Investigation of the Properties of Nuclear Matter and Particle Structure at the Collider of Relativistic Nuclei and Polarized Protons

Project STAR (JINR Participation)

A.A. Aparin, G.S. Averichev, N.A. Balashov, V.V. Belaga, T.G. Dedovich, I.Zh. Bunzarov, N.Y.Chankova-Bunzarova, V.B. Dunin, J. Fedorishin, A.O. Kechechian, K.V. Klygina, V.V. Korenkov, E.A. Kuznetsov, R. Lednicky, V.V. Lyuboshitz, V.V. Mitsyn, M.P. Osmachko, G.A. Ososkov, E.V. Potrebenikova, O.V. Rogachevski, N. E. Sidorov, E. Shakhaliev, M.V. Tokarev, P. Filip, N. I. Vorontsova, S.F. Vokal, I. Zborovsky

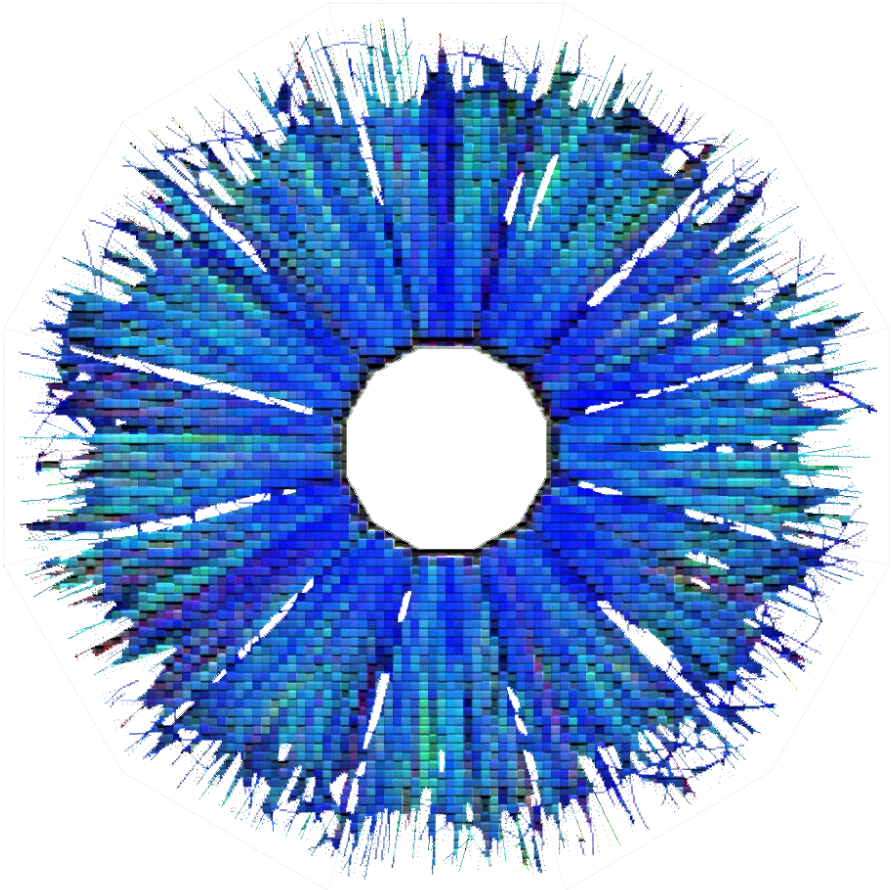

Dubna, 2018

Форма № 24

Investigation of the Properties of Nuclear Matter and Particle Structure at the Collider of Relativistic Nuclei and Polarized Protons

Project STAR (JINR participation)

JINR TOPIC : *02-0-1066-2009/2021*

A.A. Aparin, G.S. Averichev, N.A. Balashov, V.V. Belaga, T.G. Dedovich, I.Zh. Bunzarov, N.Y.Chankova-Bunzarova, V.B. Dunin, J. Fedorishin, A.O. Kechechian, K.V. Klygina, V.V. Korenkov, E.A. Kuznetsov, R. Lednicky, V.V. Lyuboshitz, V.V. Mitsyn, M.P. Osmachko, G.A. Ososkov, E.V. Potrebenikova, O.V. Rogachevski, N. E. Sidorov, E. Shakhaliev, M.V. Tokarev, P. Filip, N. I. Vorontsova, S.F. Vokal, I. Zborovsky

Project leader _____ R. Lednicky
Project leader _____ Yu.A. Panebratsev

ДАТА ПРЕДСТАВЛЕНИЯ ПРОЕКТА В НОО _____
ДАТА НТС ЛАБОРАТОРИИ _____
НОМЕР ДОКУМЕНТА _____

Форма № 25

Investigation of the Properties of Nuclear Matter and Particle Structure at the Collider of Relativistic Nuclei and Polarized Protons

Project STAR (JINR participation)

JINR topic: *02-0-1066-2009/2021*

APPROVED by JINR DIRECTOR	_____ signature	_____ data
AGREED	_____ signature	_____ data
VICE-DIRECTOR JINR	_____ signature	_____ data
CHIEF SCIENTIFIC SECRETARY JINR	_____ signature	_____ data
DIRECTOR JINR of FINANCE AND ECONOMICS OFFICE	_____ signature	_____ data
CHIEF ENGINEER JINR	_____ signature	_____ data
DIRECTOR of LHEP	_____ signature	_____ data
CHIEF ENGINEER LHEP	_____ signature	_____ data
PROJECT SCIENTIFIC LEADER	_____ signature	_____ data
PROJECT SCIENTIFIC LEADER	_____ signature	_____ data

E N D O R S E D
PAC for PARTICLE PHYSICS

_____ signature _____ data

Форма № 26

Schedule of the project

Activity		Years				
		2018	**2019**	**2020**	**2021**	**2022**
1.	Study of nuclear collisions.					
1.1.	Ru, Zr measurements at 200 GeV.					
1.2.	Global polarization measurements at 27 GeV.					
1.3.	Fixed targetmeasurements at 3 GeV.					
2.	Data analysis.					
2.1.	Ru, Zr measurements at 200 GeV.					
2.2.	Global polarization measurements at 27 GeV.					
2.3.	Fixed targetmeasurements at 3 GeV.					
3.	BES Phase-II program to search for the QCD critical point.					
3.1.	Data taking runs.					
3.2.	Data analysis of accumulated statistics.					
3.3.	Data taking with fixed target.					
3.4.	Data analysis with fixed target.					
4.	Final data taking run for BES-II.					

Форма № 29

Cost Estimate of Project

№	*Name*	*Full Cost (kUSD)*	*Expenses per Year (kUSD)*		
			2019	*2020*	*2021*
1.	*Materials and Equipment*	***45,0***	*15,0*	*15,0*	*15,0*
2.	*Research&Development*	***45,0***	*15,0*	*15,0*	*15,0*
3.	*Travel Expenses*	***210,0***	*70,0*	*70,0*	*70,0*
	Total per year	***300,0***	***100,0***	***100,0***	***100,0***

Executive Summary

This project of the JINR–STAR group is focused on two compelling programs that are key to the completion of the RHIC mission. First, study of isobaric collisions will provide enhanced clarity of the role of the magnetic field in the charge separation measurements. Second, STAR collaboration proposes Beam Energy Scan II (BES-II) program which will dramatically enhance our understanding of the QCD phase diagram.

STAR's **highest scientiftc priority for 2018–2019** is the successful realization of the isobaric collision program. In 2018 two 3.5 week runs have started with collisions of Ruthenium-96 (Ru+Ru) and Zirconium-96 (Zr+Zr) at $\sqrt{s_{NN}}$ = 200 GeV. The following data analysis and comparison of results from these events will help clarify the interpretation of measurements related to the chiral magnetic effect. Since Ru nuclei have an atomic charge of 44 compared to 40 for Zr, Ru+Ru collisions will generate a magnetic field approximately 10% larger than Zr+Zr collisions while all else remains essentially constant. Comparison of charge separation results will aid in determining the fraction of those measurements which are related to the chiral magnetic effect by isolating the magnetic field dependence. Our understanding of the chiral magnetic effect will thereby be greatly advanced and have a fundamental impact beyond the field of high-temperature QCD.

STAR's *second highest priority is measurement and following data analysis of* Au+Au collisions at $\sqrt{s_{NN}}$ = 27 GeV which will allow to make statistically significant Λ and $\overline{\Lambda}$ global polarization measurements. These measurements will take advantage of the newly installed Event Plane Detector's improved first-order reaction plane resolution.

STAR's *third highest priorities* are Au+Au collisions at $\sqrt{s_{NN}}$ = 3.2 GeV in "fixed target" mode. $\sqrt{s_{NN}}$ =3.2 GeV running will allow for a statistically significant measurement of Kurtosis at a collision energy between the HADES measurement at 2.4 GeV and STAR's lowest energy point at 7.7 GeV. This energy is accessible and being pursued by other international experiments, BM@N and CBM.

STAR's **highest scientiftc priority for 2019–2021** is the commencement of the RHIC Beam Energy Scan II.

Three upgrades are planned for completion prior to the BES-II. Both the inner Time Projection Chamber (iTPC) and the endcap Time of Flight (eTOF) are on schedule for full installation in Run 19; increasing the rapidity and low transverse momentum acceptance of STAR, and extending our particle identification capabilities. The Event Plane Detector (EPD) will be fully installed for in 2018. The EPD provides enhanced event plane resolution and forward centrality measurements.

Table 1 summarizes our request for Run 18 assuming 15 cryo-weeks. Table 2 and Table 3 summarize the request for the start of the BES-II program considering two scenarios:

- Scenario 1: 24 cryo-weeks in 2019,
- Scenario 2: 20 cryo-weeks from a combined run during 2019–2020.

For both scenarios we assume another RHIC run occurs to allow the completion of the BES-II. Table 4 outlines the dataset STAR currently plans to collect at that time. Collection of these data will allow us to achieve our high impact physics goals on a timescale consistent with the current intense international interest while utilizing RHIC beams effectively and taking full advantage of intended improvements in machine and detector capabilities.

Table 1: Beam Use Request for Run 18 assuming 15 cryo-weeks of running (including 2 weeks for the Coherent electron Cooling test).

Beam Energy (GeV/nucleon)	$\sqrt{s_{NN}}$ (GeV)	Run Time	Species	Number Events	Priority	Sequence
100	200	3.5 weeks	Ru+Ru	1.2B MB	1	1
100	200	3.5 weeks	Zr+Zr	1.2B MB	1	2
13.5	27	3 weeks	Au+Au	1B MB	2	3
3.85	3.0 (FXT)	2 days	Au+Au	100M MB	3	4

Table 2: Beam Use Request for Run 19 assuming 24 cryo-weeks of running. We assume that the commissioning of the low-energy electron cooling will be complete by the end of the first half of the run period and perform at its design for 11.5 GeV collisions in the later period of the Run 19. A possible option is to take half of the dataset at 9.1 GeV or extend the 11.5 GeV dataset running time if cooling is not yet at design performance. We are also assessing possible isobar data-taking at a lower energy depending on the outcoming of Au+Au at 27 GeV and isobar low energy test in Run 18. We could also run Au+Au collisions at $\sqrt{s_{NN}}$ = 16.7 GeV, to search for possible critical behavior assuminga narrow critical region between 14.5 and 19.6 GeV.

Beam Energy (GeV/nucleon)	$\sqrt{s_{NN}}$ (GeV)	Run Time	Species	Number Events	Priority	Sequence
9.8	19.6	4.5 weeks	Au+Au	400M MB	1	1
7.3	14.5	5.5 weeks	Au+Au	300M MB	1	3
5.75	11.5	5 weeks 4	Au+Au	230M MB	1	5
4.6	9.1[1]	weeks	Au+Au	160M MB	1	7
9.8	4.5 (FXT)	2 days	Au+Au	100M MB	2	2
7.3	3.9 (FXT)	2 days	Au+Au	100M MB	2	4
5.75	3.5 (FXT)	2 days	Au+Au	100M MB	2	6
31.2	7.7 (FXT)	2 days	Au+Au	100M MB	2	8
19.5	6.2 (FXT)	2 days	Au+Au	100M MB	2	9
13.5	5.2 (FXT)	2 days	Au+Au	100M MB	2	10

[1] The complete request is for 160M MB events and will take 9.5 weeks to collect assuming design cooling performance. The remainder of the data will be collected in the second BES-II run.

Table 3: Beam Use Request for a combined Run 19+20 assuming 20 cryo-weeks of running.

Beam Energy (GeV/nucleon)	$\sqrt{s_{NN}}$ (GeV)	Run Time	Species	Number Events	Priority	Sequence
9.8	19.6	4.5 weeks	Au+Au	400M MB	1	1
7.3	14.5	5.5 weeks	Au+Au	300M MB	1	3
5.75	11.5	5 weeks	Au+Au	230M MB	1	5
9.8	4.5 (FXT)	2 days	Au+Au	100M MB	2	2
7.3	3.9 (FXT)	2 days	Au+Au	100M MB	2	4
5.75	3.5 (FXT)	2 days	Au+Au	100M MB	2	6
31.2	7.7 (FXT)	2 days	Au+Au	100M MB	2	7
19.5	6.2 (FXT)	2 days	Au+Au	100M MB	2	8
13.5	5.2 (FXT)	2 days	Au+Au	100M MB	2	9

Table 4: Plans for Run 20 or Run 21 assuming 24 cryo-weeks of running.

Beam Energy (GeV/nucleon)	$\sqrt{s_{NN}}$ (GeV)	Run Time	Species	Number Events	Priority	Sequence
4.6	9.1[1]	9.5 weeks	Au+Au	160M MB	1	1
3.85	7.7	12 weeks	Au+Au	100M MB	1	2
3.85	3.0 (FXT)	2 days	Au+Au	100M MB	2	3

This project document is outlined as follows: in Section 1 we report highlights from completed analysis of STAR data with a focus on data from Runs 14–16. In Section 2 we discuss the research program for isobaric nuclei and global polarization. Section 3 details the STAR Collaboration's physics program which motivates beam use request for 2019–2020. Next in Section 4 we discuss the status of computing at STAR with an emphasis on the STAR–JINR Grid Computing. In the Appendix 1 is devoted to the specific JINR contribution to the STAR data analysis in 2015–2018. Appendix 2 describes STAR detectors chracteristics after its upgrade for BES-II research program: Event Plane Detector (EPD), Time Projection Chamber (iTPC) and endcap Time of Flight (eTOF).

Contents

1 STAR Heavy-Ion Highlights

Since 2015, STAR has published more than 30 papers in refereed journals: Nature, Physics Review Letters, Physics Letters B and others. In addition, STAR collaborators have made numerous contributions at conferences and workshops presenting preliminary results, including more than 60 talks at SPIN16, DIS17, SQM16, HP2016, QM2017, ISMD2017, NEC'2017, DSPIN-2017, Baldin ISHEPP 23.

Below highlights for Heavy Ion Program from these publications and preliminary analyses are presented.

1.1 Exploration of the Phase Diagram in BES-I

An important goal of high-energy heavy-ion collision experiments is to explore the Quantum Chromodynamics (QCD) phase diagram, usually spanned by temperature (T) versus baryon chemical potential (μ_B). If a thermalized system is created in heavy-ion collisions, both T and μ_B can be varied by changing the collision energy [1, 2, 3, 4], as at RHIC for the Beam Energy Scan phase I (BES-I) program. In order to estimate the T and μ_B regions of the phase diagram for a given collision energy, one can study the hadron spectra. These spectra reflect the properties of the bulk matter at the kinetic freeze-out that takes place after all the elastic scatterings have ceased. Information on the earlier stages can be deduced from the integrated yields of different hadron species, which change only via inelastic scatterings. The point when the inelastic scatterings cease is called the chemical freeze-out.

Recently STAR has submitted a paper [5] on the measurement of bulk properties of the medium produced in relativistic Au+Au collisions from BES-I. This paper presents thermal fits to the data for collision energies from $\sqrt{s_{NN}}$ = 200 to 7.7 GeV and shows that the μ_B extracted range from ~ 20 to ~ 400 MeV as expected.

In addition, a Blast-Wave model fit to pion, kaon, proton, and antiproton p_T spectra allowed the extraction of the common temperature, T_{kin}, and average transverse radial flow velocity, β, at kinetic freeze-out.

Figure 1 (left plot) shows the energy dependence of the kinetic and chemical freeze-out temperatures for central heavy-ion collisions. The values of the kinetic and chemical freeze-out temperatures are similar around $\sqrt{s_{NN}}$ = 4–5 GeV. Above $\sqrt{s_{NN}}$ = 11.5 GeV, the chemical freeze-out temperature increases with increasing the collision energy, whereas the kinetic freeze-out temperature becomes constant. Figure 1 (right plot) shows the average transverse radial flow velocity plotted as a function of $\sqrt{s_{NN}}$. The $\langle\beta\rangle$ shows a rapid increase at very low energies, and then a steady increase up to LHC energies.

T_{kin} increases from central to peripheral collisions suggesting a longer lived fireball in central collisions, while $\langle\beta\rangle$ decreases from central to peripheral collisions suggesting stronger expansion in central collisions. The separation between T_{ch} and T_{kin} increases with increasing energy. This suggests the effect of increasing hadronic interactions between chemical and

kinetic freeze-out at higher energies.

1.2 Search for the First-Order Phase Transition

A first-order phase transition is characterized bya discontinuity in one of the equation-of-state (EOS) variables. Lattice QCD predicts that there should be a discontinuity in the density below T_C [6]. A first-order phase transition is also characterized by an unstable coexistence region. This region will exhibit a change in compressibility, i.e. a softening of the EOS. In the scenario of nuclear collisions at the optimum beam energy for a first-order phase transition, various models have predicted characteristic azimuthal anisotropy signals [7, 8]. These patterns can be studied via measurement of the Fourier expansion of the final-state momentum-space azimuthal distribution relative to the reaction plane [9]. For example, the directed and elliptic flow can be quantified by the first (v_1) and second (v_2) Fourier coefficients of the expansion.

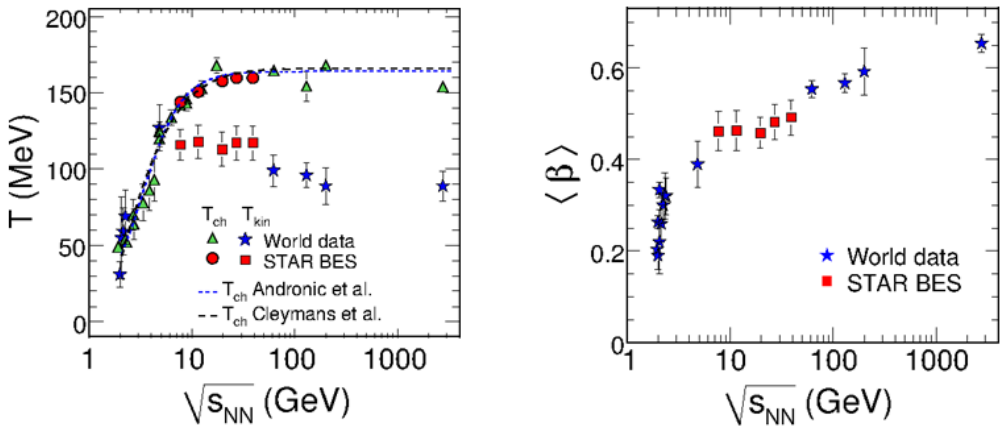

Figure 1: (left plot) Energy dependence of the kinetic and chemical freeze-out temperatures for central heavy-ion collisions. The curves represent various theoretical predictions. (right plot) Energy dependence of average transverse radial flow velocity for central heavy-ion collisions. Uncertainties represent systematic uncertainties.

Directed flow in BES-I: Recently, STAR published the beam energy dependence of the slope of directed flow (dv_1/dy) for protons and net protons near mid-rapidity [10]. The observation of a minimum in the slope of directed flow for protons and net-protons around $\sqrt{s_{NN}}$ = 10–20 GeV, and a double sign change in this observable for net-protons, suggest a possible softening of the QCD equation of state [11]. Recent model calculations, with and without crossover and first-order phase transitions, show large discrepancies with the STAR measurements [12, 13, 14].

The left plot of Figure 2 shows the dv_1/dy for all the measured strange hadrons, protons and antiprotons. The dv_1/dy slope of Λ is consistent with that of protons at all beam energies, while the $\bar{\Lambda}$ follows the trend of antiprotons. The dv_1/dy for K^+ is closer to zero than that for K^- for $\sqrt{s_{NN}}$ > 14.5 GeV. The neutral kaon dv_1/dy follows charged kaon trend and lays between positive and negative kaons. The dv_1/dy for ϕ meson shows similar trends as $\bar{\Lambda}$ and $\bar{p}$ for $\sqrt{s_{NN}}$ > 14.5 GeV, while at 11.5 GeV it is consistent with zero within large uncertainty.

This new set of measurements with different hadron species [15, 16], and hence different constituent quarks, will not only help to understand the QCD phase transition, but in addition will allow to disentangle the role of produced and transported quarks in heavy-ion collisions. The ϕ meson offers a unique advantage because its mass is similar to the proton mass, yet it is a vector meson. Moreover, ϕ meson is minimally affected by late-stage hadronic interactions.

The right plot of Figure 2 shows a comparison between the measurements and UrQMD [17] for ϕ, Λ and p. UrQMD seems to follow the trend of the data for higher beam energies, but deviates at lower energies.

Directed flow in asymmetric systems: Recent theoretical studies suggest that an asymmetric colliding system can provide new insights regarding the properties of a QGP, such as the electric conductivity [18] and the time evolution of the quark densities [19]. Due to the difference in the number of protons in the two nuclei, a strong electric field is created at the initial stage. The electric charges from quarks and antiquarks that are present in the early stage of the collision would experience the Coulomb force and so would be pushed along or opposite to the field direction depending on the particle charge.

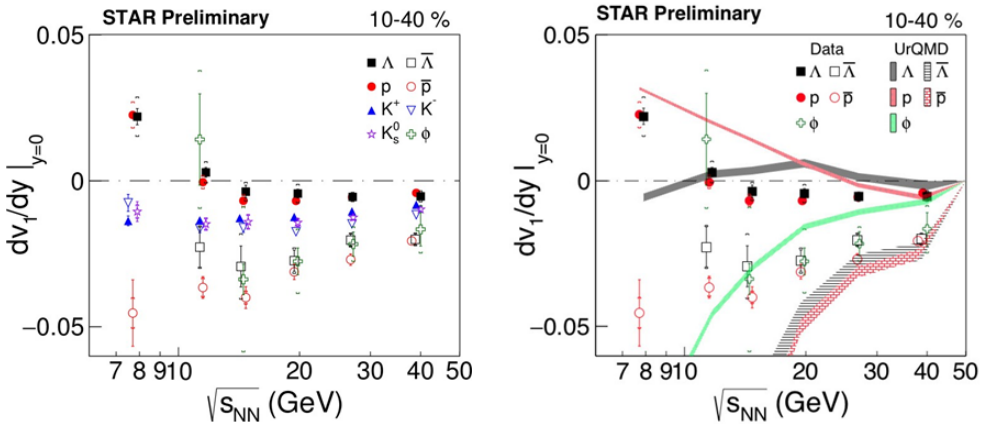

Figure 2: (left plot) Beam energy dependence of dv_1/dy for p, $\bar{p}$, $K^{\pm}$, K_s^0, ϕ, Λ and $\bar{\Lambda}$ in 10–40% Au+Au collisions. (right plot) Beam energy dependence of dv_1/dy for p, $\bar{p}$, ϕ, Λ and $\bar{\Lambda}$ in 10–40% Au+Au collisions. STAR data are compared with UrQMD model [17].

STAR recently published in PRL measurements of positive and negative particle v_1 as a function of p_T in Cu+Au and Au+Au collisions at top RHIC energy [20]. Figure 3 shows the dependencies of v_1 and Δv_1 on p_T. A finite difference in v_1 between positive and negative charged particles was observed in the transverse momentum range of $0.15 < p_T < 2$ GeV/c for Cu+Au collisions, meanwhile, the same difference is absent for Au+Au collisions (within uncertainties).

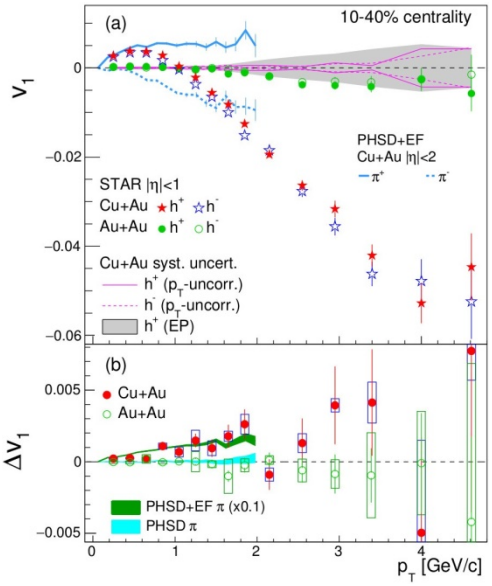

Figure 3: Directed flow of positive and negative particles and the difference between the two spectra as a function of p_T in 10%–40% centrality in Cu+Au and Au+Au collisions. The PHSD model calculations [19] for charged pions with and without the initial electric field (EF) in the same centrality region are presented for comparison. Note that the charge difference of υ_1 with the EF-on is scaled by 0.1.

These results are consistent with the presumption of a strong, initial, electric field in asymmetric collisions. The observed $\Delta\upsilon_1$ was compared to the PHSD model calculations that includes the effect of an electric field. The p_T dependence of $\Delta\upsilon_1$ is qualitatively described by the model in the region less than 2 GeV/*c*, but the magnitude of $\Delta\upsilon_1$ is smaller by a factor of 10 than the model predictions, assuming that all quarks are created at the initial time. This may indicate that most of quarks and antiquarks have not yet been created within the lifetime of the electric field ($t \leq 0.25$ fm/*c*).

1.3 Elliptic Flow of the QCD Medium

The study of collective flow in relativistic nuclear collisions could provide insights into the EOS of the matter created during heavy-ion collisions. The υ_2 coeffcient has proven to be one of the most discussed probes of the dynamics in nuclear collisions.

Multistrange particle υ_2: As recently reported in PRL, STAR measured the centrality and transverse momentum dependence of elliptic flow of multistrange hadrons and ϕ meson in Au+Au collisions at top RHIC energy [21]. It was found that unlike π and *p*, the ϕ and Ω do not participate strongly in the hadronic interactions, which suggests that the major part of collectivity is developed during the partonic phase in Au+Au collisions at $\sqrt{s_{NN}}$ = 200 GeV.

Figure 4 shows the ratios of ϕ meson υ_2 to proton υ_2. The ratios are larger than unity at p_T ~ 5 GeV/*c* for 0%–30% centrality showing an indication of the breakdown of the expected mass ordering in that momentum range. This could be due to a large effect of hadronic rescattering on the proton υ_2, indicated by the shaded red band in Figure 4 (a).

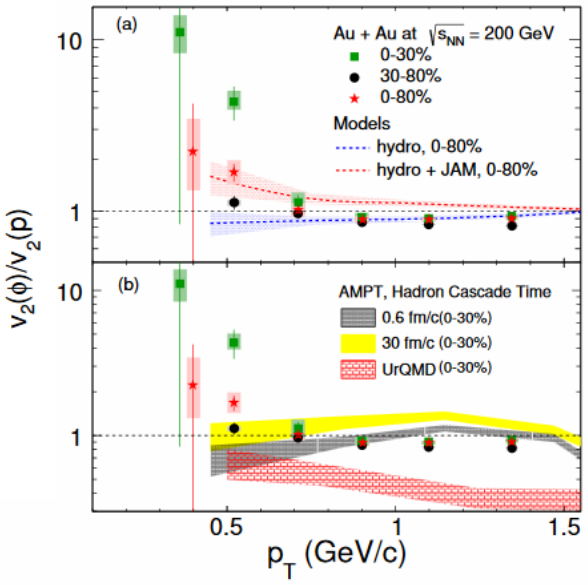

Figure 4: $\upsilon_2(\phi)/\upsilon_2(p)$ ratio as a function of p_T for 0%–30%, 30%–80%, and 0%–80% centrality in Au+Au collisions at $\sqrt{s_{NN}}$ = 200 GeV. Shaded boxes are the systematic uncertainties and vertical lines are the statistical uncertainties. The first data point of 0%–80% centrality is shifted to the right by 400 MeV/*c*. The bands in (a) and (b) represent the Hydrodynamics model [22] and transport model calculations, respectively, for $\upsilon_2(\phi)/\upsilon_2(p)$.

The effect is more pronounced in the 0%–30% than in 30%–80% centrality. In the central events, both hadronic and partonic interactions are larger than in peripheral events. Therefore, the combined effects of large partonic collectivity on the ϕ meson υ_2 and significant late-stage hadronic interactions on the proton υ_2 produce a greater breakdown of the mass ordering in the 0%–30% centrality data than in the 30%–80%. This observation indirectly supports the idea of a small hadronic interaction cross section for the ϕ meson. The ratio of ϕ υ_2 to proton υ_2 has been also studied using transport models AMPT [23] and UrQMD [17]. Figure 4 (b) shows ratios for 0%–30% centrality from the AMPT and UrQMD models. The black shaded band is from AMPT with a hadronic cascade time of 0.6 fm/*c*, while the yellow band is for a hadronic cascade time of 30 fm/*c*. It becomes clear that with increasing hadronic cascade time (and therefore more hadronic rescattering), the $\upsilon_2(\phi)/\upsilon_2(p)$ ratio increases. This is attributed to a decrease in the proton υ_2 due to an increase in hadronic rescattering, while the ϕ υ_2 remains unaffected.

Elliptic flow of light nuclei: STAR has measured the centrality dependence of the relative difference of baryon and antibaryon elliptic flow [24, 25]. It was found that the difference becomes larger with decreasing collision energy.

In a relativistic heavy-ion collision, light (anti-)nuclei can be formed by coalescence of produced (anti-)nucleons or from transported nucleons. The binding energies of light nuclei are very small (~ few MeV), making it likely that surviving light nuclei are formed at a later stage of the evolution. This phenomenon is called final-state coalescence.

STAR studied the p_T dependence of υ_2 of p, $\bar{p}$, d, $\bar{d}$, t, ^{3}He and $^3\overline{\text{He}}$ from Au+Au collisions in BES-I [26]. Figure 5 shows the light-nuclei υ_2/A as a function of p_T/A where A is the atomic mass number of the corresponding light nuclei. It is observed that the

(anti)nuclei v_2/A closely follows v_2/A of $p(\bar{p})$ for p_T/A up to 1.5 GeV/c within 5%–20% or all beam energy range presented. The scaling behavior of these nuclei suggest that $d(\bar{d})$ within p_T < 3.0 GeV/c and t, ^{3}He ($^3\overline{\text{He}}$) within p_T < 4.5 GeV/c might have formed via the coalescence of nucleons (antinucleons).

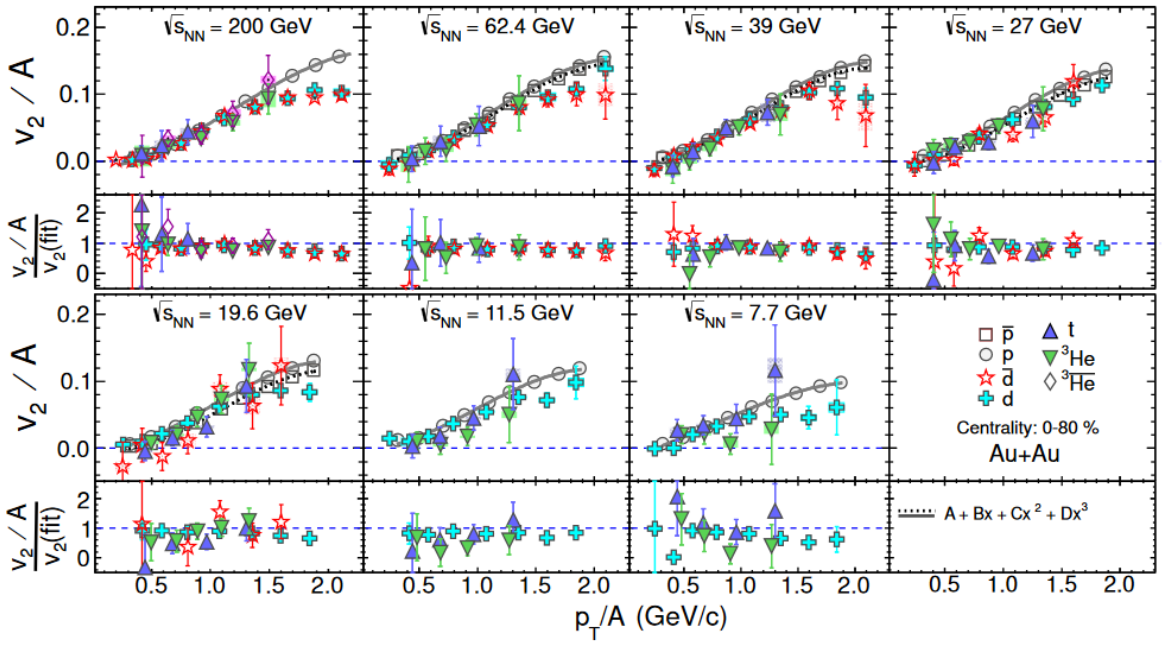

Figure 5: Atomic mass number (A) scaling of the midrapidity v_2 of p, $\bar{p}$, d, $\bar{d}$, t, ^{3}He and $^3\overline{\text{He}}$ from minimum-bias Au+Au collisions at $\sqrt{s_{NN}}$ = 200, 62.4, 39, 27, 19.6, 11.5, and 7.7 GeV. Gray solid (black dotted) lines correspond to third order polynomial fits to the p ($\bar{p}$) v_2 data. The ratios of (v_2/A/fit) for d, $\bar{d}$, t and ^{3}He are shown in the lower panels at each corresponding collision energy.

The low relative production of light nuclei and the scaling behavior of their elliptic flow seems to be favored by the coalescence formalism over the other methods, such as thermal production which can reproduce the measured particle ratios in data [27]. Although simple A scaling seems to hold for the collision energies presented, the actual mechanism might be a more dynamic process including production and coalescence of nucleons in the local rest frame of the fluid cell.

In addition, STAR presented at QM2017 the dependence of the coalescence factor of deuterons and antideuterons, B_2, as a function of m_T and collision energy. It was found that B_2 decreases with increasing m_T. The B_2 decreases with decreasing energy showing the minimum at around $\sqrt{s_{NN}}$ = 20 GeV. The $B_2(\bar{d})$ is systematically lower that those of $B_2(d)$. This suggests that the emitting source of antibaryons is larger that for baryons.

1.4 Rapidity Correlations

Initial state density fluctuations and the pressure gradient of the strongly interacting medium in the transverse plane result in azimuthal anisotropies of the emitted particles in the final state. The density fluctuations can be studied in terms of correlations of particles in the longitudinal direction, i.e. in (pseudo)rapidity [28]. Long-range rapidity correlations, and other "short range" mechanisms such as resonance decays, jet fragmentation, and quantum statistical effects, appear in specific ways in the correlation function [29]. The shape of the

longitudinal correlations can be characterized by Legendre polynomials with magnitudes given by prefactors a_{nm}.

Rapidity correlations were studied and reported for the first time at QM2017 in Au+Au collisions at eight different beam energies from 7.7 to 200 GeV (0%–5% centrality) as measured by STAR for the BES-I program [30]. It was observed that the magnitude of the coeffcients decreases with increasing beam energy, indicating decreased two-particle correlations per pair as $\sqrt{s_{NN}}$ increases. A significant increase in the magnitude of the $\langle a_{nm} \rangle$ coeffcients for pions at 19.6 and 27.0 GeV was observed. In order to understand the observed structure, the averaged correlation functions for pions versus Δy were calculated in three different ranges of the azimuthal angle $\Delta\phi$: near-side ($-30^\circ < \Delta\phi < 30^\circ$), far-side ($150^\circ < \Delta\phi < 210^\circ$) and transverse ($30^\circ < \Delta\phi < 150^\circ$ and $210^\circ < \Delta\phi < 330^\circ$) for 19.6 and 27 GeV and their neighboring energies (14.5 and 39 GeV) as shown in Figure 6.

In the near-side projection there is a peak around $\Delta y \sim 0$ which is stronger in unlike- sign pions than like-sign pions. This is an expected feature of the short-range correlation mechanisms that are dominant in this $\Delta\phi$ range. There is no significant structure in the far-side projection of both like-sign and unlike-sign pions at these energies. However, the transverse projection shows a significant and unexpected peak around $\Delta y \sim 0$ at 19.6 and 27 GeV. This structure has the same magnitude for both like-sign and unlike-sign pions.

1.5 Global Hyperon Polarization

Non-central collisions have angular momentum on the order of $1000\,\hbar$, and shear forces generated by the interpenetrating nuclei may generate a clear vortical structure [31, 32, 33]. A slight sideward deflection of the forward- and backward-traveling fragments from a given collision allows experimental determination of the direction of the overall angular momentum, $\hat{J}_{sys}$. Spin-orbit coupling can generate a spin alignment, or polarization, along the direction of the vorticity which is on average parallel to $\hat{J}_{sys}$. Hence, polarization measurements of hadrons emitted from the fluid can be used to determine the vorticity.

STAR used Λ and $\overline{\Lambda}$ to measure the global hyperon polarization in non-central Au+Au collisions [34]. The advantage of using Λ-hyperons is that due to the weak decay into p and π^-, the proton tends to be emitted along the spin direction of the parent Λ. The polarization ($\vec{P}_H$) may depend on the momentum of the emitted hyperons. However, when averaged over all phase space, symmetry demands that $\vec{P}_H$ is parallel to $\hat{J}_{sys}$. Due to the limited statistics, only the average projection ($\overline{P}_H$) of $\vec{P}_H$ on $\hat{J}_{sys}$ was extracted.

Figure 7 shows the measurements of the global polarization as a function of collision energy. At each energy, a positive polarization at the level of 1.1–3.6 times statistical uncertainty is observed for both Λ and $\overline{\Lambda}$. The data are statistically consistent with the hypothesis of energy-independent polarizations of 1.08 ± 0.15 and 1.38 ± 0.30 percent for Λ and $\overline{\Lambda}$, respectively.

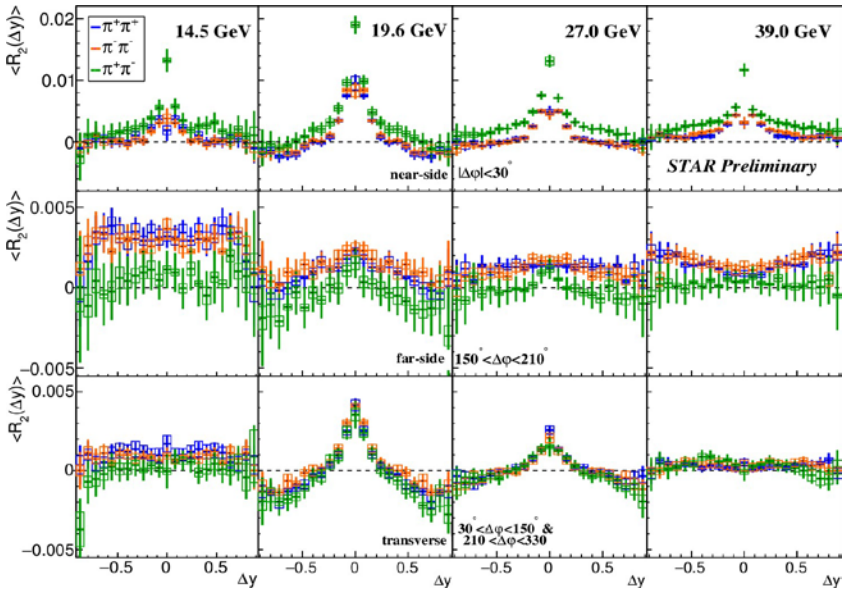

Figure 6: The averaged correlation function for pions as a function of Δ*y* for 14.5, 19.6, 27, and 39 GeV (from left to right respectively) beam energies in 0%–5%

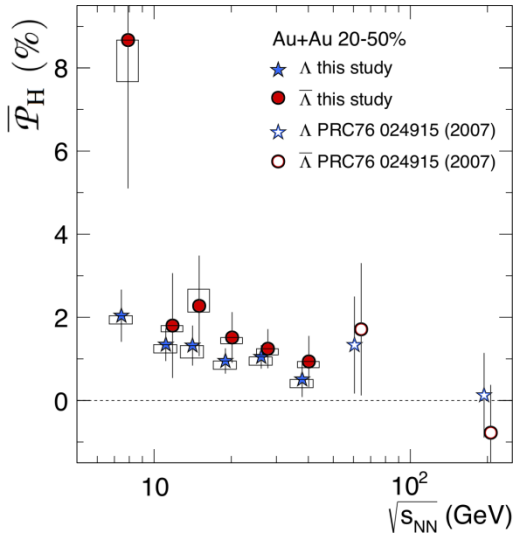

Figure 7: The average polarization $\overline{P}_H$ (where H = Λ or $\overline{\Lambda}$) from 20%–50% central Au+Au collisions as a function of collision energy. The results of the present study ($\sqrt{s_{NN}}$ < 40 GeV) are shown together with those reported earlier [35] for 62.4 and 200 GeV collisions, for which only statistical errors are plotted. Boxes indicate systematic uncertainties.

Previously published measurements at $\sqrt{s_{NN}}$ = 62.4 GeV and 200 GeV are shown by open symbols [35]. The null result reported in that paper may be considered to be consistent with the trend of our measurements, within reported statistical uncertainty.

The $\sqrt{s_{NN}}$ -averaged polarizations indicate a vorticity of $\omega \approx (9\pm1) \times 10^{21}$ s^{-1}, which is estimated using the hydrodynamic relations and takes into account the "feed-down" contributions [36]. The discovery of the global Λ polarization in non-central heavy-ion collisions opens new directions in the study of the hottest, least viscous – and now, most vortical – fluid ever produced in the laboratory. These results have been published in Nature [34].

1.6 First Fixed Target Results

The test run for the fixed target (FXT) program performed in Run 15 while primarily a technical test also resulted in 1.3 millions Au+Au events being acquired at $\sqrt{s_{NN}}$ = 4.5 GeV. Analysis of these events has been completed and were reported at the QM2017 meeting. The new results were compared to previously published data from the AGS program to demonstrate consistency. Results were presented for spectra of π, K^0_S, and Λ, directed flow of π, K^0_S, *p* and Λ, elliptic flow of π and *p*, HBT, and particle ratio fluctuations. Some results of this test run are shown in Figure 8. Further details of the proposed fixed target program and its science case are given in Section 3.4.

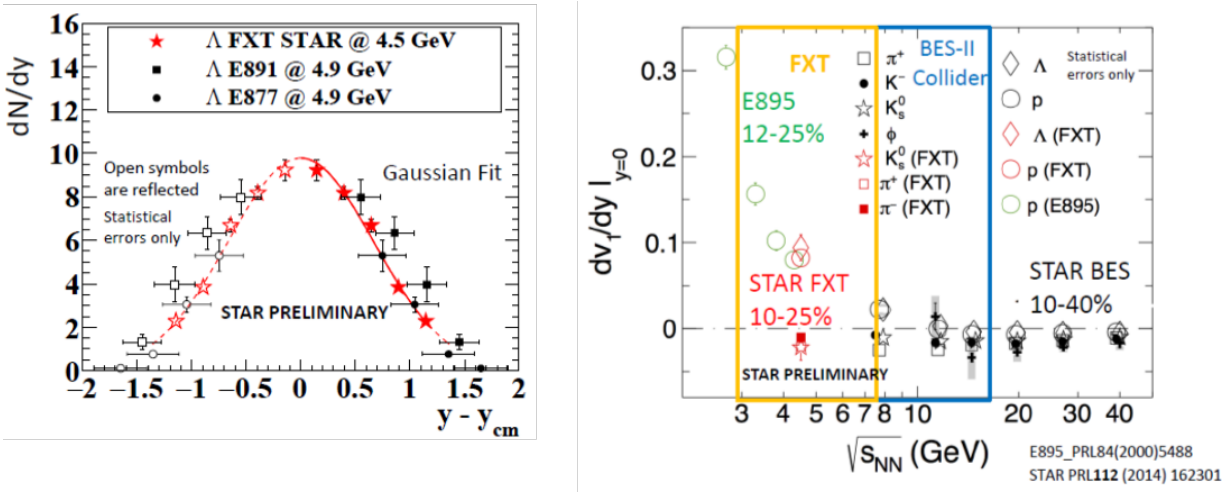

Figure 8: Sample results from the Run 15 $\sqrt{s_{NN}}$ = 4.5 GeV Au+Au test run. The Λ rapidity distribution (left) and directed flow measurements for several particle identified species in 10–25% central events (right). The FXT data are compared to other results.

1.7 Chiral Magnetic Effect

The chiral magnetic effect (CME) [37, 38] refers to the induction of an electric current ($\vec{J}_e$) by the magnetic field ($\vec{B}$) in a *chiral* system: $\vec{J}e \propto \mu_5 \vec{B}$. A chiral system bears a nonzero μ_5, which characterizes the imbalance of right-handed and left-handed fermions in the system. The discovery of the CME in high-energy heavy-ion collisions would confirm the simultaneous existence of ultra-strong magnetic fields, chiral symmetry restoration and topological charge changing transitions in these collisions. On average, $\vec{B}$ is perpendicular to the reaction plane (Ψ_{RP}) that contains the impact parameter and the beam momenta. Hence the CME will manifest a charge transport across the reaction plane.

In the presence of the CME and other modes of collective motions, we can Fourier decompose the azimuthal distribution of particles of given transverse momentum (p_T) and pseudorapidity (η):

$$\frac{dN_\alpha}{d\phi} \propto 1 + 2\upsilon_{1,\alpha}\cos(\Delta\phi) + 2\upsilon_{2,\alpha}\cos(2\Delta\phi) + \ldots + 2a_{1,\alpha}\sin(\Delta\phi) + \ldots, \quad (1)$$

where ϕ is the azimuthal angle of a particle, and $\Delta\phi = \phi - \Psi_{RP}$. Here the subscript α (+ or –) denotes the charge sign of the particle. Conventionally υ_1 is called "directed flow" and υ_2

"elliptic flow" [9]. The parameter a_1 (with $a_{1,-} = a_{1,+}$) quantifies the electric charge separation due to the CME.

Experimentally the CME has been searched for via charge-separation fluctuations perpendicular to the reaction plane, e.g., with a three-point correlator [39], $\gamma \equiv \left\langle \cos(\phi_\alpha + \phi_\beta - 2\Psi_{RP}) \right\rangle$, where the averaging is done over all particles in an event and over all events. In practice, the reaction plane is approximated with the "event plane" (Ψ_{EP}) reconstructed with measured particles, and then the measurement is corrected for the finite event plane resolution. The expansion of the γ correlator,

$$\begin{aligned} \left\langle \cos(\phi_\alpha + \phi_\beta - 2\Psi_{RP}) \right\rangle &= \left\langle \cos(\Delta\phi_\alpha)\cos(\Delta\phi_\beta) - \sin(\Delta\phi_\alpha)\sin(\Delta\phi_\beta) \right\rangle \\ &= \left(\left\langle v_{1,\alpha} v_{1,\beta} \right\rangle B_{IN} \right) - \left(\left\langle a_{1,\alpha} a_{1,\beta} \right\rangle + B_{OUT} \right), \end{aligned} \tag{2}$$

reveals the difference between the *in-plane* and *out-of-plane* projections of the correlations. The first term $\left(\left\langle \upsilon_{1,\alpha} \upsilon_{1,\beta} \right\rangle \right)$ in the expansion providesa baseline unrelated to the magnetic field. The background contribution ($B_{IN} - B_{OUT}$) is suppressed to a level close to the magnitude of υ_2 in a decaying cluster scenario [39]:

$$\frac{B_{IN} - B_{OUT}}{B_{IN} + B_{OUT}} \approx v_{2,cl} \frac{\left\langle \cos(\phi_\alpha + \phi_\beta - 2\phi_{cl}) \right\rangle}{\left\langle \cos(\phi_\alpha - \phi_\beta) \right\rangle}, \tag{3}$$

where ϕ_{cl} is the cluster emission azimuthal angle, and ϕ_α and ϕ_β are the azimuthal angles of two decay products. Note that $\upsilon_{2,cl}$ contains both flow and non-flow contributions. By "non-flow", we mean correlations not related to the reaction plane. The flowing cluster can be generalized to a larger portion of or even the whole event, through the mechanisms of transverse momentum conservation (TMC) [40, 41] and/or local charge conservation (LCC) [42].

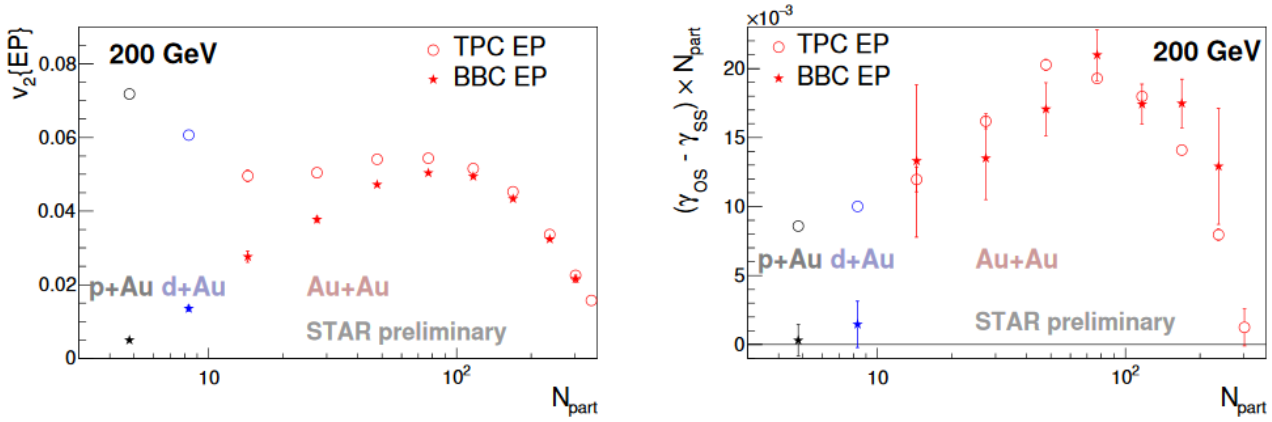

Figure 9: υ_2 (left) and $(\gamma_{OS} - \gamma_{SS}) \times N_{part}$ (right) for p+Au, d+Au and Au+Au collisions at 200 GeV, measured with event planes from both TPC and BBC.

Previous STAR measurements [43, 44, 45] have shown $\Delta\gamma \left(\equiv \gamma_{OS} - \gamma_{SS} \right) > 0$ for most centrality intervals in Au+Au, Cu+Cu and U+U collisions at 200 GeV, indicative of the charge

separation expected from the CME. The non-flow contributions in γ have been estimated to be non-dominant for mid-central and mid-peripheral Au+Au collisions at 200 GeV [79]. Recently collected p+Au (Run 15) and d+Au (Run 16) data have facilitated the systematic study of the non-flow effects in small systems. Figure 9 shows v_2 (left) and $\Delta\gamma_{*}N_{\mathrm{part}}$ (right) for p+Au, d+Au and Au+Au collisions at 200 GeV, measured with event planes from both TPC and BBC. With the TPC event plane, v_2 displays an enhancement at small values of N_{part}, demonstrating the short-range non-flow contributions, whereas with the BBC event plane, a pseudorapidity gap of at least 2.8 units is introduced between the event plane and particles of interest, and v_2 goes down monotonically with decreased N_{part}. Likewise, $\Delta\gamma_{*}N_{\mathrm{part}}$ measured for p+Au stops at a sizable positive value with the TPC event plane, and diminishes with the BBC event plane. The disappearance of the charge separation observable in p+Au is in line with the idea that the magnetic field direction and the second-order participant plane (Ψ_2) are so decoupled that no CME signals should be observed with Ψ_2 in p+Au.

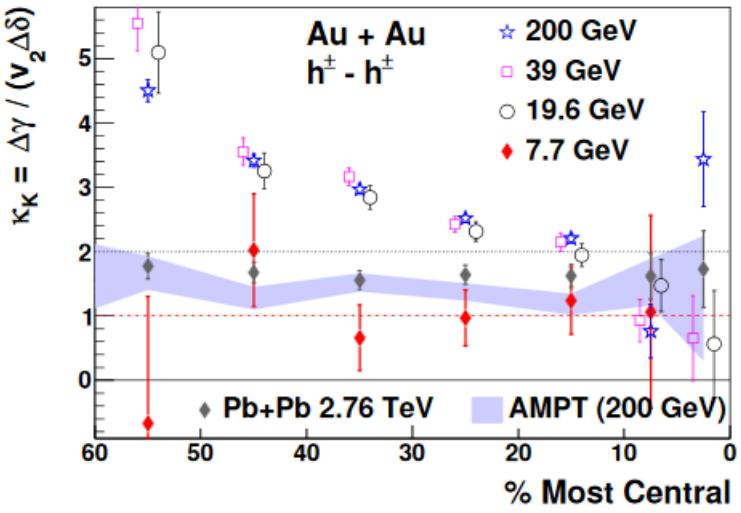

Figure 10: κ_{K} vs centrality for Au+Au collisions at 200, 39, 19.6 and 7.7 GeV [47], and for Pb+Pb collisions at 2.76 TeV [48]. The AMPT calculations are also plotted for Au+Au at 200 GeV in comparison.

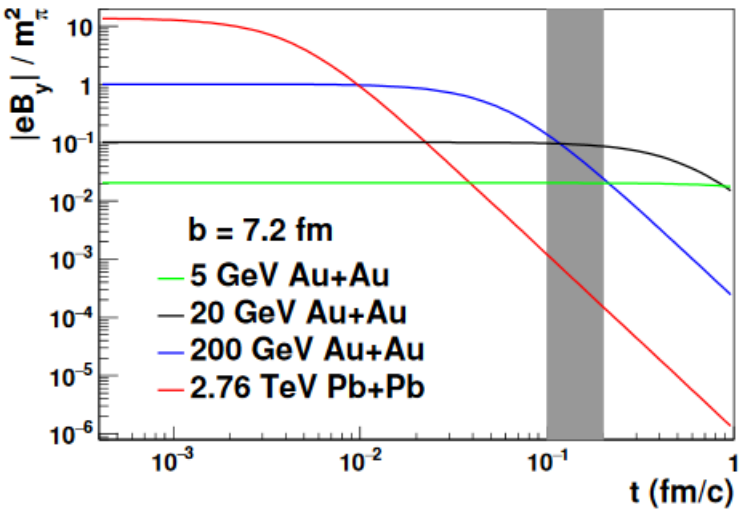

Figure 11: Magnetic field in a vacuum as a function of the evolution time for Au+Au at 5, 20 and 200 GeV and Pb+Pb at 2.76 TeV [49]. The gray band indicates the presumable initial quark production.

In mid-central and mid-peripheral Au+Au collisions at 200 GeV, the consistency between $\Delta\gamma$ measured with the TPC and the BBC event planes suggests that the charge-separation signal is

a genuine correlation with respect to the reaction plane, which corroborates the conclusion in Ref [46]. However, the non-flow-suppressed charge-separation observable could still contain flow-related backgrounds. To study the flow-related backgrounds, we define a "normalized" observable, $\kappa_K \equiv \Delta\gamma/(\upsilon_2\Delta\delta)$, to roughly scale out the influence of flow and the two-particle correlation, $\delta \equiv \langle\cos(\phi_\alpha - \phi_\beta)\rangle$. k_K can be compared between data and background scenarios estimated from theoretical calculations or model simulations. Figure 10 shows κ_K vs centrality for Au+Au collisions at 200, 39, 19.6 and 7.7 GeV [47], and for Pb+Pb collisions at 2.76 TeV [48]. The background estimation from AMPT stays between 1 and 2, and significantly below the measured k_K in 20–60% Au+Au at 200 GeV. For the time being, we assume that the background level has a very weak beam-energy dependence. The data measured at 39 GeV and 19.6 GeV look similar to the 200 GeV results, whereas κ_K for Au+Au at 7.7 GeV or Pb+Pb at 2.76 TeV seems to be a constant between 1 and 2, consistent with the background level. The CME signal disappears at 7.7 GeV presumably because of the dominance of the hadronic interaction over the partonic one, while it vanishes at 2.76 TeV probably owing to the quickly diminishing magnetic field. Figure 11 demonstrates the magnetic field in a vacuum vs time for Au+Au at 5, 20 and 200 GeV and Pb+Pb at 2.76 TeV with an impact parameter of 7.2 fm [49]. Initially the magnetic field at 2.76 TeV is about 13 times stronger than that at 200 GeV, but it decreases much faster. At t = 0.01 fm/c, they are almost identical, and by the time when quarks start to be produced (illustrated by the gray band), the magnetic field at 2.76 TeV is already weaker than that at 200 GeV by a few orders of magnitude. Recent ALICE results for Pb+Pb at 2.76 TeV with the event-shape engineering and the CMS comparison between p+Pb and Pb+Pb at 5 TeV [50] also confirm the smallness of the true CME signal at the LHC energies.

STAR has spared no effort to disentangle the possible CME signal and the flow-related background. We have studied central collisions where the charge-separation observable is dominated by the background; the CME should be greatly suppressed under the condition of the minimal magnetic field. Ref [51] presents (see. Figure 1 in this reference) $\Delta\gamma$ vs υ_2 for central Au+Au (0–20%) and U+U (0–10%) collisions. For both Au+Au and U+U, $\Delta\gamma$ tends to vanish at non-zero values of υ_2. The dependence of $\Delta\gamma$ on υ_2 in the background scenario ($\propto \upsilon_2 / N$) is non-linear since υ_2 decreases and N increases towards central events. It is a challenge to a pure background model to reproduce the positive intercept on the υ_2-axis. On the other hand, a simultaneous description of the vanishing $\Delta\gamma$ at non-zero υ_2 and its rapid linear growth can be naturally achieved by the variation of the projected magnetic field onto Ψ_2 and the ellipticity which drives υ_2 [52].

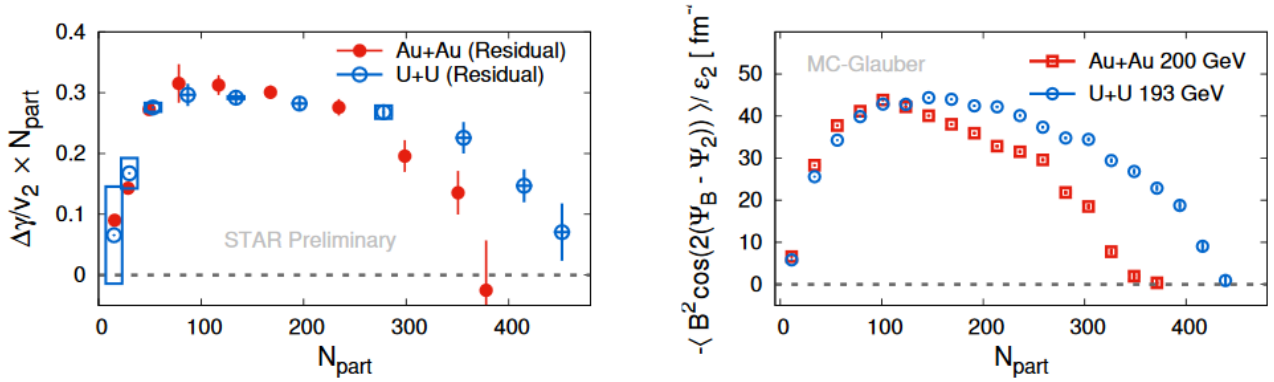

Figure 12: $\Delta\gamma/\upsilon_2 \times N_{\text{part}}$ vs N_{part} (left) and the magnetic field projection divided by ellipticity (right) for 200 GeV Au+Au and 193 GeV U+U collisions. Positive short-range correlations have been removed from the y measurements in the left panel.

Another test of the signal/background scenario has been carried out with the comparison of $\Delta\gamma/\upsilon_2 \times N_{\text{part}}$ between 200 GeV Au+Au and 193 GeV U+U, as shown in Figure 12 (left). Note that the γ measurements shown here have excluded the positive short-range correlations between particles α and β, which are determined with a multi-component fit to the differential measurement of γ as a function of the pseudorapidity gap between particles α and β. PHENIX has shown that at the same N_{part}, the multiplicity is almost identical for 200 GeV Au+Au and 193 GeV U+U [53], thus $\Delta\gamma/\upsilon_2 \times N_{\text{part}}$ should be constant and almost the same for these two systems, according to the background scenario. Data show two rise-and-fall trends for Au+Au and U+U, respectively. The two trends merge at lower N_{part}, and separate at higher N_{part}. These very features can be naturally explained by the magnetic field projection divided by ellipticity, as depicted in the right panel of Figure 12. A uranium nucleus has 13 more protons than a gold nucleus, which in turn causes the difference in the magnetic fields in U+U and Au+Au collisions. The difference in the magnetic field is compensated by the difference in ellipticity at lower N_{part}, but becomes overwhelming towards higher N_{part}.

1.8 Chiral Magnetic Wave

Another complementary transport phenomenon to the CME has been theorized and named the chiral separation effect (CSE) [54, 55], in which chiral charges are separated along the axis of the magnetic field in the presence of finite density of vector charge: $\vec{J}_5 \propto \mu_v \vec{B}$. In a chirally symmetric phase, the CME and CSE form a collective excitation, the chiral magnetic wave (CMW), a long wavelength hydrodynamic mode of chiral charge densities [56, 57]. The CMW, a signature of the chiral symmetry restoration, manifests itself in a finite electric quadrupole moment of the collision system, where the “poles" (“equator") of the produced fireball acquire additional positive (negative) charge [56]. This electric quadrupole, if boosted by radial flow, will lead to charge-dependent elliptic flow. Let’s take pions as an example: on top of the baseline $\upsilon_2^{\text{base}}(\pi^{\pm})$, the CMW will lead to [56]

$$\upsilon_2(\pi^{\pm}) = \upsilon_2^{\text{base}}(\pi^{\pm}) \mp \frac{r}{2} A_{\text{ch}}, \tag{4}$$

where $A_{\text{ch}} \equiv (N_+ - N_-)/(N_+ + N_-)$ is the charge asymmetry of the collision event, $r \equiv 2q_e/\bar{\rho}_e$, and q_e and $\bar{\rho}_e$ are the quadrupole moment and the net charge density, respectively.

Previous STAR measurements of the slope in $\Delta\upsilon_2$ (A_{ch}), r, have shown a rise-and-fall trend as

a function of centrality for Au+Au collisions at 200 GeV, as shown in Figure 13 [58]. This feature resembles the CMW expectation, whereas the UrQMD calculations yield null slopes for 20–60% collisions, where data have significant signals. Recent STAR results for p+Au and d+Au are also plotted in this figure, which are highly consistent with zero, and corroborate the falling trend previously observed at smaller systems.

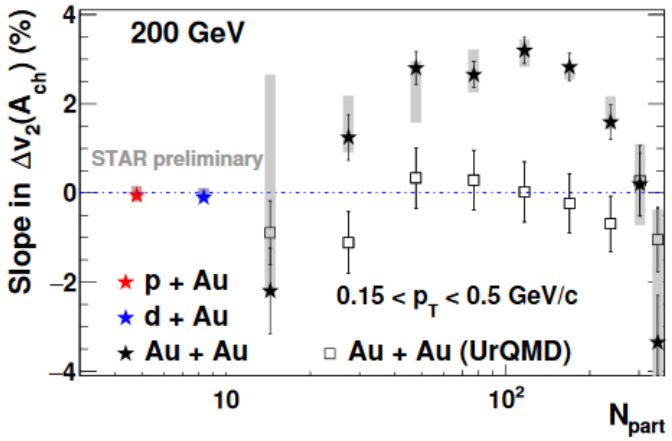

Figure 13: Slope parameter, *r* vs N_{part} for pions in p+Au, d+Au and Au+Au collisions at 200 GeV [58].

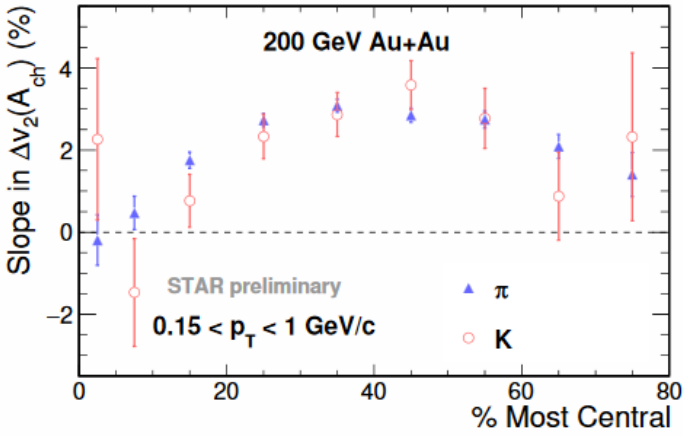

Figure 14: Slope parameter, *r* vs centrality for pions and kaons in Au+Au collisions at 200 GeV.

It was argued [59] that local charge conservation at freeze-out, when convoluted with the characteristic shape of $\upsilon_2(\eta)$ and $\upsilon_2(p_T)$, may provide a qualitative explanation for the finite υ_2 slope observed from STAR data. A realistic estimate of the contribution of this mechanism turns out to be smaller than the measurement by an order of magnitude [58]. Ref. [59] also proposes a test with the υ_3 measurement, and the corresponding slope parameters for υ_3 were reported by STAR to be consistent with zero [60], which further suggests the smallness of this effect. A hydrodynamic study [61] claimed that simple viscous transport of charges, combined with certain specific initial conditions, will lead to a sizable υ_2 splitting of charged pions. To have their results of pion splitting resemble data, the authors had to invoke a crucial relation between isospin chemical potential and the electric charge asymmetry, which needs to be verified. Furthermore, this model predicts the splitting for kaons to have the opposite sign and larger magnitude than that for pions. This prediction is contradicted by STAR data, as shown in Figure 14, where the kaon slopes have the same sign and almost identical magnitude as the pion slopes in the centrality region where the signals are significantly positive.

2 Research Program: Isobaric Nuclei and Global Polarization

In 2018 two 3.5 week runs have started with collisions of Ruthenium-96 (Ru+Ru) and Zirconium-96 (Zr+Zr) at $\sqrt{s_{NN}}$ = 200 GeV. These data will clarify the role of the magnetic field in measurements designed to probe CME and CMW effects. In addition we plan to carry out 3 week measurements of Au+Au collisions at $\sqrt{s_{NN}}$ = 27 GeV which will allow to make statistically significant Λ and $\overline{\Lambda}$ global polarization measurements. We also plan to make measurements of Au+Au collisions at $\sqrt{s_{NN}}$ = 3.2 GeV in "fixed target" mode. $\sqrt{s_{NN}}$ = 3.2 GeV running will enable fluctuation measurements at the collision energy between the HADES measurement at 2.4 GeV and STAR's lowest energy point at 7.7 GeV. More details of the physics cases that drive these requests are given below.

One of the main goals of the project in 2019 is analysis of this data and obtaining new physical results.

2.1 Collisions of Isobaric Nuclei

STAR has been searching for evidence of chiral magnetic/vortical effects for more than a decade, and so far the experimental observables support the pictures of the chiral magnetic effect and the chiral magnetic wave. To draw a firm conclusion, an effective way is needed to disentangle the signal and the background contributions, the latter of which are intertwined with collective flow. Collisions of isobaric nuclei, i.e. $^{96}_{44}\mathrm{Ru}+^{96}_{44}\mathrm{Ru}$ and $^{96}_{40}\mathrm{Zr}+^{96}_{40}\mathrm{Zr}$, present a unique opportunity to vary the initial magnetic field by a significant amount while keeping everything else almost the same. Therefore, isobaric collisions will play a decisive role in verifying/falsifying the CME. Moreover, STAR has observed a significant excess of dilepton production at very low p_T at mid-rapidity in peripheral A+A collisions, which resembles the coherent photon-nucleus interactions in ultra-peripheral events. Collisions of isobaric nuclei will shed light on the origin of this excess.

2.1.1 Chiral Magnetic Effect

In the search for the CME with the γ correlator, the non-flow backgrounds can be suppressed technically, e.g. with event planes at forward rapidities, but the approaches to remove or estimate the flow backgrounds are usually model-dependent and involve large uncertainties. To quantify the CME signal and the flow-related background in the γ correlations, we propose to collide isobaric nuclei of $^{96}_{44}\mathrm{Ru}$ and $^{96}_{40}\mathrm{Zr}$ [62], where the magnetic field can be significantly varied while the backgrounds are almost fixed. Ru+Ru and Zr+Zr collisions at the same beam energy are almost identical in terms of particle production, which is illustrated with the Monte Carlo Glauber simulation in Figure 15 [63]. The ratio of the multiplicity distributions from the two collision systems is consistent with unity almost everywhere, except in 0–5% most central collisions, where the slightly larger radius of Ru (R_0 = 5.085 fm) plays a role against that of Zr (R_0 = 5.02 fm). For the CME analysis, we focus on the centrality

range of 20 60%, so that the background difference due to the multiplicity is negligible.

The spatial distribution of nucleons in either $^{96}_{44}$Ru or $^{96}_{40}$Zr in the rest frame can be written in the Woods-Saxon form (in spherical coordinates),

$$\rho(r,\theta) = \frac{\rho_0}{1+\exp\left\{\left[r - R_0\left(1+\beta_2 Y_2^0(\theta)\right)\right]/a\right\}}, \tag{5}$$

where ρ_0 = 0.16 fm^{-3} is the normal nuclear density, R_0 and a represent the "radius" of the nucleus and the surface diffuseness parameter, respectively, and β_2 is the deformity of the nucleus. The parameter a is almost identical for Ru and Zr: $a \approx 0.46$ fm. Our current knowledge of β_2 of Ru and Zr is incomplete. According to e-A scattering experiments [64, 65] (which will be referred to as case 1), Ru is more deformed ($\beta_2^{\mathrm{Ru}} = 0.158$) than Zr ($\beta_2^{\mathrm{Zr}} = 0.08$); whereas comprehensive model deductions [66] (case 2) tells the opposite $\beta_2^{\mathrm{Ru}} = 0.053$ is smaller than $\beta_2^{\mathrm{Zr}} = 0.217$. Other B(E2) experiments indicate that $\beta_2^{\mathrm{Ru}} \approx 0.1$ and $\beta_2^{\mathrm{Zr}} \approx 0.045$ [67, 68], and the difference in β_2 between Ru and Zr is very close to case 1. In the following discussion, we still use case 1 and case 2 as two extreme cases, and the most likely result should stay between the limits set by those two cases. We have checked that this uncertainty has little influence on the multiplicity distribution.

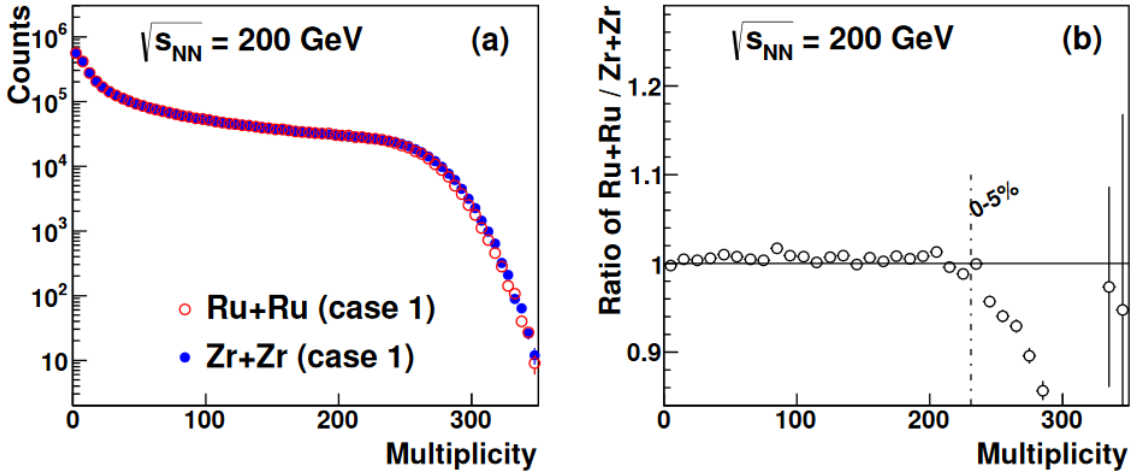

Figure 15: The Monte Carlo Glauber simulation of the multiplicity distributions for $^{96}_{44}$Ru+$^{96}_{44}$Ru and $^{96}_{40}$Zr+$^{96}_{40}$Zr at $\sqrt{s_{NN}}$ = 200 GeV (a) and their ratio (b). [63]

The charge difference between Ru and Zr nuclei provides a handle on the initial magnetic field (mostly produced by the spectator protons). Figure 16 (a) presents a theoretical calculation of the initial magnetic field squared with correction from azimuthal fluctuations of the magnetic field orientation, $B_{sq} \equiv \left\langle \left(eB/m_\pi^2\right)^2 \cos\left[2\left(\Psi_{\mathrm{B}} - \Psi_{\mathrm{RP}}\right)\right]\right\rangle$, for the two collision systems at 200 GeV, using the HIJING model [63]. B_{sq} quantifies the magnetic field's capability of driving the CME signal in the correlator γ. For the same centrality interval, the Ru+Ru collision produces a significantly stronger magnetic field than Zr+Zr.

Panel (b) of Figure 16 shows that the relative difference in B_{sq} between Ru+Ru and Zr+Zr collisions is approaching 15% (case 1) or 18% (case 2) for peripheral events, and reduces to about 13% (case 1 and case 2) for central events. In our notation, the relative difference in a

quantity F between Ru+Ru and Zr+Zr collisions is $R_F \equiv 2(F^{\text{Ru+Ru}} - F^{\text{Zr+Zr}})/(F^{\text{Ru+Ru}} + F^{\text{Zr+Zr}})$, and F can be B_{sq}, ε_2 or S. The effect of the deformity of the nucleus on the generation of the magnetic field is more distinctive in more peripheral collisions. In Figure 16 (b), we also show the relative difference in the initial eccentricity, R_{ϵ_2}, obtained from the Monte Carlo Glauber simulation. R_{ϵ_2} is highly consistent with 0 for peripheral events, and goes above (below) 0 for the parameter set of case 1 (case 2) in central collisions, because the Ru (Zr) nucleus is supposedly more deformed. The relative difference in υ_2 should closely follow that in eccentricity, so for the centrality range of interest, 20–60%, the flow-related backgrounds stay almost the same for Ru+Ru and Zr+Zr collisions. The slightly non-zero effect will be taken into account in the significance estimation for the CME signal projection, to be discussed later.

For convenience, we define the charge-separation observable $S \equiv \Delta\gamma \times N_{\text{part}}$. The focus of the isobaric collisions is to lift the degeneracy between Ru+Ru and Zr+Zr, therefore we express the corresponding S with a two-component perturbative approach to emphasize the relative difference the relative difference

$$S^{\text{Ru+Ru}} = \bar{S}\left[(1-bg)(1+\frac{R_{B_{sq}}}{2}) + bg(1+R_{\epsilon_2})\right],$$
$$S^{\text{Zr+Zr}} = \bar{S}\left[(1-bg)(1+\frac{R_{B_{sq}}}{2}) + bg(1-R_{\epsilon_2})\right], \qquad (6)$$

where $bg \in \epsilon_2$ [0, 1] quantifies the background contribution due to elliptic flow and $\bar{S} = S^{\text{Ru+Ru}} + S^{\text{Zr+Zr}})/2$. An advantage of this approach is that $R_S = (1-bg)R_{B_{sq}} + bg \cdot R_{\epsilon_2}$, which is little affected by the detailed implementation of $\bar{S}$. Without loss of generality,we parametrize $\bar{S}$ based on the STAR measurements of $S^{\text{Au+Au}}$ at 200 GeV [46] as a function of $B_{sq}^{\text{Au+Au}}$, and show in Figure 17 (a) the projection of $S^{\text{Ru+Ru}}$ and $S^{\text{Zr+Zr}}$ at 200 GeV, as functions of centrality, with B_{sq} and ϵ_2 obtained for case 1, and the background level of 80%. The statistical errors are estimated based on 1.2×10^9 minimum bias events for each collision type.

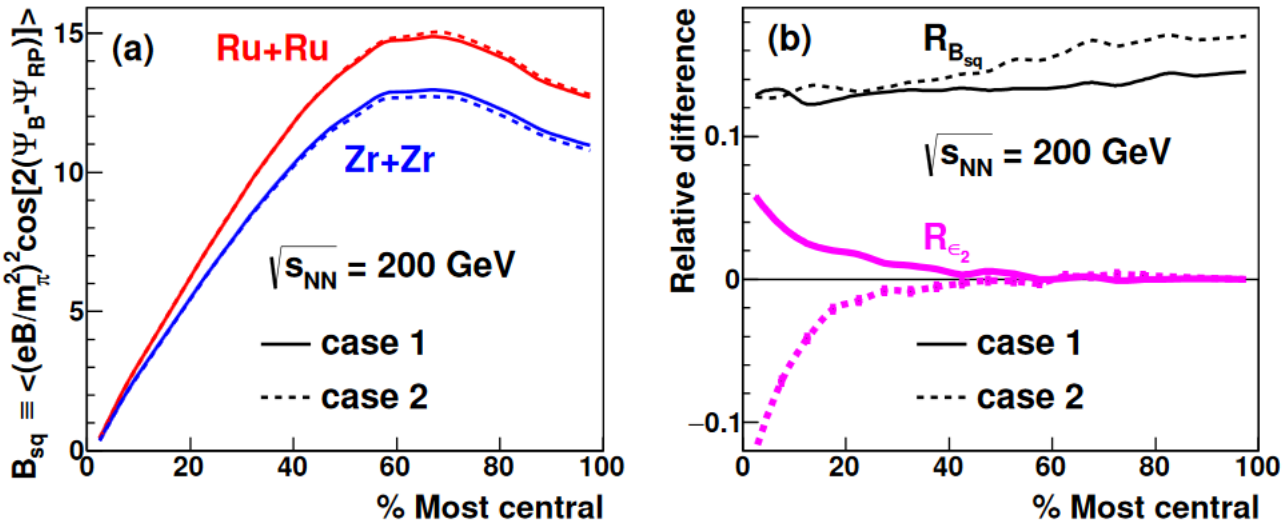

Figure 16: Theoretical calculation of the initial magnetic field squared with correction from azimuthal fluctuation

for Ru+Ru and Zr+Zr collisions at $\sqrt{s_{NN}}$ = 200 GeV (a) and their relative difference (b) versus centrality. Also shown is the relative difference in initial eccentricity (b). The solid (dashed) curves correspond to the parameter set of case 1 (case 2). [63]

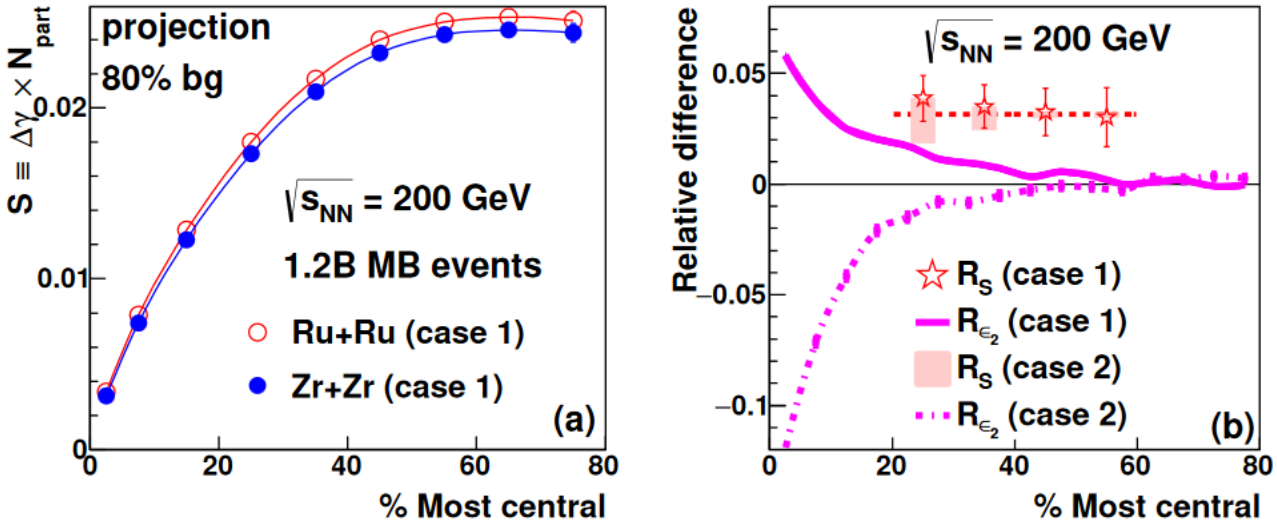

Figure 17: Projection of $S \equiv \Delta\gamma \times N_{\text{part}}$ for Ru+Ru and Zr+Zr collisions at $\sqrt{s_{NN}}$ = 200 GeV for the parameter set of case 1 (a) and the relative difference in the two (b) versus centrality, assuming the background level to be 80%. The statistical errors are estimated from 1.2×10^9 minimum bias events for each collision type. Also shown in panel (b) is the relative difference in the initial eccentricity from the Monte Carlo Glauber simulation (pink solid and dashed curves).

The systematic uncertainties in the projection are largely canceled out with the relative difference between Ru+Ru and Zr+Zr, shown in Figure 17 (b); in comparison, we show again the relative difference in eccentricity. For both parameter sets of the Glauber inputs (red stars for case 1 and pink shaded boxes for case 2), the relative difference in S is about 3% for centrality range of 20–60%. When we combine the events of 20–60% centralities, R_S is 5σ above R_{ϵ_2} for both parameter sets of the Glauber inputs. Therefore, the isobaric collisions provide a unique test to pin down the underlying physics mechanism for the observed charge separation. As a by-product, υ_2 measurements in central collisions will discern which information source (case 1 or 2) is more reliable regarding the deformity of the Ru and Zr nuclei.

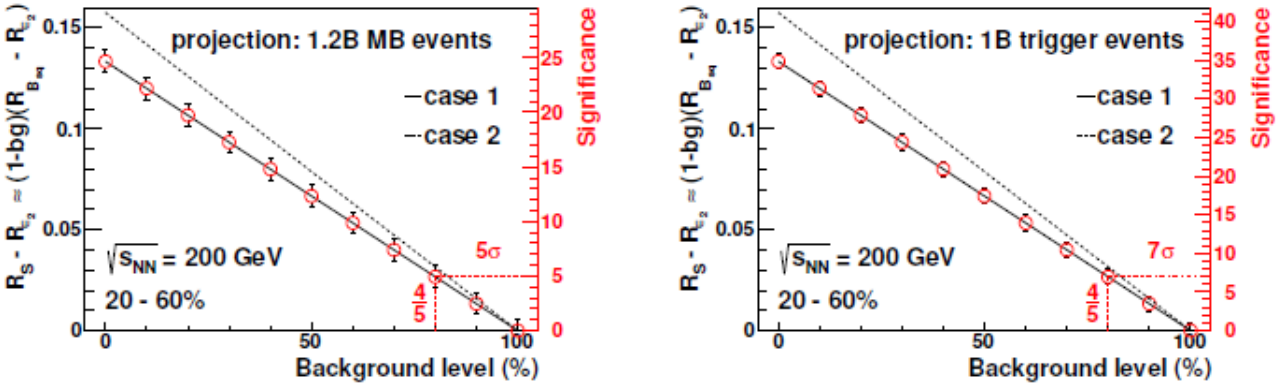

Figure 18: Magnitude (left axis) and significance (right axis) of the relative difference in the CME signal between Ru+Ru and Zr+Zr at 200 GeV, $R_S - R_{\epsilon_2}$ as a function of the background level. Results are estimated with event planes from TPC, based on 20–60% collisions selected from 1.2×10^9 minimum bias events (left) or 10^9 specially triggered events (right).

Given a specific background level, the magnitude and significance of the projected relative difference between Ru + Ru and Zr+Zr can be estimated accordingly, as shown in Figure 18 based on 20–60% collisions selected from 1.2×10^9 minimum bias events (left) or 10^9 specially triggered events (right). The measurements of the isobaric collision data will determine whether there is a finite CME signal observed in the correlator y, and if the answer is "yes", will ascertain the background contribution, when compared with this figure. The above results assume the event plane comes from the TPC.

In reality of data taking, the good event rate is about 80%, which converts the requested 1.2 billion into 1.5 billion events. A rough estimate for the RHIC operation to achieve 1.5×10^9 events will be 3.5 weeks for each collision system. For the CME analysis, the focus is on the centrality range of 20–60%, therefore a dedicated trigger for mid-peripheral collisions will be very helpful to increase the "useful" statistics. Both the existing Time-of-Flight and the expected EPD are fast detectors that can utilize the particle multiplicity to trigger on events within a wide centrality interval. We propose to take 1 billion events with this trigger and 200 million minimum bias events for each collision type. This trigger is expected to double the useful statistics, and improve the signal significance by a factor of $\sqrt{2}$ as shown in Figure 18 (right).

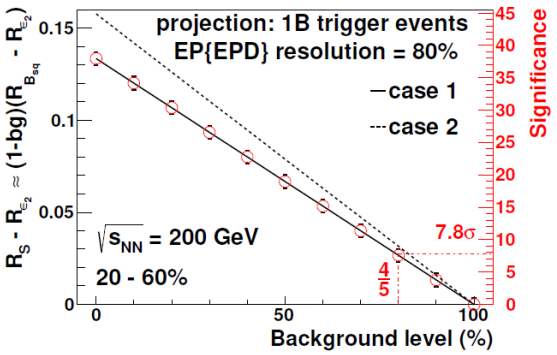

Figure 19: Magnitude (left axis) and signif- icance (right axis) of the relative difference in the CME signal between Ru+Ru and Zr+Zr at 200 GeV, $R_S - R_{\epsilon_2}$ as a function of the background level. Results are estimated with event planes from EPD, based on 20–60% collisions selected from 10^9 specially triggered events.

The new Event Plane Detector (EPD) was installed in STAR (see Appendix 2). The pseudorapidity coverage of EPD ($2.1 < |\eta| < 5.1$) better suppresses the non-flow contributions than the TPC event plane, providing an important systematic check for the γ measurements. What's more, with the estimated event plane resolution of ~ 80% in the isobaric collisions, the results with the EPD event plane will achieve a better significance than those with the TPC event plane at a specific background level, as shown in Figure 19.

2.1.2 Dilepton Production at Very Low Transverse Momenta

Dileptons (l^+l^-) are produced throughout the medium's evolution and escape with minimum interaction with the strongly interacting medium. Therefore, l^+l^- pair measurements play an essential role in the study of the hot and dense nuclear matter created in heavy-ion collisions. Dileptons in the low invariant mass region (up to $M_{ll} \sim 1$ GeV/c^2) retain information about the in-medium modification of vector mesons while dileptons in the intermediate mass region

(extending out to M_{ll} ~ 3 GeV/c^2) predominantly originate from charm decays and thermal radiation of the medium.

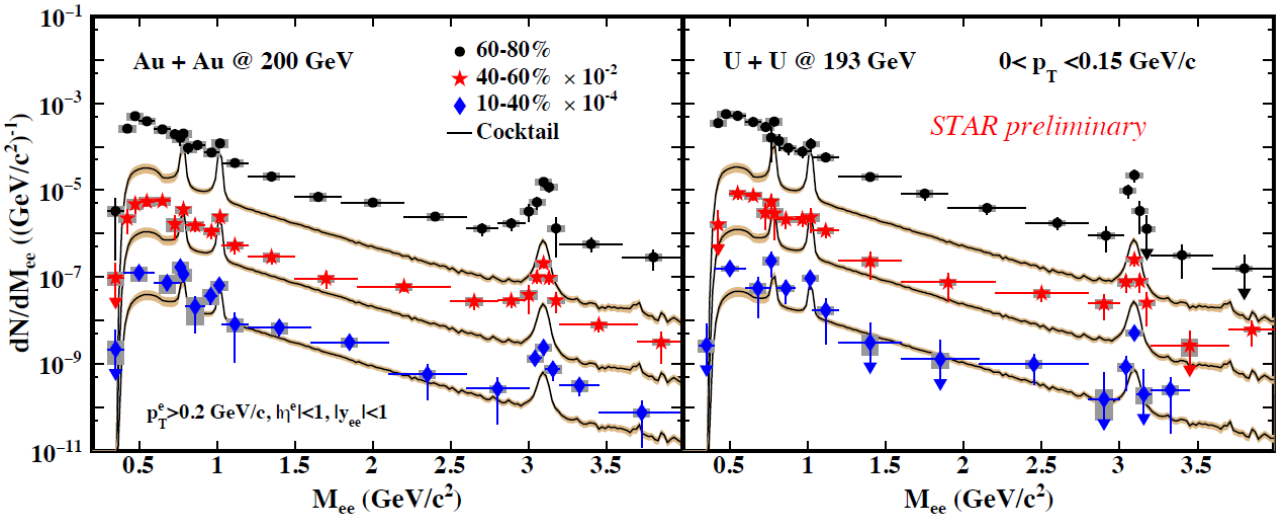

Figure 20: The low p_T (0 < p_T < 0.15 GeV/c) e^+e^- invariant mass distribution for Au+Au collisions at 200 GeV (left) and U+U collisions at 193 GeV (right). The invariant mass distributions for collisions with 60–80%, 40–60%, and 10–40% centrality are shown. For each centrality the corresponding hadronic cocktail contribution is shown as a solid curve with the uncertainty as a shaded region.

Figure 20 shows the e^+e^- invariant mass distribution from Au+Au collisions at 200 GeV and U+U collisions at 193 GeV for p_T < 0.15 GeV/c. The e^+e^- invariant mass distribution is shown for 60–80%, 40–60%, and 10–40% collision centralities. For each case the expected contribution from hadronic sources (excluding the ρ meson) is shown as a solid black curve. In 60–80% Au+Au and U+U collisions there is a significant excess visible with respect to the corresponding hadronic cocktail. The excess is less significant in 40–60% collisions and the data from 10–40% collisions are consistent with the expectation from the hadronic cocktail. The excess yield with respect to the hadronic cocktail is shown in Figure 21 for 60–80% Au+Au and U+U collisions along with the additional contributions expected from an in-medium modified ρ and thermal radiation from the QGP. The sum of these additional contributions is insuffcient to explain the observed excess.

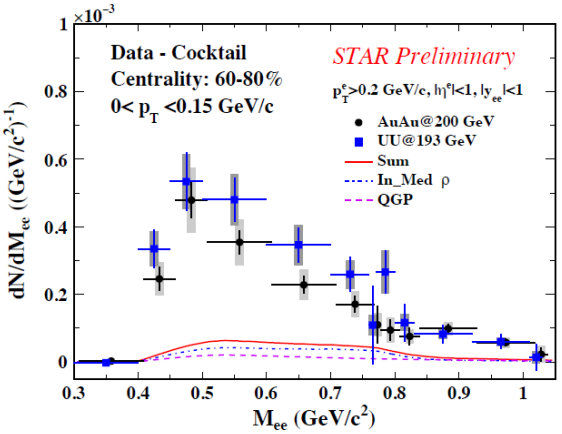

Figure 21: The low p_T e^+e^- excess yield with respect to the hadronic cocktail for Au+Au and U+U collisions with 60–80% centrality. The additional contributions expected from in-medium modified ρ production, QGP thermal radiation, and the sum of the two are shown.

There could be two sources contributing to the low- p_T dielectron enhancement in peripheral

collisions: photonuclear [69] and two-photon processes [70]. In the coherent vector meson photoproduction, a photon from the field of one nucleus fluctuates into a virtual quark-anti-quark pair which scatters elastically from the other nucleus, emerging as a real vector meson and then decaying into a dielectron pair. In a two-photon process, a photon from the field of one nucleus interacts from a photon from the other nucleus, emerging as a dielectron pair. These two processes have different dependences on the atomic number (Z) of the nucleus, with the photonuclear cross section proportional to Z^2 and the two-photon cross section proportional to Z^4. Hence, the isobaric collisions can help distinguish these two mechanisms.

Table 1: Results obtained from Monte Carlo Glauber calculations [52] for different collision systems. The magnetic fields are estimated at the time of the collisions (t = 0) and at the center of the participant zone. The multiplicity is obtained using a two-component model that is tuned to fit the Au+Au data.

Quantities Centrality (% most central)	U+U 60–80	Ru+Ru 47–75	Zr+Zr 47–75
Multiplicity ($\|\eta\| < 0.5$)	12–52	12–52	12–52
N_{part}	21 ± 1	21 ± 1	21 ± 1
B^2 (fm^{-1})	30.8 ± 0.1	30.1 ± 0.1	26.2 ± 0.1
B^4 (fm^{-1})	1984 ± 4	2121 ± 4	1672 ± 4

In a given heavy-ion collision, the cross sections of the above mentioned processes actually depend on the magnitude of the magnetic field produced by the protons in the colliding nuclei. In addition to Z, the produced magnetic field also depends on the distribution of the protons inside the colliding nuclei and the impact parameter of the collisions. For realistic estimations of the magnetic field, one must take into account the event-by-event variation. From the Monte Carlo Glauber calculations, we find that 60–80% U+U collisions will produce the same particle multiplicity as 47–75% Zr+Zr and Ru+Ru collisions [52], and therefore the same cocktail contributions and hot medium contributions to the dielectron production. On the other hand, $\langle B^2 \rangle$ and $\langle B^4 \rangle$ are different for these three collision systems. The ratio of $\langle B^2 \rangle$ in 47–75% Zr+Zr (Ru+Ru) over that in 60–80% U+U is 0.85 (0.98), while the ratio of $\langle B^4 \rangle$ is 0.84 (1.07). The results obtained from Monte Carlo Glauber calculations are summarized in Table 1.

Table 2: The expected dielectron data over cocktail ratios in the mass region 0.4–0.76 GeV/c^2 for p_T < 0.15 GeV/c with 1.2 billion minimum-bias isobaric collisions and the projected differences between Zr+Zr and Ru+Ru collisions for the two physics scenarios.

Physics process	data/cocktail 47–75% Ru+Ru	data/cocktail 47–75% Zr+Zr	Difference between Ru+Ru and Zr+Zr
Photonuclear	16.1 ± 0.4	14.3 ± 0.4	1.8 ± 0.6 (3.0σ)
Two-photon	17.4 ± 0.4	14.2 ± 0.4	3.2 ± 0.6 (5.3σ)

With all the above information, we estimate the dielectron data over cocktail ratios in the isobaric collisions with 1.2 billion good events and the projected differences between Ru+Ru and Zr+Zr collisions for the two physics scenarios. The results are shown in Table 2 and Table 3 for two different mass regions.

Table 3: The expected dielectron data over cocktail ratios in the mass region 3.0–3.2 GeV/c^2 for p_T < 0.15 GeV/c with 1.2 billion minimum-bias isobaric collisions and the projected differences between Zr+Zr and Ru+Ru collisions for the two physics scenarios.

Physics process	data/cocktail 47–75% Ru+Ru	data/cocktail 47–75% Zr+Zr	Difference between Ru+Ru and Zr+Zr
Photonuclear	20.0 ± 1.7	17.5 ± 1.7	2.5 ± 2.4 (1.0σ)
Two-photon	17.3 ± 1.7	21.8 ± 1.7	4.5 ± 2.4 (1.9σ)

2.2 Au+Au Collisions at 27 GeV

2.2.1 Global Polarization Measurements at 27 GeV

Global polarization can arise from spin coupling to both the fireball vorticity and the spectator magnetic field. Vortical coupling aligns emitted particle spin with the total system angular momentum, which can be partially transferred to the mid-rapidity fireball. Particle spins may also (anti-)align to the short lived magnetic field (in the same direction as the total angular momentum) via intrinsic magnetic moment coupling. The vortical coupling would be even with respect to baryon number, while the magnetic coupling would be odd. STAR has seen a positive (6σ) even signal and a small (1.5σ) odd signal for the $\Lambda-\overline{\Lambda}$ system in the BES-I data.

The magnetic field is poorly constrained by theory and entirely unmeasured experimentally. The primary theoretical uncertainty in our understanding of B-field effects [38] concerns its time evolution, which depends strongly on the electric conductivity of the plasma. Calculations with different conductivities differ by a few orders of magnitude [56]; the calculations with conductivity determined in the lattice QCD, yields fields (at the time of a few fm/c) eB of (a few)×10^{-2} m_π^2, similar to our equilibrium-based estimate.

In addition to being of fundamental interest on its own merits, the vorticity and magnetic field present during the evolution of a heavy ion collision are crucial inputs to the Chiral Vortical Effect (CVE) and Chiral Magnetic Effect (CME), respectively. These two effects are among the RHIC program's most exciting and visible topics today.

A conclusive discovery of chiral effects in heavy-ion collisions will generate great attention and press. Global hyperon polarization has nothing "chiral" about it. In a theoretically well-grounded fashion, it measures the average vorticity (ω) and field (B).

To test the hypothesis of a magnetically-induced splitting between the Λ and $\overline{\Lambda}$ global polarization, we propose to focus on a single energy and obtain high statistics there. Collisions at 19.6 GeV and lower energy will be obtained in the BES-II, so we focus on $\sqrt{s_{NN}}$ > 19.6 GeV. The high-statistics at one energy will also provide more differential study of possible p_T and rapidity dependence of the global polarization itself. This, in turn, would be important in clarifying potential difference in Λ and $\overline{\Lambda}$ global polarization due to stopping and final-state absorption.

At $\sqrt{s_{NN}}$ = 27 GeV we observe a 0.38σ difference between the Λ and $\overline{\Lambda}$ measurements, as can be seen in Figure 22. Also shown in Figure 22 are the expectations of the enhanced

statistical precision from 1B minimum bias events and inclusion of the EPD to determine the first order event plane. The statistical errors on these measurements go as $1/(R\sqrt{N})$, where N is the number of events and R is the reaction plane resolution. Given that the EPD will improve the first order event plane resolution by an approximate factor 2 at $\sqrt{s_{NN}}$ = 27 GeV, its installation will have a significant impact on this analysis [71]. An approximate factor 15 increase in statistics is therefore needed to realize a 3σ splitting in the hyperon polarization (assuming the central value stays fixed) driving our request for 1B minbias events.

While similar high-statistics measurements of global hyperon polarization will eventually be performed at lower energies in BES-II, the scientific impact of getting firm measures of vorticity and B much sooner is high, given the current intensity of research and discussion of CME and CVE oriented analyses. Meanwhile an isobar run with high statistics at low energy in the further future may be necessary if a splitting of hyperon and antihyperon polarization is observed. We are interested in a 2 day test run in 2018 with Zr+Zr collisions, which will determine the luminosity and STAR's data-taking capability of low energy isobar running. These test data will allow STAR to assess the potential of probing the magnetic field on the Λ polarization at energies where observation of the global polarization effect is optimal.

2.2.2 Dilepton Measurements at 27 GeV

In Figure 23, the preliminary acceptance-corrected excess spectrum for $\sqrt{s_{NN}}$ = 27 GeV is shown. Superimposed on the data points are projections of the improved uncertainties of our measurements for two scenarios. The uncertainties for each scenario are based on the measured preliminary uncertainties from the Run 11 run at 27 GeV. Furthermore, it includes the projected improvement of ~ 1.9 for the Au-beam luminosity in Run 18 at 27 GeV, as well as an estimate of the performance envelope of the STAR DAQ rates based on Run 15's performance (saturate at 1.7 kHz). The scenarios involve two cases: (i) running for 2 RHIC weeks at a data-taking effciency comparable to what was previously achieved for the same energy during Run 11 and (ii) running for 3 full weeks. These scenarios yield approximately 400M and 700M events that pass the analysis criteria for both scenarios, respectively.

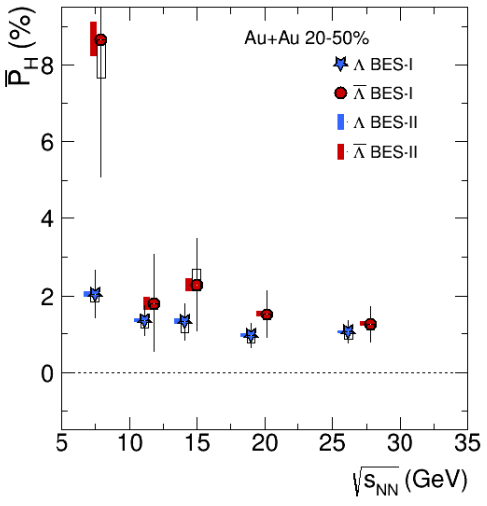

Figure 22: Comparison of the measured Λ and $\bar{\Lambda}$ global polarization as a function of $\sqrt{s_{NN}}$ to estimates of the enhanced precision of the measurements using 1B MB events and the EPD to enhance resolution of the first order plane.

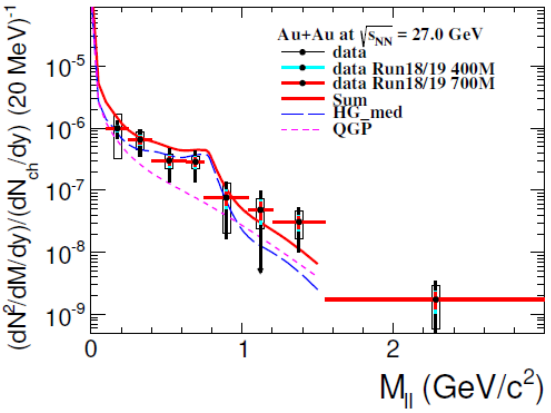

Figure 23: STAR preliminary measurement of the acceptance-corrected dielectron invariant mass spectrum for $\sqrt{s_{NN}}$ = 27 GeV. The hadron cocktail has been subtracted. The dotted and striped curves depict calculations by Rapp *et al.* that include a hadron gas (HG) and quark-gluon plasma (QGP).

As a result, we expect the average uncertainties to reduce by a factor of 2.4 (2-week scenario) up to 3.2 (3-week scenario). Model calculations [72] show that for dielectron masses above that of the ϕ meson the main contribution to the dielectron spectra arrives from the QGP component. The projected improvements in either scenario allow for a first measurement in this intermediate mass range, thus allowing a first potential measurement of the temperature of the hot medium at this energy.

2.3 Au+Au Collisions at 3 GeV

STAR requests two days (100 M events) of running at the fixed target energy of 3.0 GeV. More details of the entire fixed target program are given in Section 3.4. While in Run 18 the forward assets of the iTPC and the eTOF will not yet be available, at this low beam energy the rapidity of the center of mass is 1.05 units and the majority of the mid-rapidity particles are well within the acceptance of the detector in its current configuration. The primary goal of this run is to make a measurement of the higher moments of the net-proton distributions. This measurement will help determine if this $\kappa\sigma^2$ returns to unity at low energy, which was not seen in the recent HADES results. It is important to make this measurement in Run 18, as a 3.5 GeV Au+Au FXT target run is scheduled at NICA for 2019. One hundred million events will be needed because the significance of the $\kappa\sigma^2$ signal has been shown to scale as N^3 (where N is the net-proton multiplicity). The multiplicity of well identified protons measured in the 4.5 GeV FXT test run from Run 15 is one third of that in the 7.7 GeV BES-I data, therefore twenty-seven times higher statistics are needed to achieve a similar level of significance. There were four million good events taken in the the 7.7 GeV BES-I run; 27×4 M ≈ 100 M events are needed. Secondary purposes of taking an FXT data set in Run 18 are to verify the required conduct of operations (i.e. how often to dump the beam and whether the TPC needs to be turned off for dumps) and to optimize the FXT triggers and software.

3 Research Program: BES-II

In 2019 STAR proposes to initiate the BES-II. Specific details of the physics goals and required statistics at each energy are given below. In addition STAR is proposing a fixed target program to allow access to energies below those possible at RHIC in collider mode. In

2014 the STAR Collaboration released a white paper [73] in which it summarized the status of the analysis results from the first phase of the Beam Energy Scan (BES-I) and a proposed a second phase dedicated to low-energy running. In the following years, this white paper was followed by several detector-upgrade proposals [74, 75, 71] which in anticipation of Phase-II will significantly improve STAR's capabilities in terms of acceptance, effciency, and particle identification. At this time, the STAR collaboration has published more than 20 "BES-I results" papers. The results of these analyses are spectacular yet while they remain intriguing they do not allow for definite conclusions.

A disappearance of QGP signatures was indeed seen in the breakdown of constituent quark scaling of elliptic flow at beam energies below 19.6 GeV, in the disappearance of high p_T suppression for energies near 27 GeV and below, and in the collapse of charge separation that is attributed to the Chiral Magnetic Effect below 11.5 GeV, to name a few. There still remains some uncertainty in the interpretation of these observations, *i.e.*, it can be a challenge to unambiguously distinguish between a scenario where QGP production itself disappears, and the alternative picture in which our sensitivity to a QGP signature fades away. Hints of a first-order phase transition are seen in directed flow for protons and net- protons [76]. The measured directed flow signature at intermediate centralities has good statistical significance, but as will detailed in one of the next sections, the best available models show poor agreement with data and a clear physics interpretation requires further study. Meanwhile, searches for critical point signatures in particle ratio fluctuations and in the analysis of higher moments (skewness and kurtosis) of the multiplicity distribution of conserved quantities remain inconclusive, but arguably the net-protons kurtosis shows departure from monotonic dependence on $\sqrt{s_{NN}}$ expected in the absence of CP. These observations narrow-down the most promising region for future searches that will involve improved detectors and higher statistics.

The BES-II proposal requests high statistics (typically 20 times higher than BES-I), as set out in Table 4 for the BES-II beam energies currently envisaged. The searches for new physics will benefit substantially from a much larger rapidity acceptance, lower p_T thresholds, and improved *dE*/*dx* resolution, all provided by the iTPC upgrade see [74]. The endcap Time of Flight detector (eTOF) upgrade, [75], will enable the particle identification at higher momenta in the extended rapidity coverage. The proposed Event Plane Detector (EPD), [71] will allow the centrality and the event plane to be measured in the forward region, thus reducing the systematic errors due to autocorrelations from mid-rapidity analyses.

In the next subsections we describe the main goals of the proposed BES-II program.

3.1 Structure of the QCD Phase Diagram

3.1.1 Search for the Critical Point: Fluctuation Measurements

Thermodynamics indicates that QCD matter should exhibit a first-order phase transition ending in a critical point, with a crossover transition thereafter [77, 78]. The discovery of the critical point would be the most anticipated outcome of the BES program. Models suggest that the critical point might be signaled by large fluctuations in event-by-event multiplicities of conserved quantities such as net-baryon number, net charge, and net strangeness. These

quantities have variances $\langle (dN)^2 \rangle$ that are proportional to the correlation length (ξ) squared. Higher moments like skewness, $S \propto \langle (dN)^3 \rangle \sim \xi^{4.5}$ and kurtosis $\kappa \propto \langle (dN)^4 \rangle \xi^7$ vary more strongly with ξ and are argued to offer higher sensitivity to critical fluctuations [79, 80, 81].

Table 4: Event statistics (in millions) needed for BES-II for various observables. Taken from [73].

Collision Energy (GeV)	7.7	9.1	11.5	14.5	19.6
μ_B (MeV) in 0–5% central collisions	420	470	315	260	205
Observables					
R_{CP} up to p_T = 5 GeV/c	–		160	125	92
Elliptic Flow (ϕ mesons)	100	150	200	200	400
Chiral Magnetic Effect	50	50	50	50	50
Directed Flow (protons)	50	75	100	100	200
Azimuthal Femtoscopy (protons)	35	40	50	65	80
Net-Proton Kurtosis	80	100	120	200	400
Dileptons	100	160	230	300	400
Required Number of Events	100	160	230	300	400

Figure 24 presents $\kappa\sigma^2$ for net charge and net protons [82] (a proxy for net baryons) [83] at mid-rapidity as a function of beam energy for 0–5% centrality and for 70–80% centrality in Au+Au collisions. The net-charge $\kappa\sigma^2$ does not allow us to make strong statements because of the large uncertainties.

The net-proton $\kappa\sigma^2$ values for the 0–5% centrality selection at $\sqrt{s_{NN}}$ = 19.6 and 27 GeV are observed to deviate from: (a) the values from 70–80% peripheral collisions which are expected to create small systems which are dominated by two-to-two processes and do not show significant bulk properties; (b) Poisson and hadron resonance gas expectation values, which would correspond to uncorrelated emission and are close to unity; and (c) transport-model-based UrQMD [17, 84] calculations, which represent the expectations of expanding drops of finite hadronic matter which do not experience a phase transition. Within the current statistical uncertainties we cannot reach a conclusion about fluctuations attributable to a possible critical point. It is essential to re-visit these analyses with the greatly enhanced data to be acquired in BES-II.

Model calculations [85] suggest that the sensitivity of experimental moments analyses strongly depends on the detector's acceptance. The larger the acceptance, the more accurate is the extracted information on moments. STAR acceptance in net-proton cumulants (which are a proxy for net-baryon) is about 30% of the full phase space available for the final-state protons, while in the case of net-charge, it is about half of the full phase space. Due to the upgrades of BES-II, STAR acceptance will be extended by about 50%, significantly improving both analyses. Moreover, the additional STAR coverage will substantially reduce the size of the error on the measurement, effectively reducing the number of events required.

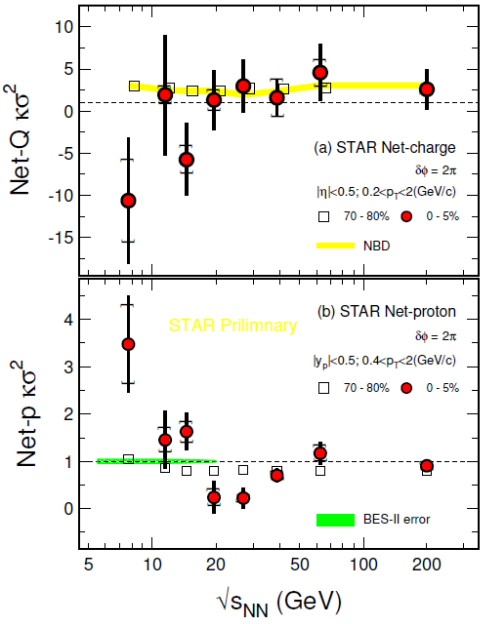

Figure 24: STAR results for beam energy dependence of $\kappa\sigma^2$ for net-protons (lower panel) and for net-charge (upper panel) in Au+Au collisions. Dotted horizontal lines are expec- tations from Poisson distributions. The green shaped band shows the estimated mid- rapidity statistical errors for the BES-II, assuming the requested events listed in Table 4. Thanks to the iTPC and eTOF, STAR's full capability here will be even better.

3.1.2 Search for the First-Order Phase Boundary: Measurement of Baryon Directed Flow

Directed flow excitation functions have been proposed by Frankfurt theorists as promising observables of evidence for a first-order phase transition, based on hydrodynamic calculations [7, 8, 86]. Figure 25 (left panel), based on a 3-fluid hydrodynamic model [8], presents directed flow for net-baryons as a function of beam energy. Note that the older $\langle px \rangle$ directed flow observable used here is proportional to v_1. A first-order phase transition leads to a softening of the Equation Of State (EOS), and this in turn causes the predicted proton directed flow to change sign from positive to negative near $\sqrt{s_{NN}}$ = 4 GeV. The directed flow prediction crosses back to positive again as the beam energy increases further. This phenomenon is referred to in the theory literature as the "softest point collapse" of flow [8].

Directed flow measured by STAR for net-protons is presented in the right panel of Figure 25, for Au+Au collisions at intermediate centrality [76]. The plotted quantity is the slope of $v_1(y)$ near mid-rapidity. The net-proton slope is a proxy for the directed flow slope of protons associated with baryon number transported from the initial state to the vicinity of mid-rapidity, based on the assumption that produced baryon-antibaryon pairs have similar directed flow and baryon-antibaryon annihilation does not alter the directed flow [76].

The net-proton slope shows a similar minimum to the predicted one, but at the collision energy in dv_1/dy about a factor 4 higher than the hydro prediction shown on the left in Figure 25. In contrast, there is no hint of this non-monotonic behavior in the UrQMD hadronic transport model [17, 84] (not shown) that has a good record of reproducing observed trends at least at a qualitative level. Theory comparisons that followed the publication of STAR's measurements of directed flow have overall not strengthened either the hadronic or the phase transition interpretations. Specifically, recent hydrodynamic calculations [12] confirm the

prediction on the left of Figure 25 but with a much larger magnitude of v_1 slope than the data, while hydro with a more realistic prescription for particle freeze-out has a much reduced minimum and no sign change [12]. A recent hybrid calculation by the same authors, featuring Boltzmann transport with an intermediate hydrodynamic stage, does not show a minimum or a sign change in v_1 slope for any assumed EOS [12]. The Parton-Hadron String Dynamics transport model does not show a minimum in v_1 slope for any assumed EOS [13].

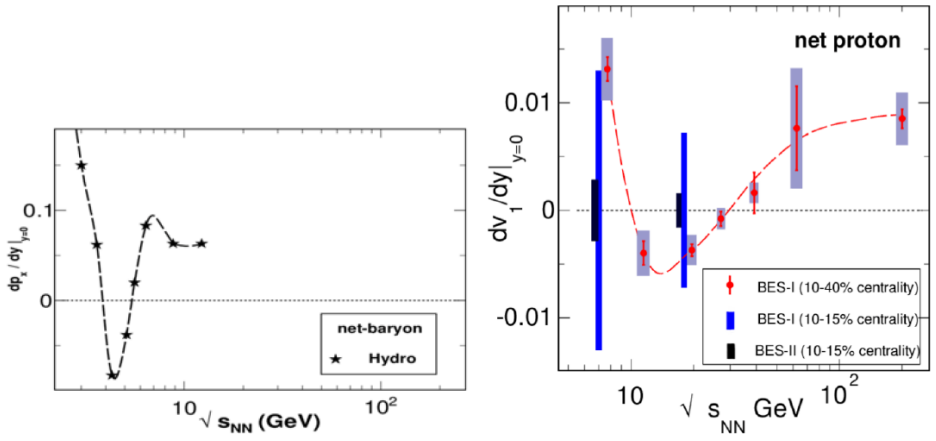

Figure 25: Left: Directed flow prediction in units of GeV/*c* as a function of beam energy, based on a three-fluid hydrodynamic model [8] whose EOS incorporates a first-order phase transition. Right: Comparison of BES-I 10–40% centrality measurement with 10–15% uncertainties and projected uncertainties for BES-II.

There is an important connection between the search for a first-order phase transition and the search for a critical point. A confirmed observation of a first-order phase transi- tion would imply that a critical point must exist, by ruling out a hypothesized scenario where the boundary between hadronic matter and QGP is a smooth crossover throughout the phase diagram. Such an observation would also have implications for the allowed and excluded locations in μ_B of the critical point. While model comparisons to date have underlined the importance of further theoretical work in order to reach a confident interpretation, new experimental data are also essential for a definitive conclusion.

Because of the strong non-monotonic behavior observed for protons and net protons, other baryon species like Λs are of special interest (see Sect. 1.2.5), and will have excellent statistics in BES-II. Although BES-I statistics are insuffcient for a systematic study of the centrality dependence of directed flow, it is noteworthy that at low BES energies, $v_1(y)$ magnitudes appear to increase roughly a factor of 5 when going from intermediate centralities to more peripheral centralities. Normally, anisotropic flow coeffcients exhibit far less centrality dependence over this range, and so this unusual pattern is highly deserving of targeted investigation in BES-II.

After the greatly improved BES-II measurements, any possible future explanation of v_1 data in terms of purely hadronic physics would have to predict the detailed phenomenology of the centrality, rapidity, and transverse momentum dependence of directed flow for various particle species as a function of beam energy. Simulations indicate that the improved statistics and extended rapidity acceptance, in combination with improved RHIC luminosity in the future, will be suffcient to meet this challenge. The restriction of measurements to the region near mid-rapidity is a serious limitation that must be overcome in order to reach a full

understanding of the physics.

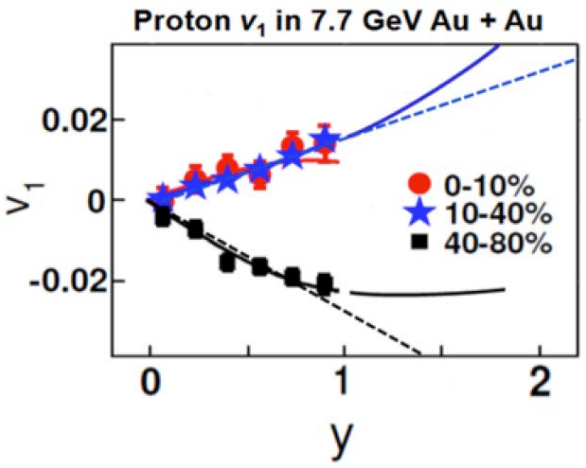

Figure 26: Plotted points show measured directed flow $\upsilon_1(y)$ for protons in three centrality bins for Au+Au collisions at $\sqrt{s_{NN}}$ = 7.7 GeV. The solid curves are a cubic fit to the measured data points for intermediate and peripheral centralities while the dashed lines are linear fits. For simplicity, only positive rapidities are plotted here.

Figure 26 illustrates the improved rapidity coverage of the iTPC via the extrapolated cubic and linear fits to $\upsilon_1(y)$ for protons at 7.7 GeV measured in BES-I. Clearly the extrapolation to higher rapidity is a major source of systematic error in this analysis and it will be significantly reduced by the extended rapidity coverage of BES-II. The most significant point of Figure 26 is that with the present rapidity coverage of the STAR TPC, $\upsilon_1(y)$ carries insuffcient information to go much, if at all, beyond a study of a single parameter like the slope $d\upsilon_1/dy$ averaged over the current rapidity acceptance, especially when statistics are limited. In contrast, the much wider $\upsilon_1(y)$ coverage of the iTPC opens the possibility to go well beyond a study of the single number yielded by the average slope just described. In light of the fact that proton and net-proton υ_1 near y = 0 have proven to be a highly promising signature, it is clearly of great interest and importance to extend the same form of analysis to the adjacent regions away from y = 0. The BES-I υ_1 measurements are based on the rather wide 10–40% centrality sample. The right-hand panel of Figure 25 compares these measurements with the associated uncertainties for the 10-15% centrality class and the expected impact of the proposed statistics for BES-II on the υ_1 measurement for the $\sqrt{s_{NN}}$ = 7.7 and 19.6 GeV collision energies. It is expected that such significantly reduced uncertainties will allow for definite conclusions.

3.1.3 Onset of Deconftnement: the Disappearance of QGP Signatures

Every QGP signature will benefit from extended η coverage, improved dE/dx and lowered p_T cut-off. Here we discuss, as an example, the improvement to elliptic flow analysis, which was intensively studied signature in BES-I.

There is evidence that a partonic phase is produced in the early stages of Au+Au collisions at top RHIC energies [1, 2, 3, 4]. Charting the evolution of the established partonic signatures with $\sqrt{s_{NN}}$ from 200 to 7.7 GeV should reveal the value of $\sqrt{s_{NN}}$ where these signatures

change or disappear completely. The observation that elliptic flow (expressed by the anisotropy parameter v_2) scales with the number of constituent quarks (NCQ) in a given hadron species indicates that the flow is established early in the collision process, when quarks are the relevant degrees of freedom. In contrast, if the flow had been established during a hadronic phase, then the magnitude of v_2 for each hadron species would scale with its mass. In Figure 27, the differences between particle and antiparticle v_2 for the six energies 7.7, 11.5, 19.6, 27, 39, and 62.4 GeV are shown.

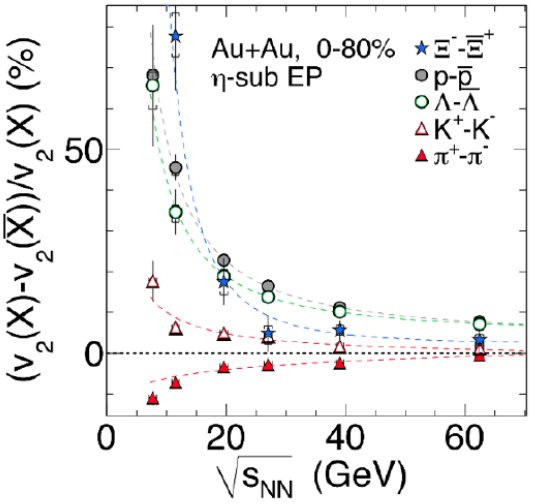

Figure 27: The difference in v_2 between particles and their antiparticles (see legend) as a function of $\sqrt{s_{NN}}$ for 0–80% central Au+Au collisions. The dashed curves are fits with a power-law function. The error bars depict the combined statistical and systematic errors.

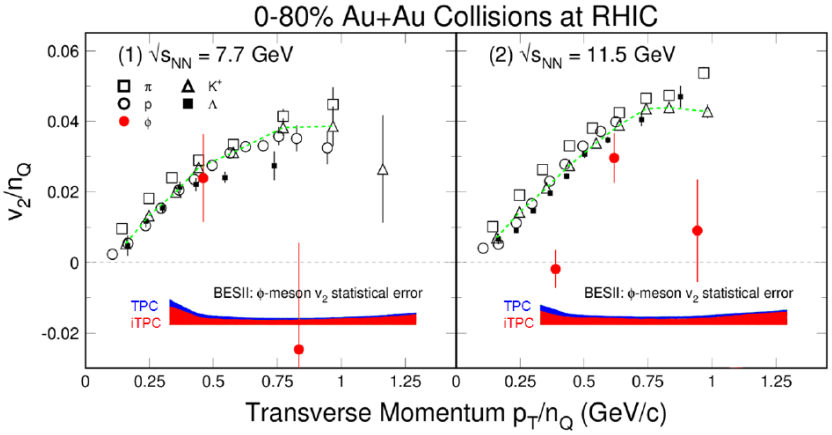

Figure 28: Scaled v_2 of the ϕ meson showing the projected error bars for BES-II with the current STAR TPC (blue band) and with the iTPC (red band).

The results suggest that NCQ scaling, first observed at $\sqrt{s_{NN}}$ = 200 GeV [24] may no longer hold at lower energies. As the energy is lowered, the violation of NCQ scaling becomes stronger, and the splitting between mesons and baryons becomes stronger. These observations are consistent with the expectation that the system spends a smaller percentage of the collision duration in the partonic phase as the beam energy is lowered, and that at the lowest BES energies, the system might not reach the QGP phase at all.

The study of the v_2 of particles with a very small hadronic cross section may elucidate to a

much higher degree the partonic dynamics and collectivity in heavy-ion collisions.

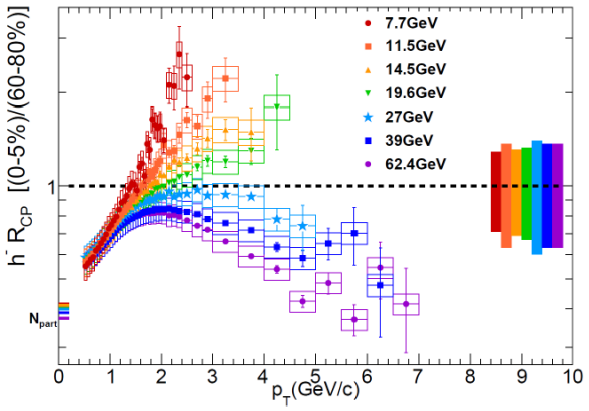

Figure 29: Nuclear modification factor versus transverse momentum for negatively charged hadrons from Au+Au collisions at various $\sqrt{s_{NN}}$ at RHIC. The yield ratios for charged hadrons are taken for 0–5% to 60–80% collision centrality.

The ϕ meson, which is a bound state of the s and $\bar{s}$ quarks, has a small interaction cross section with other hadrons, and freezes out early [87, 88]. Due to the small hadronic interaction cross section of the ϕ meson, its υ_2 is almost unaffected by later-stage hadronic interactions, and will have a negligibly small value if ϕ's are not produced via s and s quark coalescence in the partonic phase [89]. Therefore the elliptic flow of ϕ meson is particularly interesting because the entire magnitude of its elliptic flow is expected to originate from the partonic phase.

Figure 28 presents $\upsilon_2(p_T)$ at 7.7 and 11.5 GeV for several identified particle types, scaled on both axes by the number of constituent quarks. The ϕ meson result, the solid red circles with error bars, illustrate the fact that BES-I statistics for the ϕ are far less than what is needed to reach a useful physics conclusion at these two beam energies. The height of the red band in the lower part of each panel illustrates the expected error with BES-II statistics and with the enhanced midrapidity acceptance of the iTPC. If BES-II were to take data without the iTPC, the errors would increase by an amount represented by the blue band.

Another broadly discussed result from BES-I related to the onset of deconfinement is the R_{CP} measurement shown in Figure 29 (for all BES-I energies) and Figure 30(for 7.7, 11.5 and 19.6 GeV). The high- p_T suppression observed at the top RHIC energies is seen as an indication of the energy loss of leading partons in a colored medium, and the R_{AA} measurements are one of the clearest signatures for the formation of the quark-gluon plasma. Because there was not a comparable p+p energy scan, the BES analysis has had to resort to R_{CP} measurements as a proxy. Still the study of the shape of $R_{CP}(p_T)$ will allow us to quantitatively address the evolution of jet-quenching to lower beam energies.

A very clear change in behavior as a function of beam energy is seen in these data (see Figure 29); at the lowest energies (7.7 and 11.5 GeV) there is no evidence of suppression for thehighest p_T values that are reached. And while we do not expect to reach p_T range of ~ 5GeV/c for the lowest BES energies, we will be able with the BES-II statistics, to investigate identified particles in the intermediate p_T range, which may allow us to better understand the

Cronin effect and the evolution of R_{CP} (see Figure 30 and Table 4).

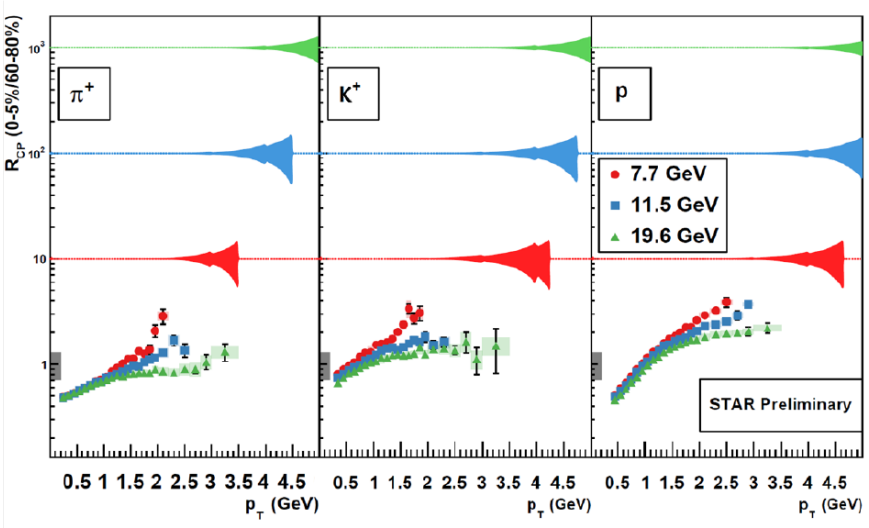

Figure 30: The BES-I R_{CP} data are are shown for p, K, and π for 7.7, 11.5, and 19.6 GeV. The BES-II projected error bands are for the same energies, 7.7 (red, scaled by 10), 11.5 (blue, scaled by 100), and 19.6 (green, scaled by 1000).

3.1.4 Search for Chiral Symmetry Restoration

Dileptons are a crucial probe of the strongly interacting matter created in ultrarelativistic heavy-ion collisions. Leptons are produced during the whole evolution of the created matter and can traverse the medium with minimal interactions. Different ranges in the kinematics of dilepton pairs (mass and transverse momentum ranges) can selectively probe the properties of the formed matter throughout its entire evolution. In the low invariant mass range of produced lepton pairs (M_{ll} < 1.1 GeV/c^2), the in-medium properties of vector meson (*i.e.* the mass and width of the $\rho(770)$, $\omega(782)$, and $\phi(1020)$ mesons) can be studied via dilepton decays and may exhibit modifications related to possible chiral symmetry restoration. Additionally, in the higher p_T range, direct photon yields have been derived through dielectron measurements at RHIC, allowing an assessment of thermal radiation. Large acceptance, precision experiments with a broad range of beam energies can provide invaluable insights in this subject.

The dilepton spectra in the intermediate mass range (1.1 < M_{ll} < 3.0 GeV/c^2) are expected to be directly related to the thermal radiation of the Quark-Gluon Plasma. However, significant background contributions from other sources have to be taken into account and measured experimentally. Such contributions include background pairs from correlated open heavy-flavor decays. It includes pairs of electrons or muons from the semileptonic decay of a pair of open charm or bottom hadrons, $c \rightarrow l^+l^-$ or $b \rightarrow l^+l^-$; both of which may be subject to in-medium modifications. In the high-mass region (M_{ll} > 3.0 GeV/c^2), J/ψ, Υ, and their excited states are used to study the color screening features of the QGP.

It has been generally accepted that the properties of the vector mesons change dramatically from vacuum to the hot and dense medium created in relativistic heavy ion collisions. Observations at SPS and RHIC indicated enhancements of the dilepton yields at low p_T and in the low invariant mass range between the π and ρ mass. These enhancements could not be described with model calculations that involve the vacuum ρ spectral function. The key question is how to connect this modification of the ρ meson to the possible chiral symmetry

restoration expected at the high temperatures achieved at RHIC and LHC. Dynamic models [90] show that the broadening of the width of the ρ can be attributed to interactions with the surrounding nuclear medium, *i.e.* to the coupling of ρ to the baryons and their resonances. These interactions affect the properties of the ρ even in the cold nuclear matter. In hot nuclear matter, where temperature and/or baryon density is high, these interaction are expected to cause the width to further broaden to the extent that it becomes indistinguishable from the radiation continuum. This continuum coincides with the dilepton thermal radiation from QGP at the phase transition temperature. Measuring the temperature dependence of the dilepton yields at low mass would thus be a key observable.

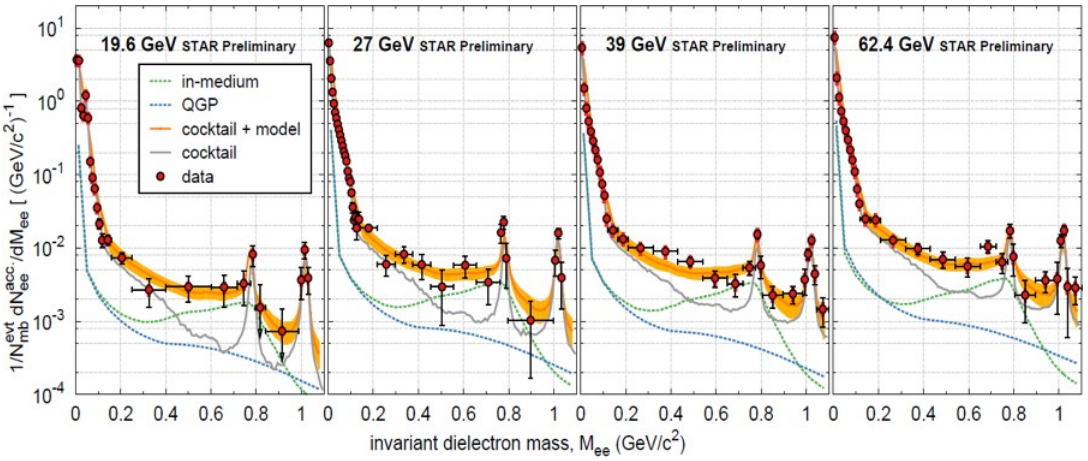

Figure 31: BES-1 preliminary results for the low-mass range dielectron invariant mass spectra at $\sqrt{s_{NN}}$ = 19.6, 27, 39, and 62.4 GeV (red circles). The curves show the empirical contributions from empirical hadronic sources and the sum with a model calculation by Rapp, *et al*. The dotted lines are the in-medium and QGP contributions.

In relativistic heavy ion collisions, the observed dilepton yields at low mass have contributions from many sources integrated over the entire evolution of a collision. During BES-I running, STAR has collected dielectron data for minimum-bias Au+Au collisions at $\sqrt{s_{NN}}$ = 19.6, 27, 39, and 62.4 GeV. Figure 31 shows the preliminary effciency-corrected dielectron invariant mass spectra for these four beam energies.

To help further disentangle the various factors that play a role in measuring the dielectron production in the low mass range, we show in Figure 32 the baryon density *vs.* the collision energy. Here, the total baryon density at freeze-out is approximated by the measured ratio of the sum of proton and antiproton yields over the sum of charged pion yields. The plot shows that above approximately 20 GeV the total baryon density remains almost independent of the beam energy. Consequently, the medium effect on the ρ meson and its dielectron spectrum are independent of beam energy when the dielectrons are emitted close to freeze-out. On the other hand, both the temperature and baryon density at the earlier stage of the collision strongly depend on the beam energy. This, and the lifetime of the system are expected to impact the measured dielectron yields, and could result in measurable anomalies [91].

The dielectron measurements in BES-I have served as an important bridge between those at top SPS and top RHIC energies, and provide an effective tool to study the temperature dependence of the ρ spectral function. These data are used to test models that involve a broadened ρ meson. Using these broadened ρ spectral function, verified against inputs from Lattice QCD through Weinberg/QCD sum rules, theorists have demonstrated [92] that when the temperature reaches 170 MeV, the $a_1(1260)$ spectral function is the same as the ρ spectral

function. This is a signature of chiral symmetry restoration as the axial vector meson $a_1(1260)$ is considered to be the chiral partner of the ρ meson.

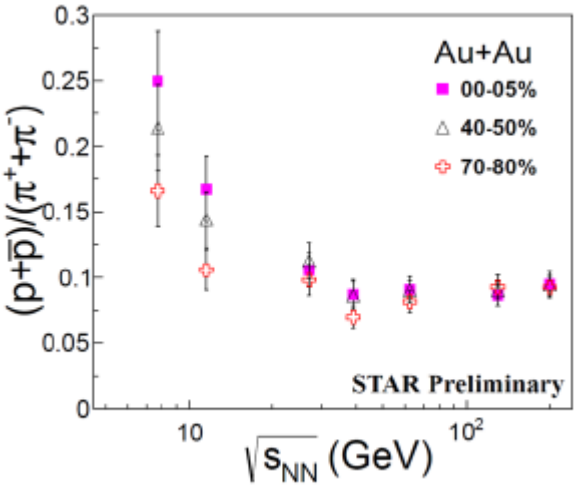

Figure 32: Total baryon density, represented by $(p+\bar{p})(\pi^+ + \pi^-)$, *vs.* collision energy.

As can be seen from Figure 32, further lowering the collision energy will see, in addition to a change in temperature, a significant change in the total baryon density at freeze-out. STAR proposes to measure the low-mass range dielectron spectrum down to 7.7 GeV in order to further test the yields against models that connect the broadening of the ρ meson to chiral symmetry restoration. At the same time, measurements of the intermediate mass range will allow STAR to determine how this range may smoothly transition and match to the p_T slopes in the low-mass range. While the charm contribution in the low-mass range will significantly drop with lower collision energies, these rates continue to dominate the intermediate mass range. During BES-II the STAR's muon detection capabilities will allow for independent measurements, through e–μ correlations, of the charm contribution to the dilepton continuum. Finally, one can also change the total baryon density by shifting the analysis frame from midrapidity towards a more forward rapidity. The combination of the iTPC and eTOF will allow electron identification to be pushed out to larger rapidities (see rightmost panel of Figure A4.2 in Appendix 2). The rapidity dependence of the total baryon density will provide a strong and independent observable to study the baryon density's dependence of the low-mass dielectron emission.

3.1.5 Charged Hadron Spectra and Parton Energy Losses

The transverse momentum spectrum of hadrons produced in high-energy collisions of heavy ions reflects features of constituent interactions in the nuclear medium. The medium modification is one of the effects (recombination, coalescence, energy loss, multiple scattering,...) that affects the shape of the spectrum. The properties of the created medium are experimentally studied by variation of the event centrality and collision energy.

STAR has measured spectra of negative charged particle production in Au+Au collisions for the first phase of the RHIC Beam Energy Scan Program over a wide range of collision energy $\sqrt{s_{NN}}$ = 7.7–200 GeV, and transverse momentum of produced particle in different centralities at $|\eta| < 0.5$. The spectra demonstrate strong dependence on collision energy which enhances

with p_T. The constituent energy loss as a function of energy and centrality of collisions and transverse momentum of inclusive particle was estimated in the *z*-scaling approach. The energy dependence of the model parameters – the fractal and fragmentation dimensions and "specific heat" was studied.

Figure 33 shows the negatively charged hadron yields in Au+Au collisions at $\sqrt{s_{NN}}$ =7.7, 11.5, 19.6, 27, 62.4 and 200 GeV at mid-rapidity $|\eta| < 0.5$ as a function of transverse momentum p_T. The results are shown for the collision centrality classes of 0–5%, 5–10%, 10–20%, 20–40%, 40–60%, 60–80%. The distributions are measured over a wide momentum range $0.2 < p_T < 12$. GeV/*c*. The multiplied factor of 10 is used for visibility. As seen from Figs. 3 spectra fall more than eight orders of magnitude. Spectra demonstrate a strong dependence on collision energy and centrality at high p_T.The exponential behavior of spectra at low p_T and the power behavior of spectra at high p_T are observed.

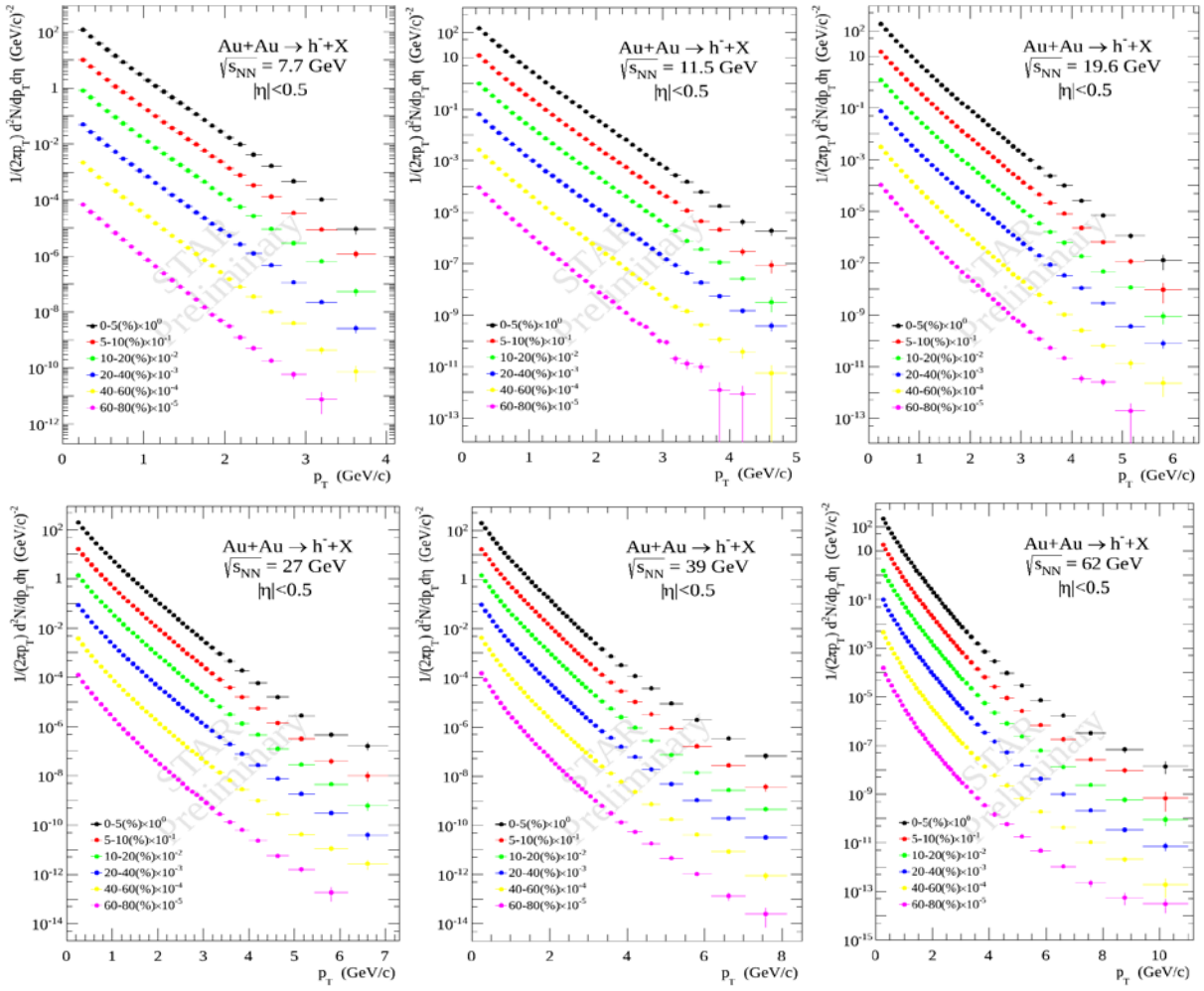

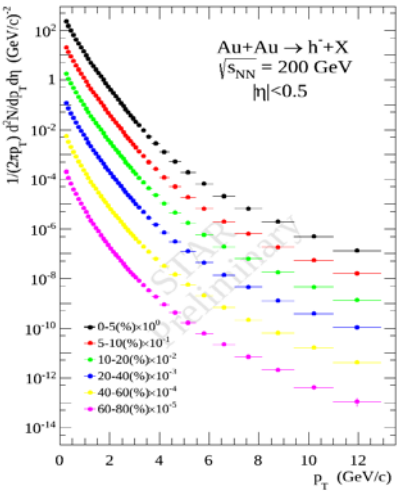

Figure 33: Transverse momentum distribution of negative charged particles production at BES energies 7.7, 11.5, 19.6, 27, 39, 62 and 200 GeV as a function of centrality.

As one seen from Figure 33 shows the the negatively charged hadron yields in Au+Au collisions at $\sqrt{s_{NN}}$ =7.7, 11.5, 19.6, 27, 62.4 and 200 GeV at mid-rapidity $|\eta| < 0.5$ as a function of transverse momentum p_T. The results are shown for the collision centrality classes of 0−5%, 5−10%, 10−20%, 20−40%, 40−60%, 60−80%. The distributions are measured over a wide momentum range $0.2 < p_T < 12$. GeV/*c*. The multiplied factor of 10 is used for visibility. As seen from Figure 33 spectra fall more than eight orders of magnitude. Spectra demonstrate a strong dependence on collision energy and centrality at high p_T.The exponential behavior of spectra at low p_T and the power behavior of spectra at high p_T are observed.

In Figure 33 the data demonstrates strong energy and centrality dependence of spectra, exponential behavior of the spectra at low p_T and energy $\sqrt{s_{NN}}$, a power behavior of spectra at high p_T and energy $\sqrt{s_{NN}}$. One observes that difference of yields at various energies strongly increases with transverse momentum.

The JINR team of the STAR collaboration takes part in the analysis of the BES-I data. The original method of data analysis (*z*-scaling approach) has been suggested and exploited for search for new phenomena in nuclear matter created in heavy ion collisions. The analysis of the obtained spectra has been performed in the framework of the *z*-scaling approach (Phys. Rev. D75, 2007, 094008; Int. J. Mod. Phys. A24, 2009, 1417; Nucl. Phys. Suppl. B245, 2013, 231).

The study of critical phenomena in nuclear matter is most preferable in terms of dimensionless variables. The idea of the Beam Energy Scan programs at RHIC is to vary the collision energy and look for the signatures of QCD phase boundary and QCD critical point i.e. to span the phase diagram from the top RHIC energy to the lowest possible energy. Turn-off of signatures of QGP established at $\sqrt{s_{NN}}$ = 200 GeV would suggest the crossing of phase boundary. Self-similarity of hadron interactions is assumed to be a very fruitful concept to study collective phenomena in the hadron and nuclear matter. Important manifestation of this concept is a notion of scaling itself. Scaling in general means self-similarity at different scales. The approach based on *z*-scaling is treated as manifestation of the self-similarity property of the

structure of colliding objects (hadrons, nuclei), the interaction mechanism of their constituents, and the process of constituent fragmentation into real hadrons. The approach relies on a hypothesis about self-similarity of hadron interactions at a constituent level. The assumption of self-similarity transforms to the requirement of simultaneous description of transverse momentum spectra corresponding to different collision energies, rapidities, and centralities by the same scaling function $\Psi(z)$ depending on a similarity parameter z. The scaling function for the collision of nuclei is expressed in terms of the experimentally measured inclusive invariant cross section, the multiplicity density, and the total inelastic cross section.

The function $\Psi(z)$ is interpreted as a probability density to produce an inclusive particle with the corresponding value of z. The similarity parameter z is expressed via momentum fractions (x_1, x_2, y_a, y_b), multiplicity density, and model parameters interpreted as fractal dimension of colliding particle (nuclei) and "specific heat" of produced matter. The constituents of the incoming nuclei carry fractions x_1, x_2 of their momenta. The inclusive particle carries the momentum fraction y_a of the scattered constituent. Simultaneous description of different spectra with the same $\Psi(z)$ puts strong constraints on the values of these parameters, and thus allows for their determination. The fractal dimension of the nucleus is expressed in terms of the nucleon fractal dimension (δ) and the atomic number of nucleus (A) as follows, $\delta_A = A \cdot \delta$. The fragmentation fractal dimension in nucleus-nucleus collisions is parameterized in the form: $\varepsilon_{AA} = \varepsilon_0(dN/d\eta) + \varepsilon_{pp}$. It depends on multiplicity density and nucleon fragmentation dimension ($\varepsilon_{pp} = 0.2$). Here ε_0 is a fitting parameter. In this approach the energy loss of the scattered constituent during its fragmentation in the inclusive particle is proportional to the value $(1-y_a)$. We would like to emphasize once more that dimensionless quantities, like momentum fractions, a scaling function and similarity parameter, are expressed via dimensional experimental measurable quantities.

Figure 34 shows scaling function $\Psi(z)$ as a function of self-similarity parameter z. The data z presentation corresponds to spectra of negatively charged particles produced in Au+Au collisions at energies $\sqrt{s_{NN}}$ = 7.7–200 GeV in the range $|\eta| < 0.5$ for most central (0–5%) and peripheral (40–60%) events as a function of the transverse momentum. We observe "collapse" of the data onto a single curve. The solid line is a fitting curve for these data. The derived representation shows the universality of the shape of the scaling curve for the BES-I energies. The found regularity (the shape of the function and its scaling behavior in the wide kinematic range) can be treated as manifestation of the self-similarity of the structure of colliding objects, interaction mechanism of their constituents, and processes of fragmentation of these constituents into real registered particles. As we can see from
Figure 34, the scaling function exhibits two kinds of behavior: one in the low-z and the other in the high-z region. The first regime corresponds to saturation of the scaling function with the typical flattening out. The second one corresponds to the power behavior of the scaling function pointing on self-similarity in constituent interactions at small scales. The energy dependence of the fractal and fragmentation dimensions and "specific heat" was found.

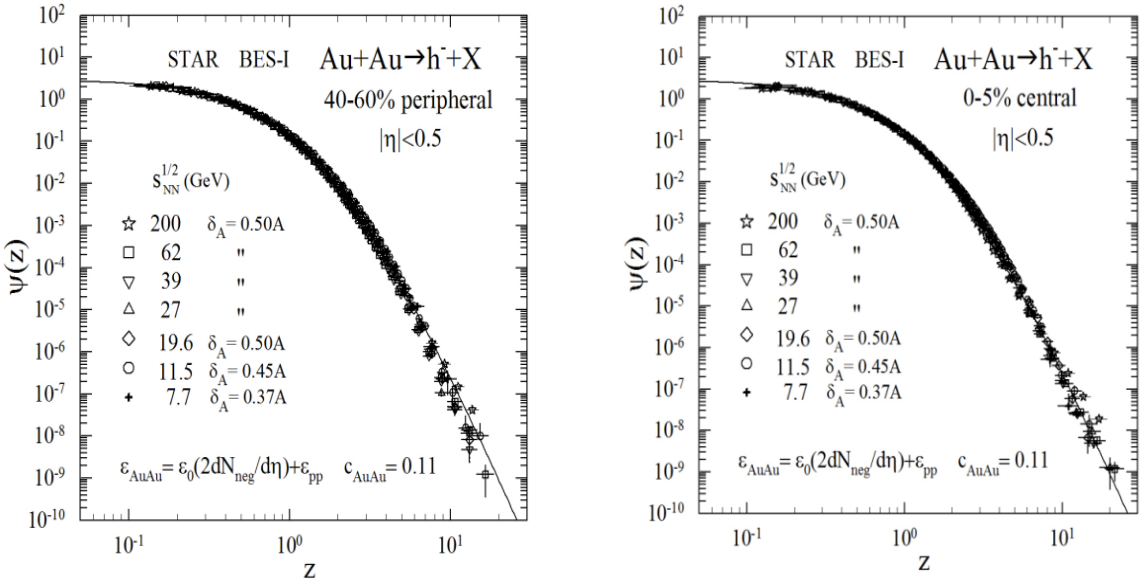

Figure 34: *z*-presentation of transverse momentum distribution of negative charged particle production at BES energies 7.7, 11.5, 19.6, 27, 39, 62.4, and 200 GeV at most central (0–5%) and peripheral (40–60%) centralities and central rapidity range ($|\eta|$<0.5).

The nuclear modification factor R_{AA} measured at RHIC at $\sqrt{s_{NN}}$ = 62.4, 130 and 200 GeV strongly shows a suppression of the charged hadron spectra at p_T > 4 GeV/*c*. This suppression was one of the first indications of a strong final-state modification of particle production in Au+Au collisions that is now generally ascribed to energy loss of the fragmenting parton in the hot and dense medium. At the BES-I energies the nuclear modification factor drastically changes with a collision energy. It increases with transverse momentum as the energy decreases. The study of the evolution of the energy loss with collision energy has relevance to the evolution of created nuclear matter, and can be useful for searching for signature of phase transition and a critical point. The measured spectra (see Figure 34) allow us to estimate constituent energy loss in charged hadron production in Au+Au collisions at BES energies. The estimations are based on a microscopic scenario of particle production in the frameworh of *z*-scaling approach. The energy loss $\Delta E/E$ of the scattered constituent during its fragmentation in the inclusive particle is proportional to the value $(1-y_a)$.

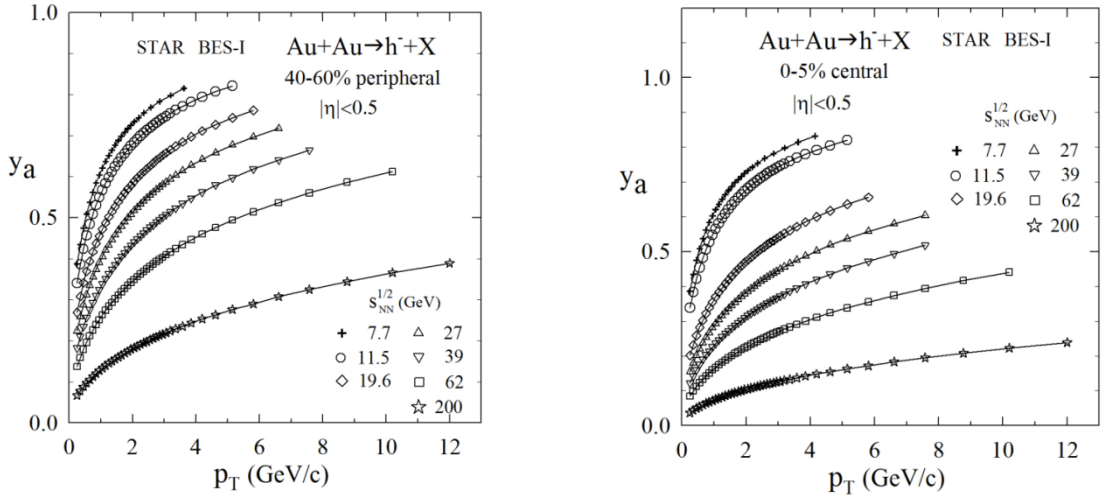

Figure 35: Momentum fraction y_a as a function of the energy and centrality of collision and the transverse momentum of inclusive particle.

Figure 35 shows the dependence of the fraction y_a for central (0–5%) and peripheral (40–60%) Au+Au collisions on the transverse momentum over a range $\sqrt{s_{NN}}$ = 7.7–200 GeV. The behavior of y_a demonstrates a monotonic growth with p_T. It means that the energy loss associated with the production of a high- p_T hadron is smaller than that with lower transverse momenta. The decrease of y_a with collision centrality represents larger energy loss in the central collisions as compared with peripheral interactions. The energy dissipation grows as the collision energy increases. It is estimated to be about 20% at $\sqrt{s_{NN}}$ = 7.7 GeV and 85% at $\sqrt{s_{NN}}$ = 200 GeV for at $p_T \approx 4$ GeV/c for central events (0–5%), respectively. These estimations are in agreement with the energy dependence of the model parameters (see Figure 35). Discontinuity of these parameters was assumed to be a signature of phase transition and a critical point.

3.2 Improvements in the Coverage of Phase Space and the Determination of Freeze-Out Parameters

Statistical-thermal models have proven to be very successful in describing particle multiplicities observed in relativistic collisions of heavy ions and elementary particles. These models permit the use of experimental particle yields as input and can calculate corresponding thermodynamic parameters such as chemical freeze-out temperature T_{ch} and baryon chemical potential μ_B.

The critical region in μ_B has been predicted to span on the order of 100 MeV [93], which suggests that the program of measurements in Phase-I of the Beam Energy Scan offers reasonable coverage along the μ_B axis from a few tens of MeV up to at least 400 MeV. Furthermore, this interval is predicted to encompass the location of the critical point, if it exists [93]. On the other hand, the Phase-I measurements are subject to basic limitations that strongly motivate a new set of measurements with improved capabilities. Extending the acceptance at low p_T will allow STAR to reduce the fraction of the extrapolated yield which will subsequently be reflected in a similar improvement of the extracted freeze-out parameters.

Current STAR measurements of freeze-out parameters show some deviations from other published data [5], due in part to the fact that the current TPC only offers mid-rapidity coverage. It has been well established that protons have a broader distribution in rapidity than those of mesons or anti-baryons due to partial stopping [94]. As baryon stopping is the key feature in the increase in μ_B at lower energies, it is essential to measure the full proton rapidity distributions [95]. The extended TPC coverage for BES- II will allow proton rapidity density measurements to made to 1.6 units of rapidity which (ignoring spectator protons) accounts for 70% of the proton yield at $\sqrt{s_{NN}}$ = 19.6 GeV. Vertices displaced in z from the center of the detector allow one to further extend the coverage to 2.3 units of rapidity. This extended range will allow (on a statistical basis) for almost 4π measurements of particle yields, improving constraints on the thermodynamics.

Improving the low p_T coverage also makes possible new physics analyses. A study that is made possible only with the lower p_T thresholds of the iTPC involves measurement of the effect of the Coulomb acceleration of the pions. The effect is seen as an enhancement of ratio

of π^-/π^+ for p_T below 100 MeV [96]. By studying the details of the low-p_T pion spectra, one can determine the Coulomb potential of the source, which is related to the stopping of the protons as these participating protons bring a net positive charge to the interaction region [97].

3.3 Key Measurements for BES-II

The BES-I scientific program has localized the most interesting regions and has identified the observables which are likely to be the most discriminating for understanding the QCD phase structure. However, several of the key measurements were found to require higher statistics in order to provide a quantitative physics conclusion. Therefore, we propose to run a second phase of the beam energy scan (BES-II) which is driven by the precision requirements of this suite of physics observables. In Table 4 [73] we outline the event statistics that is required to make a precision measurement of each proposed observable at each proposed energy.

The main driver for the numbers of events needed in BES-II program are three observables: (1) net-proton kurtosis, (2) υ_2 of φ meson and (3) dielectron production. The bullets below provide an overview of these observables:

Improved $\kappa\sigma^2$ for net-protons: The search for CP location requires quantitative measurements of the variation of of net-proton $\kappa\sigma^2$ with beam energy. The current measurements have large statistical uncertainty at all collision energies from $\sqrt{s_{NN}}$ = 7.7 to 27 GeV. These errors preclude any conclusion of a non-monotonic or monotonic variation of the observable with beam energy. We will need to achieve a statistical error of less than 10% on $\kappa\sigma^2$ for each beam energy in order to determine if the suggestive features of the net-proton higher moments shown in Figure 24 genuinely establish a non-monotonic behavior which is consistent with a CP. The estimated statistical errors, for the BES-II energy region 7.7 < $\sqrt{s_{NN}}$ < 19.6 GeV, for net-proton are shown in Figure 24 by the green shaded band assuming the required number of events listed in Table 4. The requested high statistics will allow us to pursue the net-proton distribution studies at higher orders (higher than the 4th) where one expects increased sensitivity to the criticality. In addition, we will also study the higher moments of the net-kaons with better accuracy.

Improvements in υ_2 of φ mesons and testing of NCQ scaling: This measurement will allow us to quantitatively address the suspected decrease, followed by an absence, of partonic collectivity below $\sqrt{s_{NN}}$ = 19.6 GeV. It is necessary to make measurements up to p_T = 3 GeV/*c* with a statistical error of less than 10% on υ_2. From this resolution requirement we can estimate the statistics necessary (see Table 4) for BES-II to reach transverse momenta beyond 2.5 GeV/*c* even at the lowest energies. This will allow us to test in NCQ scaling detail for many particle species, including multi- strange particles.

The projection of the statistical errors for the φ meson υ_2 for BES-II are shown by the shaded bands in both plots in Figure 28. As shown in Table 4, 100M and 200M useful minimum-bias events are required from the Au+Au collisions at 7.7 and 11.5 GeV, respectively. These measurements will answer decisively the question how much φ meson flow there is compared to that of light quark hadrons. Lack of the collectivity of the φ meson will provide clear

evidence of the hadronic interaction dominated medium in the low energy heavy ion collisions.

Improvements in the low-mass dilepton measurements: The event size of the data sets that were collected during BES-I for energies below 19.6 GeV have been too small to allow for meaningful measurements in the low-mass range of the dielectron spectrum, let alone in the intermediate mass range. The proposal for measurements in the context of BES-II would therefore not be as much as an improvement, but rather a first measurement of the dielectron invariant mass spectrum in this particular collision energy range. In Figure 36, the measured statistical (blue error bars) and systematic (blue boxes) uncertainties are shown for $\sqrt{s_{NN}}$ = 19.6 GeV. The proposed dielectron event statistics, summarized in Table 4, will allow the BES-II measurements to have statistical uncertainties (black error bars) that are comparable to those in the previously published 200 GeV papers [98, 99]. The systematic uncertainties will be improved by the iTPC upgrade (red boxes). The upgrade will also have an appreciable impact on the statistical uncertainties thanks to an increased acceptance at low p_T. The combined improvement of the systematic and statistical uncertainties will allow the BES-II data to better constraint different models that within BES-I uncertainties could otherwise not be distinguished.

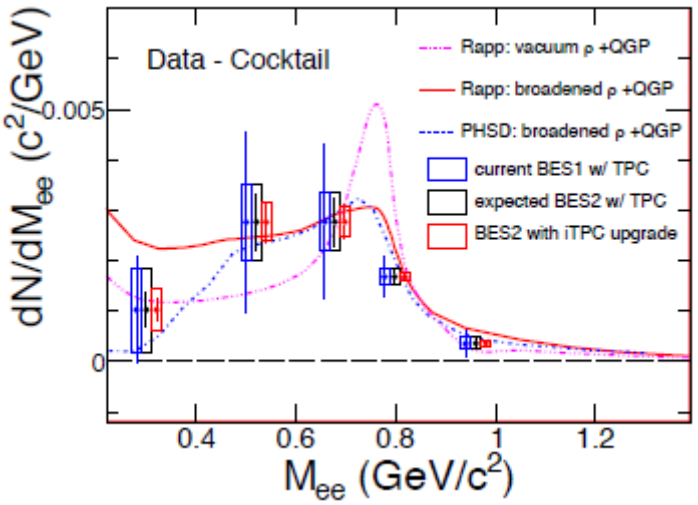

Figure 36: Dielectron invariant mass distribution for Au+Au at $\sqrt{s_{NN}}$ = 19.6 GeV.

The improvement needed in the intermediate mass range is estimated based on the statistical uncertainties of the dielectron mass slope from the same BES-I data set at $\sqrt{s_{NN}}$ = 19.6 GeV. A factor of 10 more (minimum-bias) events would bring that uncertainty to about 10%. This is comparable to the requested improvement in statistical uncertainty for the low-mass range measurements. During BES-II STAR's muon detection capabilities, thanks to the 2014 MTD up grade [100], will allow for independent measurements through e–μ correlations of the charm contribution to the dilepton continuum. In addition, with its trigger capabilities, the MTD will allow to efficiently select on the dimuon channel, which suffers significantly less from the large backgrounds that complicate dielectron measurements.

3.4 The FXT Program

3.4.1 Motivation for the FXT Program

In the normal collider mode, the lowest collision energy available at RHIC is 7.7 GeV. The fixed-target (FXT) program at STAR, with the iTPC and eTOF upgrades, will enable the energy scan to be extended to also cover the range from 3.0 to 7.7 GeV. It is important to measure key observables at energies lower than 7.7 GeV for several reasons:

- There are theoretical calculations suggesting that the mixed phase is entered at energies well below 7.7 GeV [101].
- NA49 has reported that the onset of deconfinement occurs at 7.7 GeV [102].
- Some of the QGP signatures (local parity violation [80] and narrowing of balance functions [103]) show signs of disappearing at 7.7 GeV. We need to extend the energy range so that we can confirm that these signatures have indeed turned off.
- The BES-I critical point search has shown intriguing results for the net proton fluctuations (see Figure 24). Predictions are that these fluctuations rise and fall in the region of the critical point. The rise (see at 7.7 GeV in Figure 24) should return to the baseline of unity at lower energies. This return to unity is not seen on the recent HADES results at 2.4 GeV and needs to be checked with lower energy data at RHIC.

The BES-I program was first proposed in the Run 7 STAR BUR; at that time energies of 4.6 and 6.3 GeV were proposed. In the Run 9 STAR BUR, 100k events were requested at 5.0 GeV. The collider tried circulating beams at 5.5 (Run 9) and 5.0 GeV (Run 10), but because the luminosity is proportional to γ^3 (the relativistic γ of the individual ion beams), operating below 7.7 GeV proved to be impractical. The FXT program provides a practical way of acquiring data below 7.7 GeV and was included conceptually in the 2014 BES-II proposal.

In order to determine the best conduct of operation for a FXT program at RHIC, a gold target was installed inside the beam pipe at STAR in Run 14. The target was 1 cm in height; 6 cm in width, and 1 mm thick. The target was positioned 2 cm below the beam axis and 2.1 meters to the West of the center of the detector (see Figure 37).
The iTPC and eTOF upgrades improve the acceptance of STAR for the FXT.

- The low-p_T threshold values are defined by energy loss in the backplane of the TPC.
- The η limit of the barrel TOF system is 1.47. The eTOF system covers η = 1.52 to 2.24.
- The track length in the STAR TPC for particles with η > 0.88 is longer in fixed-target events. Therefore, the *dE/dx* resolution for these tracks is better than for tracks with similar η values in collider events.
- The flight path for particles with η > 0.96 is longer in fixed-target events. Therefore, the TOF PID limits for these tracks extend to higher momentum than for tracks with similar η in collider events.

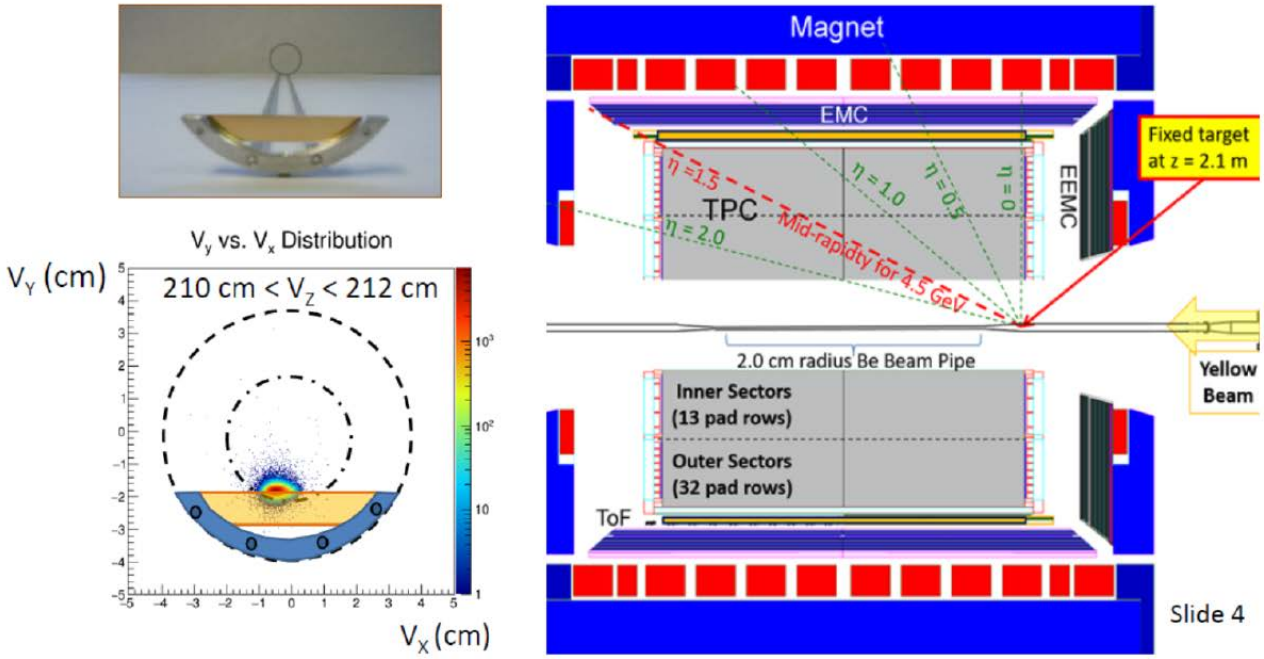

Figure 37: The top-left panel shows an image of the internal gold target. The lower-left panel shows the distribution of vertices with respect to the target. The right panel shows a side view of the STAR detector and the *z* location of the target.

The acceptance and PID ranges for fixed-target events are shown in Figure 38.

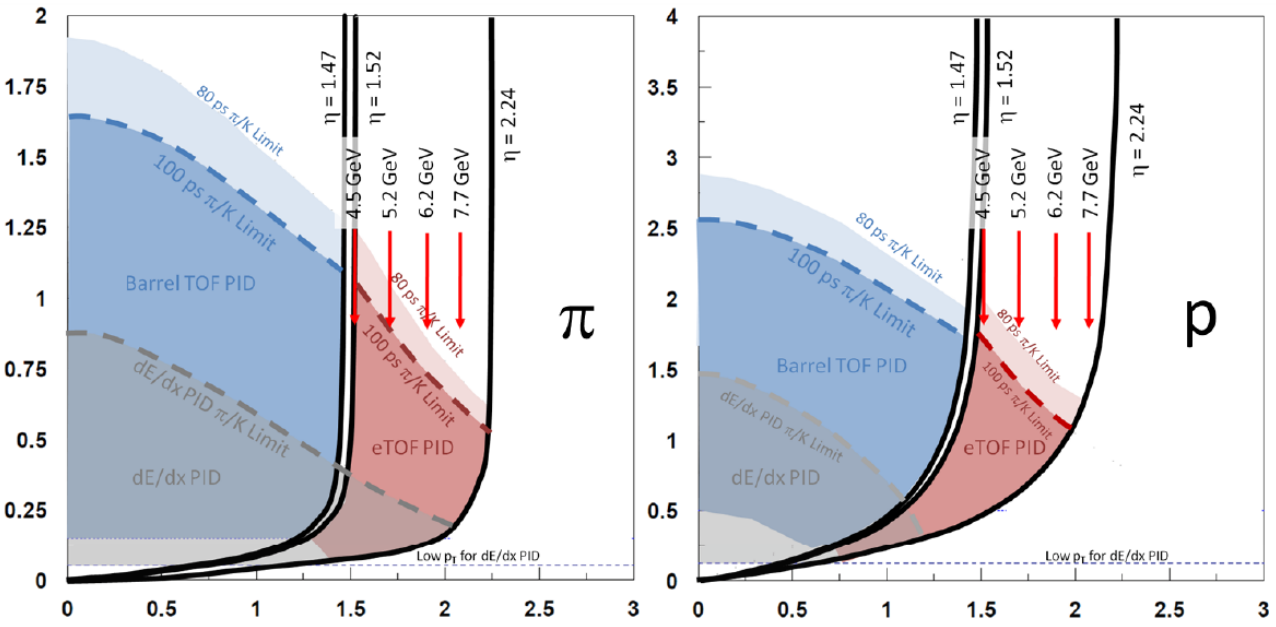

Figure 38: Acceptance maps in p_T vs. y space for the STAR detector in FXT mode. The regions in pink require the iTPC and eTOF upgrades.

From the point of view of conduct of operations, it was concluded that dedicated runs in which the elevation of the circulating beam is lowered to graze the top edge of the target can safely deliver a sufficient luminosity to fill the DAQ bandwidth of STAR. For FXT events, STAR can take data at 2 kHz; therefore STAR can accumulate 50 million events per day (also data taking 60% of the time).

3.4.2 FXT Physics Program

Exploring the phase diagram of QCD matter requires that at each collision energy there is sufficient yield (both $y_{CM} = 0$ and full acceptance) of each species to determine the chemical equilibrium T and μ_B values. The coverage maps shown in Figure 38, demonstrate that we have acceptance for π, and p from $y_{CM} = 0$ to y_{target} for all fixed-target energies except 7.7 GeV, where even with eTOF PID, the p acceptances do not reach $y_{CM} = 0$ (the K acceptances fall between those of the π and p). The efficiency for hyperon reconstruction is a convolution of the single particle acceptances. This will make possible y-dependent measurements of K^0_S, Λ, and Ξ^-. Currently, there is only a single Ξ^- measurement for collision energies below 7.7 GeV [104]. The STAR fixed-target program will map out the turn on of Ξ production with collision energy. Measurements of Ω, $\bar{\Lambda}$, and $\bar{\Xi}^+$ have not been made at these energies previously. Studying the onset of the production of these species could be possible with the fixed-target program using the eTOF.

NA49 has argued that the onset of deconfinement is achieved at 7.7 GeV [102]. This result is based on a set of inclusive observables: there is a kink in the rate of increase of the pion production with collision energy, there is a step in the slope parameter of the kaon spectra, and there is a peak (horn) in the K^+/π^+ ratio. We will study all of these inclusive observables. In addition, the fixed-target program will allow us to track other QGP signature observables, studied in BES-I, spanning a collision energy range from 3.0 to 19.6 GeV (μ_B from 720 to 205 MeV). Observables that will be studied in the fixed-target program:

- Number-of-constituent-quark scaling of elliptic flow is a key QGP signature [105]. The results from BES-I show the N_{CQ} scaling is exhibited independently for particles and anti-particles [24]. At fixed-target energies, the N_{CQ} scaling for particles is expected to break. The elliptic flow is a mid-rapidity observable, and PID is necessary in order to observe the N_{CQ} scaling.

- One form of balance function is a rapidity correlator. This correlator is sensitive to QGP formation [106]. The BES-I data show the balance function narrowing signal decreases with decreasing beam energy. This signal is almost, but not quite, gone at 7.7 GeV [103]. Lower energy measurements are needed to demonstrate that this signature disappears. A key to the sensitivity of this measurement is the width of the total rapidity window.

- Strangeness enhancement is seen as an important QGP signature. The energy range covered by the fixed-target program sees the opening of several strange particle production channels. The strange particle production is maximum at mid-rapidity, and cleanly identifying weakly decaying strange hadrons requires clean PID for the daughters.

Assuming that there is a first-order phase transition, the concept of a single “onset of deconfinement” is an oversimplification. Depending on the universality class of the phase transition, there may be a spinodal decomposition which would imply a mixed-phase region with a negative compressibility. Rather than a single “onset”, there may actually be several interesting onsets: the lowest energy which causes some fraction of the system to enter the

mixed phase region, the energy at which the system spends the maximum amount of time in the instability regime, and the energy at which the system passes into the pure QGP phase. In order to understand the nature of the phase transition, we propose to study several observables which are expected to have sensitivity to the compressibility. These observables include:

- The directed flow of protons, which offers sensitivity to the early compressibility. Most of these particles are transported participants recoiling off the interaction region [76, 107, 12, 13, 14, 11]. We will study the evolution of the mid-rapidity "wiggle" which is particularly sensitive to compressibility and is known to be absent [108] at the lower end of the proposed fixed-target beam energy range.

- The tilt angle of the pion source, measured through femtoscopy [109, 110, 111].

- The volume of the pion source, measured through femtoscopy [112].

- The width of the pion rapidity density distribution, which has been argued to be sensitive to the speed of sound in nuclear matter [113]. This study relies on the ability to characterize the shape of the rapidity density distribution. Measurements with sufficient rapidity acceptance are required in order to understand the shape of the distribution.

- The elliptic flow of protons, which has been shown to change sign at a fixed-target beam energy of 6 AGeV ($\sqrt{s_{NN}}$ = 3.5 GeV) [114]. This sign change of v_2 is explained by the transit speed of the projectile nucleus through the target nucleus matching the expansion speed from compression (speed of sound).

- The Coulomb potential of the pion source provides an independent means of assessing the source volume, being affected by the expansion velocity of the system [115].

- The life-time of the emitting source, measured through low-mass dileptons [116].

The observation of enhanced fluctuations would be the clearest evidence that the reaction trajectory of the cooling system had passed near the possible critical end point on the QGP/hadronic gas phase boundary. Recent analyses of the higher moments of the net-proton distributions have suggested the possibility of enhanced fluctuations at 7.7 GeV [82]. These results require higher statistics to improve the significance. It has also been shown that the significance of the $\kappa\sigma^2$ signal scales as N_p^3.

An important test to determine if the enhanced fluctuations are related to critical behavior would be to see the fluctuation signals return to their baseline levels at energies below 7.7 GeV. The energies of the fixed-target program will provide these important control studies, allowing critical behavior searches to be extended to higher μ_B. Clean PID is essential for this analysis and its sensitivity has been shown to depend strongly on the efficiency and acceptance. At 4.5 GeV, test run data indicate that we accept 20% of all protons using the current configuration of the TPC. This would drop to 5% for the 7.7 GeV fixed-target energy. The key mid-rapidity coverage of the eTOF raises these acceptance numbers to 50% and 20% respectively (increasing the significance of the results by a factor of 15 to 65). Although there are some fluctuation analyses performed by the NA49 collaboration [117], the more sensitive higher moments studies have been done only by STAR [82, 118], PHENIX [119], and are being studied by HADES at 2.42 GeV. There were no critical fluctuation studies performed at

the AGS so the fixed target program will provide the first data in this energy regime.

Dilepton experiments have been an important part of the physics program at almost all heavy-ion facilities, with the notable exception of the AGS. At the lowest energies, HADES measured e^+e^- productions in Au+Au collisions at $\sqrt{s_{NN}}$ = 2.42 GeV. In the SPS heavy-ion program, dilepton data were taken by experiments Helios-3, NA38/50, CERES, and NA60. And at RHIC, both PHENIX and STAR have dilepton capabilities. The eTOF detector will provide electron ID at mid-rapidity for all energies of the fixed-target program. This provides the first opportunity to study the evolution of the low-mass dilepton excess in this collision energy region in which the low-mass yield might be also sensitive to the emitting source temperature in addition to being sensitive to the total baryon density. These dependencies will help us to understand the mechanism of in-medium ρ broadening which is the fundamental probe of chiral symmetry restoration in hot, dense QCD matter.

The first species of hypernuclei, ${}^{3}_{\Lambda}\mathrm{H}$ and ${}^{4}_{\Lambda}\mathrm{H}$, were discovered in the 1950s [120]. Several isotopes of hyper-helium and hyper-lithium have been found in kaon beam *s*-transfer reactions. In heavy-ion collisions, light nuclei are formed through coalescence of nucleons. As the energy is raised, nucleons can coalesce with hyperons to form light hypernuclei. At even higher energies, anti-nucleons can coalesce to form light anti-nuclei. This coalescence mechanism has allowed STAR to make the discoveries of anti-hyper-tritium ($\overline{{}^{3}_{\Lambda}\mathrm{H}}$) [121] and anti-alpha ($\overline{{}^{4}_{\Lambda}\mathrm{H}}$) [122].

The energy regime covered by the fixed-target program (3.0 to 7.7 GeV) should be optimal for the formation of matter (as opposed to anti-matter) hypernuclei. At energies below 3.0 GeV, few hyperons are produced, whereas at energies above 8 GeV, the increased production of anti-baryons stifles formation of composites of matter particles. Meaningful samples of ${}^{3}_{\Lambda}\mathrm{H}$ and ${}^{4}_{\Lambda}\mathrm{H}$ will be observed at all the fixed-target energies. Simulations have been made assuming eTOF coverage and PID. The statistics are expected to be comparable to STAR data samples from 200 GeV collider data; this will allow a precise measurement of the light hypernuclei lifetimes and a mapping of the ${}^{3}_{\Lambda}\mathrm{H}/({}^{3}\mathrm{He}\times(\Lambda/p))$, and ${}^{4}_{\Lambda}\mathrm{H}/({}^{4}\mathrm{He}\times(\Lambda/p))$ ratios as a function of $\sqrt{s_{NN}}$. Searches for multi-strange hyper-nuclei (${}^{5}_{\Lambda\Lambda}\mathrm{H}$ and ${}^{6}_{\Lambda\Lambda}\mathrm{He}$) make appealing physics goals. However, further simulations arerequired to determine if these measurements will be feasible with the expected integrated luminosity.

3.4.3 FXT Beam Request

The FXT program at STAR will employ energies that have already been developed for the BES-I program. Details of the sequence of energies is listed in the tables in theExecutive Summary. Table 5 shows $\sqrt{s_{NN}}$ set-up for the collider and the center of mass energy for FXT. Also listed is the kinetic energy of the beam as some other facilties use this describe the energy system. The center of mass rapidity is listed as this gives insight to the acceptance of STAR for a given energy, and the expected chemical potential demonstrates the region of the QCD phase diagram to be studied.

Table 5: Collider set-up and fixed-target center-of-mass energies ($\sqrt{s_{NN}}$), projectile kinetic energies (AGeV), center-of-mass rapidity offset (y_{CM}), baryon chemical potentials (μ_B) for the proposed fixed-target program.

Collider $\sqrt{s_{NN}}$	FXT $\sqrt{s_{NN}}$	Kinetic (AGeV)	Rapidity y_{CM}	μ_B (MeV)
62.4	7.7	30.3	2.10	420
39	6.2	18.6	1.87	487
27	5.2	12.6	1.68	541
19.6	4.5	8.9	1.52	589
14.5	3.9	6.3	1.37	633
11.5	3.5	4.8	1.25	666
9.1	3.2	3.6	1.13	699
7.7	3.0	2.9	1.05	721

4 Computing at STAR

4.1 STAR Workflow and Computing Resources

The STAR computing resources available for data processing currently consists primarily of the resources available at the RHIC Computing Facility (RACF) where at most 14,000 CPU slots are allocated to the data production campaign and the handling of data calibration tasks. The rest of the RACF slots are reserved for user analysis jobs, with the overflow directed to opportunistically utilize unused resources from other experiments. While the number of slots used by the data production and calibration workflows is ~14,000 on average across the year, this number fluctuates lower during RHIC run time (when additional resources are taken for near real-time incremental calibrations) and increases just after major conferences in the field (when user's jobs slightly deplete).

In the early years of RHIC STAR had the resources to produce a given run's data 2.2–2.4 times within a year after the data was taken. Severe resource constraints in past years have forced the STAR Software and Computing team (S&C) to first reduce this number to a conservative 1.2–1.5 passes. Additionally, because the computational resources have not grown for several years, S&C no longer constrains the 1.5 passes to fit with a year's schedule. Instead, planning is made and expressed in terms of delayed production and scheduled physics priorities. Processing time needed for calibration varies from 1.5 to 3 months depending on whether the collision system is well known and all calibrations follow expectations, or if the studied system is novel (i.e. isobars in Run 18) and/or presents a unique new challenge such as unusually high luminosity, additional distortions or inclusion of a new detector sub-system. Typically, the scheduling of the production of quality high priority physics datasets may occur as soon as 2 months after a given run ends. To reach this goal, incremental calibrations are performed during the run (both online and offine), allowing for rapid turn-around at run's end. At that time sub-system software leaders and designated calibration experts work on bootstrapping and correlating all calibration pieces, including particle identification.

To increase resource availability, the S&C team has attempted to make use of the unused cycles on the PHENIX farm. This effort was suggested by the 2016 PAC and initially believed to have the potential to deliver a boost of +12.5% in processing time over a period of 6 months. Unfortunately STAR jobs submitted to PHENIX resources are only allowed to run for a fraction of the time needed to complete the full reconstruction of all events in a single DAQ file (jobs running long are killed and must be re-submitted). As a result, each job must be split into N sub-tasks that can be completed within the allowed time. This then raised the need to ensure all N sub-tasks are completed before merging back into a set of single output files. Setting aside the bookkeeping complication this implies, it is worth noting that the RACF production system (a.k.a. CRS) did not allow the restoration of the same DAQ files multiple times on multiple nodes while simultaneously minimizing tape access. This issue was reported and fixed in early 2017 and we were then in a position to test the feasibility of this new paradigm. Ultimately, for reasons detailed below, we feel this mechanism is not a productive path forward for STAR. First, such workflow does not allow our jobs to be transient. The transient property of our jobs (whether running on the Grid or on STAR's own resources) is the fact that for all jobs, data is transferred to the compute element (asynchronously to the use of the CPU cycle) and the output produced locally then moved as soon as possible to tape storage (HPSS). The data appears only temporarily onto central disk storage (for purposes of data sanity validation and cataloging) and the storage freed as soon as this automated process has completed. Such workflow adaptation has allowed us to survive the increase in production demands over the past years under a flat-storage budget scenario. But in the case of using the PHEHIX resources, storage needs to be available to store the output of N sub-tasks before they are merged into single files and moved to tape. For this to happen, additional storage is required and we estimate we need to have at least a day worth of central storage (~15 TB) to support this mechanism. Second, the long pause of our incomplete jobs (i.e. waiting for any of the N sub-tasks from a single job to finish) would, upon resuming, restore again the raw data causing an increase access to tape resources (hence risking increase of wear-and-tear) – this has shown to be detrimental to media lifetime. Finally, due to the very unpredictable nature of the availability of those resources (if PHENIX starts a production campaign, we may be out of the queue for a long time), this does not allow for providing our Physics Working Groups (PWG) with accurate estimates of when data productions would be delivered. To add to those bookkeeping, technical and organizational issues, at the time of writing this report the unused PHENIX resources have dropped to an 8% average over the past year. Meanwhile STAR's user analysis jobs, more adapted to short time slots, continue to harvest up to 17.25% of unused PHENIX's resources.

More predictable resources provide a fast path for scientific discovery while minimizing human investment. The S&C team has therefore continued to look and focus on additional resources outside the RACF. Those include the farm available at our Dubna institutions (at most 1,000 slots or +7% increase of predictable CPU cycles) and the less-standard use of High performance Computing (HPC) resources at the NERSC/Cori Supercomputing leadership facility. In 2016, STAR demonstrated the first high efficiency use of HPC resources for real-data production in the Nuclear and Particle Physics communities. This work was presented at the CHEP 2016 conference and showed an end-to-end workflow efficiency nearing 95% and the STAR collaboration was subsequently provided with an allocation of 25 Million hours.

Those remote resources are primarily used to provide a boost to the data production workflows (lower priority datasets are moved to Dubna with predictable estimated time to

delivery) or used to provide additional production passes realigning with a community standard number of production passes far greater than 1. While our workflow efficiencies are very high, for planning purposes, we will use a 93% compounded efficiency where the compounded efficiency is defined as the product of the resource utilization efficiency (our ability to saturate the available slots) times the application's run-time efficiency.

4.2 Datasets overview and Prioritization process

The STAR data production plan is an evolving prioritization process based on input from the PWG conveners, the readiness of data calibrations and the software development time invested to deliver high precision physics. Analysis of past challenges revealed that the lack of live storage was proving to be a show-stopper to either stage the MuDsts and/or store the PWG's private analysis tree necessary to pursue their analysis and publications in a timely manner. Therefore, STAR had vested interests in developing newer and more compact analysis data format and in 2016, the Data Summary file format known as a "MuDST" (micro-DST) was complemented by an emerging format known as "picoDST". The picoDST related code workflows were since integrated in the STAR framework after a successful software peer-review process verifying code compliance. The PWG were actively polled for readiness and adaptation of ongoing analysis to the new file format and the picoDST was extended for a wider acceptance across all physics topics.

Table 6: Production summary for the Run 14, 15 and 16 datasets. The first row within a block shows the summary for a given year, while the subsequent rows provide information broken down by species. Lighter species being processed faster, the %tage completion is given in both number of events and relative time for the year summary. Text in *italics* indicates productions considered completed (note %tages less then 100 reflect the fact that some jobs may have not been recorded).

Year	Species	Total #events (M)	%tage events completed	Estimate time to delivery (months)	%tage time to completion
16	[summary]	**9126.46**	**49.44**	**3.74**	**60.45**
	Au+Au 200GeV	6543.26	63.25	3.22	
	d+Au 200GeV	1181.10	31.58	0.44	
	d+Au 62GeV	357.91	0.00	0.08	
	d+Au 39GeV	642.12	0.00	0.08	
	d+Au 20GeV	402.08	0.00	< 0.08	
15	[summary]	**10997.37**	**84.31**	**0.75**	**86.89**
	p+p 200GeV	6329.66	93.70	*0.19*	
	p+Au 200GeV	3647.70	78.76	0.33	
	p+Al 200GeV	1015.11	45.61	0.24	
	fixed Target	4.76	100.00	0.00	
14	[summary]	**6718.09**	**84.66**	**0.39**	**90.85**
	Au+Au 200GeV	5045.59	96.79	*0.22*	
	He3+Au 200GeV	1260.30	31.29	0.18	
	Au+Au 14.6GeV	412.20	99.38	*0.00*	

All 2016 datasets produced both micro-DSTs and picoDSTs and STAR is in the process of converting a few selected past datasets to the new more compact format. With 10 CPU cores,

we estimated we needed 4 days to convert 6 TB worth of MuDST to picoDST. The full conversion of all datasets produced prior to the 2016 data production campaign would therefore require allocation of resources. As all conversion tasks look alike (and each job is short), this may be a place where STAR can effectively utilize unused PHENIX cycles, although this remains untested at this time.

Table 6 shows the status of data production during the past year, including % completed in number of events and total time estimated to wrap up production for a given run. Since lighter systems require less time to process for an equivalent number of events, it is to be noted that we are nearly complete for Run 14, 86.9% complete for the Run 15 datasets and ~4 months away from completing all Run 16 datasets production.

4.3 Production computing resource estimates for the purpose of the BUR

Table 7 provides estimates for DAQ, data summary ("MuDST" and “picoDST”) dataset sizes for the past, not yet fully produced, RHIC runs as well as the proposed colliding species in this BUR along with the estimated time needed to process those datasets considering the currently available resources. As discussed earlier, we base our plan on 1.5 production passes, a need for time for calibration processing, and an overall workflow effciency of 93%.

Table 7: Required resource summary table broken down by year and collision systems. The columns indicating “total space required” are the cumulative space necessary to keep all current datasets available for analysis (in the prefixed specific format) as well as future year’s dataset in distributed storage. The first row indicates the current space usage and in italic, the usage if all datasets currently available to data analyzers (in MuDST format) would be converted to the picoDST format. Production time estimates are given in months time assuming the 2017 RACF farm size.

Year	Species	RAW space [PB]	MuDST space [PB]	picoDST [PB]	MuDST total space [PB]	picoDST total space [PB]	Total reco time, 1.5 passes [m]	Required (+calib time) [m]
					8.5	***1.31***		
16	200 GeV Au+Au	6.96	4.88	0.70	**9.28**	**2.09**	14.04	**15.20**
	200 GeV d+Au	0.43	0.53	0.08			1.04	
	Low energy d+Au	0.14	0.06	0.01			0.12	
17	500 GeV p+p	4.85	2.65	0.41	**12.53**	**2.59**	11.4	**15.34**
	Low energy Au+Au (27 GeV or 1/2 time 62 GeV)	1.2	0.6	0.09			1.45	
18	27 GeV Au+Au	0.32	0.22	0.03	**12.76**	**2.82**	0.42	**6.48**
	200 GeV Ru+Ru	0.88	0.65	0.10			1.53	
	200 GeV Zr+Zr	0.88	0.65	0.10			1.53	
19/20	Various Au+Au BES-II	0.35	0.25	0.04	**13.01**	**2.86**	1.45	**2.95**

The MuDST to picoDST size ratio varies from 7 (measured for all Run 16 data productions) to 6.5 (planned addition of information that would cover for most Physics Working Group’s need).

The Run 18 plan as well as a Run 19 or Run 19+20 combined plan are represented for an overview of the current BUR. For the purpose of resource planning, those two scenarios (19 or 19+20 combined) provide little differences to the overall conclusion so they are grouped together.

A few conclusions emerge. First and foremost, considering the remaining time outlines in Table 6 for finishing all data production, we see that in ~5 months' time all past data would be produced at least once (providing priorities are given to data production). With an end of the Run 17 currently planned by summer and considering a needed 2.5 months calibration time for those samples, STAR is unlikely to suffer major delays in delivering datasets from Run 17 flagged as high priority. As indicated earlier, this projection may change depending on upcoming conferences and the usage of the farm for user analysis (but the fluctuation is at most a 12% effect). Year 17 will offer the same challenge as year 16 – an extended allocation on facilities such as NERSC/Cori, or a boost of resources from one of our remote Grid facilities if available, would once again absorb the excess resources needed to fit the production campaign within a year's time. But the out years are light on resource demands and do not seem to raise significant computing resource challenges. For the BES-II datasets especially, and providing the organization of our calibration is focused during the run, STAR could even consider a near real-time processing of the data. Particular attention is needed on columns 6&7 of Table 7 however. Those columns represent the total cumulated storage needed to keep all previously stored datasets and future datasets under the MuDST and picoDST assumption respectively. They illustrate the storage challenge the collaboration has been facing. STAR's distributed storage capacity of 8.6 PBytes is currently occupied at its near maximum capacity of 8.5 PBytes. To make the datasets from 2016 and future years available to STAR analyzers, it is clear that the only path is a full push forward toward the use of the picoDST format. Since the picoDST columns shows we would need at maximum ~3 PB of storage, it is conceivable that only some of the past datasets (and not all) would be converted to the new format. The discussion of which past datasets should be converted has started within the PWG.

A final note that for data collection and run plans beyond the scope of this BUR, the storage limitations will remain a constraint limiting both the data production workflow we could envision and our ability to keep most physics datasets available for physics analysis. Large datasets, without complementary CPU resources, would further see a delay in the delivery of physics samples.

4.4 STAR–JINR GRID Computing

Introduction

STAR's first physics run was in year 2000. The detector takes one data run, lasting about six months, every year-currently we are on our 18^{th} physics run. This poses a huge data challenge as the dataset from one run has to be calibrated and reconstructed before the next dataset is captured. STAR's local computing facility (the RHIC Computing Facility or RCF) provides ~15,000 computing slots for this data processing. This allows between 1.2 to 1.4 passes of reconstruction whereas the typical high energy physics experiment takes in excess of five passes. In order to speed up the rate of scientific discoveries, STAR started

utilizing grid resources in 2001 for simulation requests, where small efficiency losses are tolerable, and over-submission can cover for losses. Today the bulk of computing requests are reconstruction of detector data which requires higher efficiency as there is only a precious finite amount of input. Detector upgrades have provided exponential increases in detector data while the computing resources remain mostly flat. To date STAR has collected about 50 Petabytes of data. So there is a desire and need to supplement local computing resources with grid computing resources especially for detector data reconstruction.

STAR's current and former production sites

STAR has received support over the years from a shifting array of cloud and grid production sites. Currently STAR is using the JINR (Joint Institute for Nuclear Research) tier-2 site with an agreement to opportunistically utilize 500 slots and later increase to 1,000 slots if good utilization is demonstrated, along with STAR's own Online cluster which is a mix of Xeon Phi systems and conventional systems under STAR's grid production resource pool. As all sites are heterogeneous the reconstruction software is pre-compiled to insure that there will be a compatible payload for target sites.

Grid sites utilized by STAR but not using the grid production system software include NERSC's (National Energy Research Scientific Computing Center) PDSF cluster which is used for complex simulation along with user analysis and NERSC's Cori which is an HPC cluster used for detector data reconstruction. The envisioned payload for such a cluster is one which requires a massive number of processes with low latency inter-communication between all of the threads. This has traditionally not been a requirement of STAR data reconstruction, which can run on inexpensive commodity hardware which can even be geographically separated at different sites.

Another typical attribute of current HPC clusters is a high ratio of CPU cores to memory. In order to efficiently utilize such HPC clusters, event level parallelization is required because the "pleasantly parallel" computing model requires too much memory per process (or core) and the implied input size is greatly reduced. With event level parallelization the base memory footprint of the payload can be shared amongst many event level reconstruction threads. Event level parallelization requires one input file to be split into event ranges, each of which is assigned to one of the reconstruction threads. Each thread produces its own output file which must be merged back into one contiguous file. This is done on the host site and requires a common buffer space. With this workflow, host sites without a common buffer space cannot utilize event level workload splitting, instead whole files are processed in a "pleasantly parallel" model. However care must be taken in this case to insure all events can be processed within the host site's queue time limits otherwise, the process will be evicted before it has time to finish its reconstruction and copy back its output. Another benefit of a local host site providing common buffer space is that the output payload can be copied to the buffer and the processes can terminate allowing the output to be copied back outside of the job's runtime. We will discuss data transfer modes in more detail in the upcoming section.

Data transfer modes

When running detector reconstruction on a remote site it is necessary to transfer the raw

detector files to the site which will be used as the reconstruction job's input and to transfer back the reconstructed output files. Simulation tasks are easier because there are no input event files to transfer to the remote site (only trivially small configuration files need to be sent), but simulation is a relatively small percentage of STAR's computing workload. Transfer modes for workflows with both input and output can be divided into two groups, those using a shared buffer space on the host site and those without such a space. It is relatively common to have sites share computing slots but provide no local disk space as storage is a more valuable resource requiring a file retention time far in excess of an individual job's own runtime to be viable.

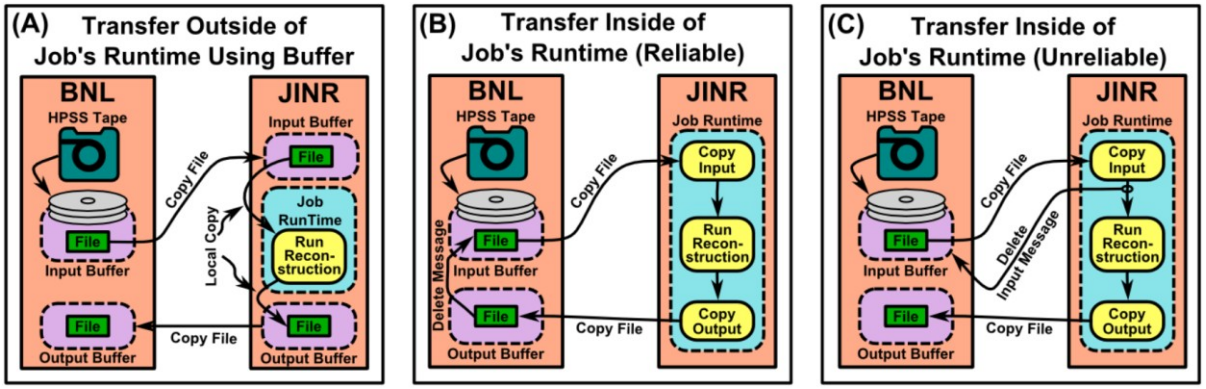

Figure 39: Transfer modes from submitter (BNL) to host site (JINR)

In all modes the input file is restored from a tape located in the drive silo (HPSS) to a local buffer at BNL. Figure 39 shows three transfer modes labeled (A), (B), and (C). Mode (A) depicts a transfer utilizing a shared buffer space on the remote site (JINR). Then the input (raw event file) is copied to a local buffer on the remote site. As it is a shared space, once the job starts up it can do a local copy into the job's local temporary directory where the job has low latency access to the input. As the job runs and processes the input it produces the output file which it also writes into the job's local temporary directory. Just before the job finishes it does a local copy to the local output buffer, which may be the same as the input buffer. The benefit of mode (A) is that site-to-site transfers occur outside of job runtime. Interruptions or slow transfer of the input and output files will not consume job runtime as wasted CPU cycles and will not accumulate towards queue runtime limits, potentially losing the output files when jobs are killed by the batch system. Network connectivity interruptions between the two sites can be very large without affecting recovery of the outputs, given a sufficiently large output buffer. The negative aspect of this mode is that more logic is needed to manage the remote site buffers, keep them clean and insure they do not overfill.

Modes (B) and (C) are variations on transfers without remote shared buffer space. As a consequence all transfers are transacted inside of job runtime. The STAR grid production system supports both modes (B) and (C). We have extracted statistics for a period of six months from the production system's database to determine the overhead of performing the transfers within job runtime between BNL and JINR. The average reconstruction time was 1,784.3 minutes and the average input file size was 2.05 GB with an average input file copy time of 12.9 minutes which constitutes 0.7% of the total runtime. The average output file size is 1.31 GB and the average output file copy time is 5.36 minutes constituting 0.3% of the job's total runtime. The average job spends

99.0% of its time in actual reconstruction. From these statistics it can be concluded that the

transfer overhead is negligible. An identical conclusion was reached looking at a large production STAR ran at KISTI (Korea Institute of Science and Technology) in 2015 [90].

In mode (B) the input file is restored from HPSS to a local buffer, and once the job starts it pulls in its input file directly to the job's local temp space. After reconstruction is completed the job copies (pushes) back its output file and log files from the worker node's temp space directly back to the submitting site's output buffer. Once the output files are verified to be intact and correct, the production system removes the input file from the submitting site's input buffer. If the output files are not intact or are missing, the input file in the local buffer remains, and a new job is submitted to attempt to process the input again. One disadvantage of this method is that the local buffer must be large enough to hold a copy of the input file for every running job. With input files of several GB each multiplied by the number of available slots the buffer may need to be very large indeed. If the input buffer is insufficient it will limit the number of job slots that can be filled.

Mode (C) overcomes the above problem of requiring large local input file buffers. Once the input file is restored and the job pulls it in, the job sends back a message indicating that the framework may remove the input files from the local site. As a side note this signal is always sent, but as it plays no role in the other modes it has not been drawn in the other illustrations. Once the input file is removed the space can be reused for the next job. In this way a small local input file buffer can support a large number of jobs. However if the job fails after sending back the "input copy completed" message then the input file must be restaged again from tape. For this reason this method has been christened "unreliable" just as the IP network protocol is unreliable. However, the method is used within the context of the production system, and the system always verifies completion, so even if the job fails multiple times due to transient problems (up to the configured retry limit), the job is likely to be ultimately successful, albeit with more overhead in the case of a re-submission. As the latency of file restoration from HPSS is very, large especially when the files requested are noncontiguous, this method is typically only used when the first pass efficiency is very high and the number of slots available exceeds the input buffer limit. First pass efficiency is defined as the percentage of jobs that successfully complete without any resubmission attempts. In all three models above (A, B, C), gsiftp is used as the transfer protocol as implemented by the globus-url-copy [91] program for both pulls and pushes of files. Plans are underway to deprecate the Globus software stack including the globus-url-copy program as the developers no longer wish to support it. Globus-url-copy performs the copy, user mapping, and authentication. The OSG [92] (Open Science Grid) has made a commitment to support the Globus software stack for at least three years. However this component will eventually have to be replaced with a substitute.

JINR lessons learned

As with any site added to the STAR grid production system, extensive testing and tuning is first done to insure the best possible efficiency, such as job first pass efficiency and bandwidth testing of the network connection in both directions. The initial configuration consisted of submission to a CREAM CE [93] from an HTCondor [94] client (HTCondor is distributed with a built-in CREAM submission plug-in). For authentication a grid proxy with VOMS [95] extension was used. It was initially believed this configuration could provide a robust method of submission between the OSG and WLCG environments. And it did work to

first order allowing the submission of jobs. However the first pass efficiency was poor. Most of the inefficiency was attributed to the VOMS extension. For non-technology (administrative) related reasons the lifetime of the proxy was limited to three days, and renewal of the proxy on the submission side did not always propagate. Automated password-less renewal of the proxy returned successfully however the internal VOMS proxy certificate chain was mangled and was unable to actually authenticate hence renewal had to be done by hand. With these and other problems it was decided to switch to a native HTCondorCE on the JINR (host site) side from the OSG distribution and use a long-lived grid proxy to authenticate. This achieved our goal of over 90% first pass efficiency. Some bugs still exist – most notable HTCondor will lose track of some jobs, reporting them as held in the local HTCondor queue when they are in fact still running. This was realized by the fact that the held jobs later returned output. This inconsistency in state tracking is observed in the presence of network transient outages between the CE and HTCondor client.

A resource constraint we had not encountered before was a tight limit on queued jobs (jobs waiting for a free slot to run). If jobs exceed the limit they go into the held state. To ensure this limit is not exceeded we simply adjusted a parameter in the HTCondor client to limit the number of jobs pushed over to the JINR host site at any one time. This way the local queue (submitting side) can hold as many jobs as required up to the resource limits of the queue and only push over the pre-configured quantity into the host sites local queue. Once the remote host site's batch system digests some of these jobs and the number of jobs in the remote queue drop, HTCondor will push over more jobs up to its limit again and repeat this feeding cycle as long as jobs exist.

STAR grid production system components and data flow

The STAR production system uses mostly existing software components maintained by STAR itself or the grid community, mainly OSG. Hence development time is minimized and the quality of these components is high as most of the debugging was carried out in advance and maintenance over time is assured. The STAR local components have an additional advantage in that the collaboration decides the end-of-life date of all components instead of external groups. Some of the STAR components include the STAR Unified Meta Scheduler (SUMS) [96], the STAR Data Carousel [97, 98] and STAR File Catalog.

SUMS, first deployed by STAR in 2002, provides a uniform interface for users submitting jobs both locally and via the grid across all STAR sites. It also allows sites to transparently switch between batch systems without disturbance to the user's job submission and expert shaping of resource requirements. SUMS takes a JDL (Job Description Language) request which describes a dataset, operation, and optional resource requirements such as memory, time (events or files per hour) and produces jobs based on a tailored configuration which it submits to a batch system or grid or cloud interface. This fits very well into the production system because different JDLs can be produced for the processing of different datasets. It is the component that transforms the actual request into jobs.

The STAR Data Carousel is a tool which restores datasets from HPSS to disk for reconstruction. It has a sophisticated feature, holding a queue of file restoration requests from multiple users re-orders the queue by the tape on which the requested files reside. This will minimize the mount-dismount cycles, as the time required for the robotic

arms to fetch and mount a tape is relatively large.

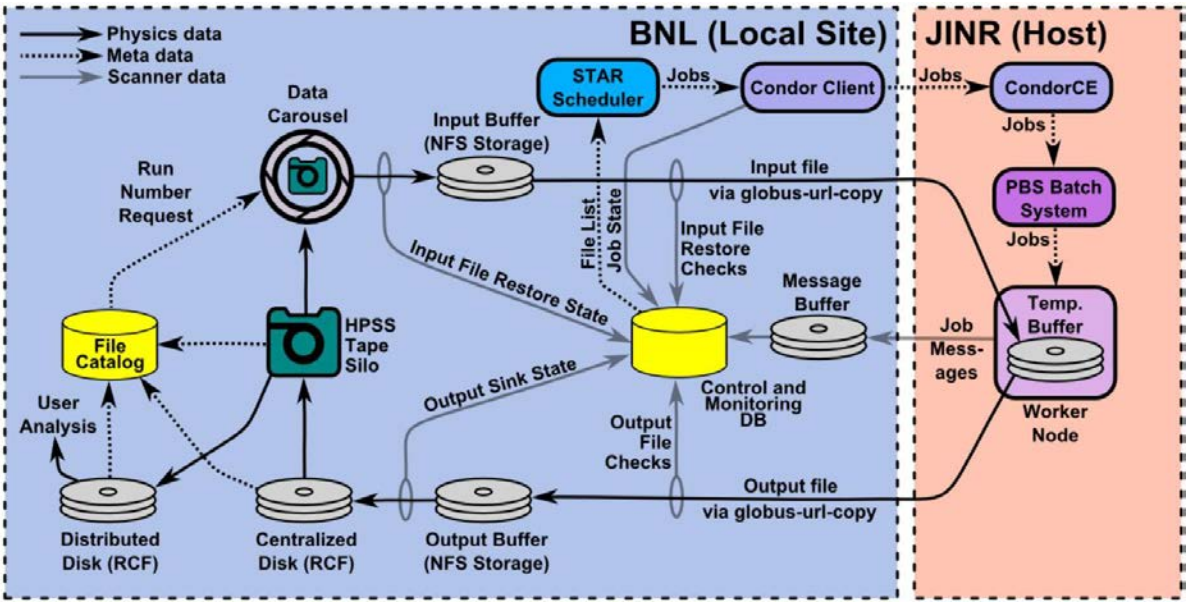

Figure 40: STAR Grid Production System Dataflow

The diagram in Figure 40 shows STAR's grid production system dataflow. Starting from the left, the input files are originally located on HPSS tapes with the list of files to be restored coming from the STAR File Catalog. The carousel will recover as many files as can possibly be fit into the grid production system's input file buffer on NFS disk at any one time. Typically this will only be a small fraction of the total dataset. SUMS picks up the list of files and submits one file per job to the HTCondor grid client which passes the jobs to the remote site's batch system where they eventually execute on the worker node and pull in their input files. While a job is running it passes back messages. Once a job is done it copies its output file back to the local site. The file is placed into the output buffer. Once the scanner passes over the file it is copied to both centralized disk, where it can be used for physics analysis, and to HPSS tape for backup. At multiple stages along the way the scanner is checking the throughput for validity, advancing the dataflow with its movement scripts, and retrying steps where possible and necessary.

STAR's grid production system's finite state system

Using JINR's resources, STAR has a high (93.2%) first-pass efficiency. However the requirement is that the n^{th}-pass efficiency is 100% of all files that can be reconstructed. A finite state system model is used to track the progress of each file to be reconstructed. This includes loops to retry actions such as copying files in or out and, if needed resubmitting the job which would count as a first-pass efficiency failure. Retries are limited to a finite number of attempts.

Figure 41 illustrates the finite state automaton's states and transition conditions which are kept track of in the production system's control and monitoring database illustrated in Figure 40.

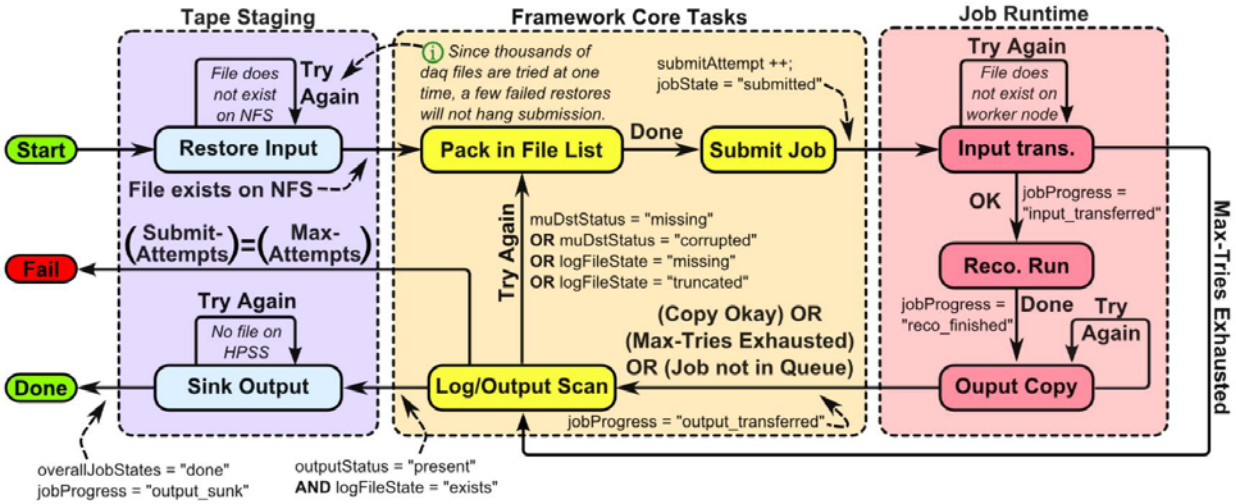

Figure 41: Finite state machine diagram for grid production system

Resubmission of failed jobs

Key features of any software claiming to call itself a production system versus by-hand-submission is the ability to feed, monitor, and resubmit failed jobs. The software must accurately determine if a job has finished and was successful. Our system does this by polling the batch system every hour to check if the job is still in the queue. Once the job is out of the queue, the system checks the expected location of output files for their existence, size, and the log file for known error patterns. In an older version the software checked checksums taken on the worker node verses the checksum of the same file on the output buffer, however this was later replaced by a simpler and faster size check, which does not require reading back all of the output files. It is critical to check returned output quickly so it can be flagged for sinking to tape as it could overflow the output buffer if too many returned output files linger in the buffer for too long.

Job feeding

So far we have discussed first-pass efficiency exclusively, however there exist other efficiency metrics such as utilization efficiency, which is the percent of available slots versus the number of jobs actually running. When there exists a non-zero number of idle jobs on all sites, utilization efficiency will be one hundred percent of the resource, even in an opportunistic environment where the number of available slots changes with time. The key to achieving full utilization is to ensure a sufficient number of restored files. We have already discussed the method used to achieve restoration even with a small output buffer in section 3 of our paper. There exists a propagation delay, checking for input files, wrapping them into a job, submitting the jobs to the grid, and waiting for the batch system to do its matchmaking. But if we ensure there are always idle jobs for the batch system to grab the propagation time is irrelevant as propagation happens long before the slot is actually available. There are some inherent limits which lead to job feeding, for example, the whole dataset size cannot fit into the input buffer at one time, but even if the buffer could be sized to restore the entire dataset at once it is not ideal to submit them simultaneously as they would divide between sites with different capacities where one site finished well in advance of another. Attempting to calculate the capacity of a site providing opportunistic resources in order to pre-allocate workload (jobs) is impossible as it would require accurate knowledge of other users resource requests before

they actually make them. Instead, our production system polls the HTCondor client queue once per hour in order to keep a “pad” of idle jobs on each site as represented in Figure 42. When the idle job pad starts to deteriorate, and the jobs go into the running state, the feeder replenishes it by submitting more jobs up to the preconfigured limit. This forms a negative feedback loop holding the pad size essentially constant and insuring each sites workload is scaled correctly so that the dataset finishes on all site’s at approximately the same time.

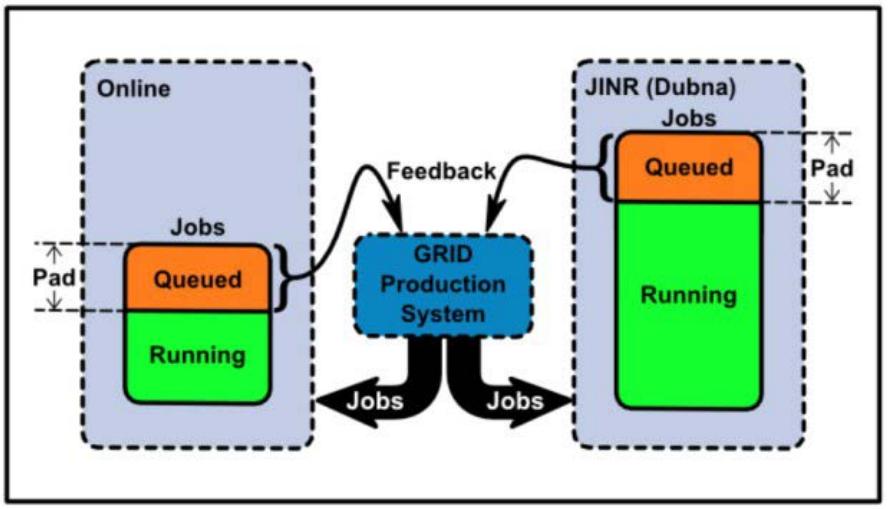

Figure 42: Jobs Feeding

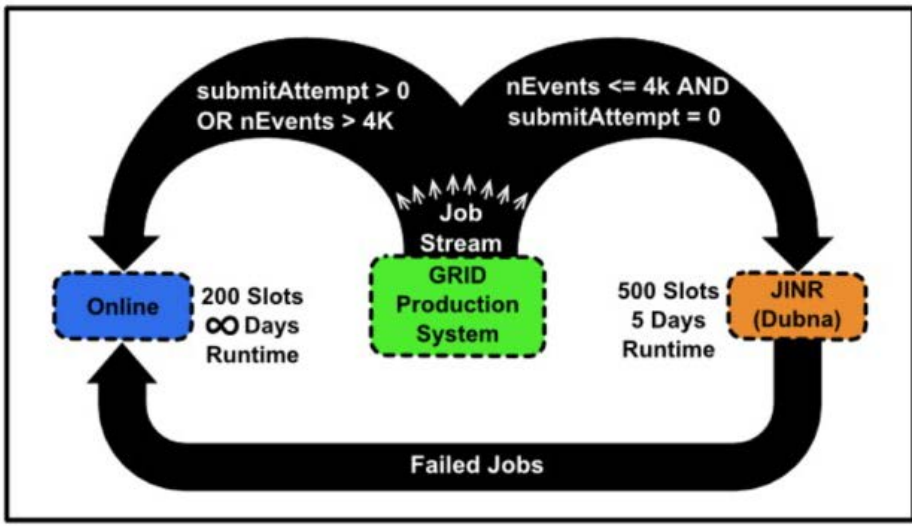

Figure 43: Multi-site feeding algorithm example

Site selection

To further boost efficiency the production system has some logic to do matchmaking at the site level. For example for a particular dataset which had a high number of tracks per event it was noted that some jobs were approaching the queue time limit of five days at JINR. A quick plot was produced of events versus runtime from jobs that had already been processed, and it was determined that four thousand events represent a point where the job is unlikely to exceed the queue limit. A rule was added for the dataset to only submit jobs containing four thousand events or less to JINR and pass the rest to the Online farm which has no queue time limit. And for good measure a second rule was added that if a job fails at JINR it should not be resubmitted there but instead to the Online farm. This will improve the second pass efficiency as jobs that exceed the time limit of the queue will not be retried on the same site where they are likely to fail again. This is a powerful feature but care needs to be taken to

ensure no inadvertent unbalance is caused between sites.

Efficiency

In a recent ten-month period, STAR successfully reconstructed 25,627 files containing 151 million events using JINR resources and our own Online farm. A breakdown of production statistics between the two sites can be seen in Table 8. It should be noted that the Online cluster has considerably fewer slots, takes longer jobs, and is only available after STAR finishes data-taking each year and so it has produced fewer files. Our first pass efficiency was 93.2% of all jobs returning valid input and log files in the first attempt with the remainder being resubmitted. Causes of job failures include jobs running past the queue runtime limits, AFS errors, gsiftp errors, and an Online farm power outage.

Table 8: Multi-site feeding algorithm example

Site	Files	Events	Runtime (Hours)	Dataset Size GB
Online:	4,847	27M	332,633	14,293
JINR:	20,780	138M	534,324	23,878
Total:	25,627	165M	866,957	38,171

MuDst PicoDst Update

At this moment, all past data has been produced or reproduced thanks to resources loaned from a few sites, JINR being one of them. As a result, we have not run more jobs since after the NEC 2017 conference and with the 2017 data production just starting 2 weeks ago locally, we are not expecting an immediate dataset scheduled at Dubna (not until we confirm the production is fine- issues with distortion correction at High PT requires the datasets go under further local scrutiny and investigation).

However, we have discussed attempting different workflows – the generation of picoDST from Micro-DST is a recent process by which, a more compact (and newly introduced) format could be produced from past data. The jobs are short, possibly a good match for the queue limitations at Dubna and pending a test on how many transfers we can sustain with the current infrastructure, we aim at directing the whole picoDST production at the JINR/Dubna site. Currently, over a million files production was requested from the PWG (but pending a code implementation and validation). We hope to continue at Dubna after we overcome these obstacles.

We reported 23,199 files produced (reconstructed) in our talk, 686,716 wall hours of runtime, and 30,367 GB of data produced. Images for the workflow, state diagram, production stages, plus the talk and paper were sent via Email.

Analysis of computing results at JINR for the STAR

The following figures (44–48) and tables (9–10) show statistics of computing of STAR data at JINR GRID cluster.

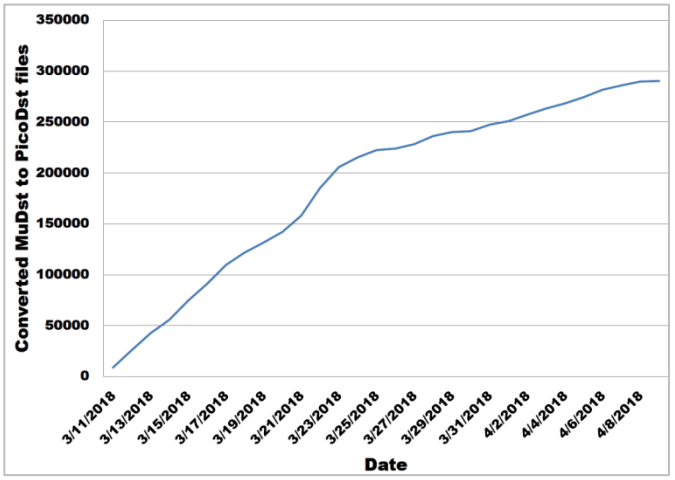

Figure 44: Files converted on JINR + Online.

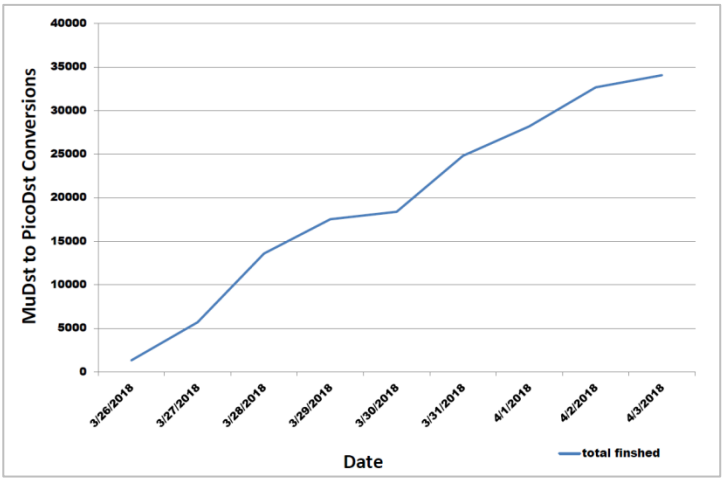

Figure 45: Total MuDst Files Finished pAu200_2015.

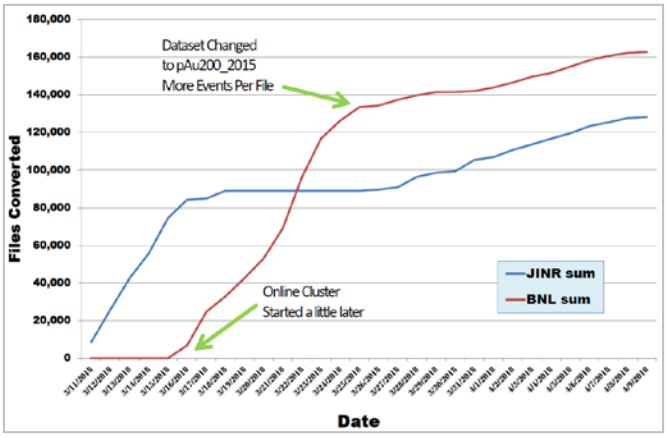

Figure 46: MuDst to PicoDst Files Converted Per Site.

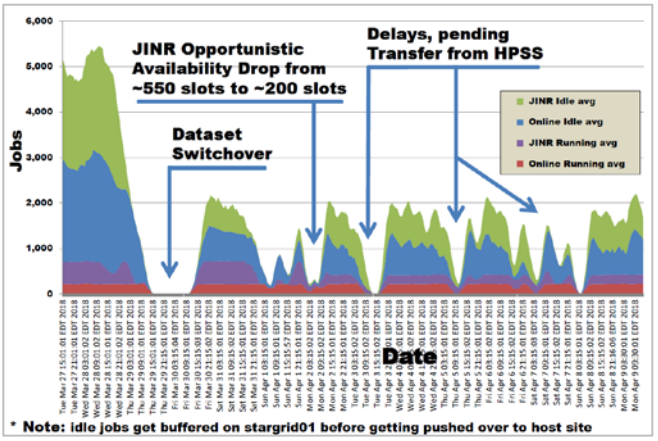

Figure 47: Running and Idle Jobs on JINR and Online site.

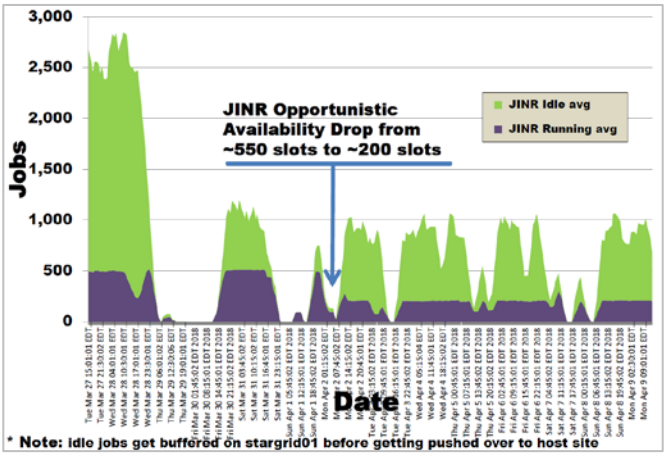

Figure 48: Running and Idle Jobs on JINR

Table 9: Real time data accumulation

Note: This page is for production purposes and does not reflect real-time dataset availability.
Taken from: http://www.star.bnl.gov/public/comp/prod/GRIDsummary.2017.html

Trigger Set	Prod Tag	Input Files On disk	Missing input files	Jobs SUBMITTED	Jobs RUNNING	Jobs FINISH	Jobs IDLE	Jobs HELD	Jobs notInQ	Jobs NOT SUBMITTED	Reco success	Average CPU/evt sec
production_pp200trans_2015	P17ii	2	0	0	0	30,738	0	0	0	1	30,738	0.11
production_pp200long2_2015	P17ii	2	0	0	0	35,812	0	0	3	0	35,814	0.13
production_pp200long_2015	P17ii	0	0	0	0	9,677	0	0	0	0	9,677	0.09
production_pp200long3_2015	P17ii	0	0	0	0	244	0	0	0	0	244	0.10
AuAu_200_production_low_2014	P18ib	0	0	0	0	88,435	0	0	0	0	88,415	0.44
AuAu_200_production_mid_2014	P18ib	0	0	0	0	134,201	0	0	0	9	134,201	0.48
production_pAu200_2015	P18ib	8,537	3894	0	410	32,620	1629	13	0	5613	32,620	0.19

CPU higher with fewer events per file

Table 10: MuDst → picoDst Production Summary Official Page for Analyzers

Taken from: http://www.star.bnl.gov/public/comp/prod/ProdSumPicoDst.html

Trigger setup name	Stream name	Collision	Year Data taken	Production Tag	Library Tag	Number of MuDst files	Number of Events in MuDst	Number of picoDst files	Size of picoDst (GB)	% of produced picoDst files
AuAu_200_production_mid_2014	st_physics_adc	auau200	year2014	P17id	SL18b	16253	7372216	16250	64.9	100.0
	st_physics	auau200	year2014	P17id	SL18b	117957	769106585	117949	6502	100.0
AuAu_200_production_low_2014	st_physics	auau200	year2014	P17id	SL18b	77802	514016848	77857	3756	100.1
	st_physics_adc	auau200	year2014	P17id	SL18b	10468	4965001	10471	37.6	100.0
production_pp200long_2015	st_mtd_adc	pp200	year2015	P16id	SL17i	3168	605587	3168	18.6	100.0
	st_mtd	pp200	year2015	P16id	SL17i	6509	61417248	6509	1860	100.0
production_pp200trans_2015	st_mtd	pp200	year2015	P16id	SL17i	23733	206879704	23733	9247	100.0
	st_mtd_adc	pp200	year2015	P16id	SL17i	7006	2009728	7006	90.7	100.0
production_pp200long3_2015	st_mtd	pp200	year2015	P16id	SL17i	181	1538918	181	63.1	100.0
	st_mtd_adc	pp200	year2015	P16id	SL17i	63	14924	63	0.62	100.0
production_pAu200_2015	st_physics	pAu200	year2015	P16id	SL18b	136019	1340113827	27694	13768	20.4
	st_physics_adc	pAu200	year2015	P16id	SL18b	21234	12512655	3795	111	17.9
production_pp200long2_2015	st_mtd	pp200	year2015	P16id	SL17i	28919	232164673	28918	11967	100.0
	st_mtd_adc	pp200	year2015	P16id	SL17i	6892	2267756	6892	118	100.0
cuProductionMinBias	st_physics	cucu200	year2005	P06ib	SL17d	62752	42930041	60670	1.00	96.7
	st_physics_adc	cucu200	year2005	P06ib	SL17d	19177	3598983	18985	0.31	99.0
	st_zerobias	cucu200	year2005	P06ib	SL17d	664	149765	664	0.01	100.0

Scavenging additional resources allows for the reconstruction of a few additional small datasets per year which allows additional analysis work in turn and is therefore of value to STAR. Our framework has an excellent first pass efficiency of 93.2%. The efficiency is comparable to, but slightly lower than, local efficiency, which is 98%, due to the additional complexity of the added software interfaces. STAR has put a lot of thought and iterative refinement into the design of this production system. Extensive preproduction testing and a well-structured finite state system applied to each job, with retries in the event of interruption, applied to each job contributes to this high efficiency. What makes this even more remarkable is that it is running on heterogeneous nodes.

References

[1] I. Arsene et al. Quark-gluon plasma and color glass condensate at RHIC? The perspective from the BRAHMS experiment. *Nucl. Phys.*, A757:1–27, 2005.

[2] B. B. Back et al. The PHOBOS perspective on discoveries at RHIC. *Nucl. Phys.*, A757:28–101, 2005.

[3] J. Adams et al. Experimental and theoretical challenges in the search for the quark–gluon plasma: The STAR Collaboration's critical assessment of the evidence from RHIC collisions. *Nucl. Phys.*, A757:102–183, 2005.

[4] K. Adcox et al. Formation of dense partonic matter in relativistic nucleus–nucleus collisions at RHIC: Experimental evaluation by the PHENIX Collaboration. *Nucl. Phys.*, A757:184–283, 2005.

[5] L. Adamczyk et al. Bulk Properties of the Medium Produced in Relativistic Heavy-Ion Collisions from the Beam Energy Scan Program. 2017.

[6] B.-J. Schaefer and J. Wambach. Susceptibilities near the QCD (tri)critical point. *Phys. Rev.*, D75:085015, 2007.

[7] D. H. Rischke et al. The Phase transition to the quark-gluon plasma and its effects on hydrodynamic flow. *Heavy Ion Phys.*, 1:309–322, 1995.

[8] H. Stöcker. Collective flow signals the quark–gluon plasma. *Nucl. Phys.*, A750:121–147, 2005.

[9] Arthur M. Poskanzer and S. A. Voloshin. Methods for analyzing anisotropic flow in relativistic nuclear collisions. *Phys. Rev.*, C58:1671–1678, 1998.

[10] L. Adamczyk et al. Beam-energy dependence of the directed flow of protons, antiprotons, and pions in Au+Au collisions. *Phys. Rev. Lett.*, 112:162301, 2014.

[11] Yasushi Nara, Akira Ohnishi, and Horst Stoecker. Directed flow as a signature of the softest point of the equation of state in QCD matter. 2016.

[12] J. Steinheimer, J. Auvinen, H. Petersen, M. Bleicher, and H. Stöcker. Examination of directed flow as a signal for a phase transition in relativistic nuclear collisions. *Phys. Rev. C*, 89:054913, May 2014.

[13] V. P. Konchakovski, W. Cassing, Yu. B. Ivanov, and V. D. Toneev. Examination of the directed flow puzzle in heavy-ion collisions. *Phys. Rev. C*, 90:014903, Jul 2014.

[14] W. Cassing, V. P. Konchakovski, A. Palmese, V. D. Toneev, and E. L. Bratkovskaya. *EPJ Web Conf.C*, 95:01004, 2014.

[15] P. Shanmuganathan. Beam-energy and centrality dependence of directed flow of identified particles. *Nucl. Phys.*, A956:260–263, 2016.

[16] S. Singha. Directed flow of $\Lambda, \bar{\Lambda}, K^{\pm}, K_S^0$ and ϕ mesons from Beam Energy Scan Au+Au collisions using the STAR experiment. *J. Phys.: Conf. Ser.*, 779:012066, 2017.

[17] S. Bass et al. Microscopic models for ultrarelativistic heavy ion collisions. *Prog. Part. Nucl. Phys.*, 41:255–369, 1998.

[18] Y. Hirono, M. Hongo, and T. Hirono. Estimation of the electric conductivity of the quark gluon plasma via asymmetric heavy-ion collision. *Phys. Rev.*, C90:021903, 2014.

[19] V. Voronyuk, V. D. Toneev, S. A. Voloshin, and W. Cassing. Charge-dependent directed flow in asymmetric nuclear collisions. *Phys. Rev.*, C90:064903, 2014.

[20] L. Adamczyk et al. Charge-dependent directed flow in Cu+Au collisions at $\sqrt{s_{NN}} = 200\,\mathrm{GeV}$. *Phys. Rev. Lett.*, 118:012301, 2017.

[21] L. Adamczyk et al. Centrality and transverse momentum dependence of elliptic flow of multistrange hadrons and $ meson in Au+Au collisions at $\sqrt{s_{NN}} = 200\,\mathrm{GeV}$. *Phys. Rev. Lett.*, 116:062301, 2016.

[22] S. Takeuchi, K. Murase, T. Hirano, P. Huovinen, and Y. Nara. Effects of hadronic rescattering on multistrange hadrons in high-energy nuclear collisions. *Phys. Rev.*, C92:044907, 2015.

[23] Z.-W. Lin, C. M. Ko, B.-A. Li, B. Zhang, and S. Pal. Multiphase transport model for relativistic heavy ion collisions. *Phys. Rev.*, C72:064901, 2005.

[24] L. Adamczyk et al. Observation of an Energy-Dependent Difference in Elliptic Flow between Particles and Antiparticles in Relativistic Heavy Ion Collisions. *Phys. Rev. Lett.*, 110(14):142301, 2013.

[25] L. Adamczyk et al. Centrality dependence of identified particle elliptic flow in relativistic heavy ion collisions at $\sqrt{s_{NN}} = 7.7 - 62.4\,\mathrm{GeV}$. *Phys. Rev.*, C93:014907, 2016.

[26] L. Adamczyk et al. Measurement of elliptic flow of light nuclei at $\sqrt{s_{NN}}$ = 200, 62.4, 39, 27, 19.6m 11.5 and 7.7 GeV at RHIC. *Phys. Rev.*, C94:034908, 2016.

[27] A. Andronic, P. Braun-Munzinger, J. Stachel, and H. Stocker. Production of light nuclei, hypernuclei and their antiparticles in relativistic nuclear collisions. *Phys. Lett.*, B697:203–207, 2011.

[28] Adam Bzdak and Derek Teaney. Longitudinal fluctuations of the fireball density in heavy-ion collisions. *Phys. Rev.*, C87:024906, 2013.

[29] J. Jia, S. Radhakrishnan, and M. Zhou. Forward-backward multiplicity fluctuation and longitudinal harmonics in high-energy nuclear collisions. *Phys. Rev.*, C93:044905, 2016.

[30] S. Jowzaee. Rapidity correlations in the RHIC Beam Energy Scan Data (in publishing). *Nucl. Phys.*, A, 2017.

[31] Liang Z.-T. and X.-N. Wang. Globally polarized quark-gluon plasma in noncentral A+A collisions. *Phys. Rev. Lett.*, 94:102301, 2005.

[32] F. Becattini, F. Piccinini, and J. Rizzo. Angular momentum conservation in heavy ion collisions at very high energy. *Phys. Rev.*, C77:024906, 2008.

[33] L.-G. Pang, H. Petersen, Q. Wang, and X.-N. Wang. Vortical fluid and Λ spin correlations in high-energy heavy-ion collisions. *Phys. Rev. Lett.*, 117:192301, 2016.

[34] L. Adamczyk et al. Global Λ hyperon polarization in nuclear collisions: evidence for the most vortical fluid. Nature 548, 62 (2017)

[35] B. I. Abelev et al. Global polarization measurement in Au+Au collisions. *Phys. Rev.*, C76:024915, 2007.

[36] F. Becattini, I. Karpenko, M. A. Lisa, I. Upsal, and S. A. Voloshin. Global hyperon polarization at local thermodynamic equilibrium with vorticity, magnetic field and feed-down.

[37] Dmitri Kharzeev. Parity violation in hot QCD: Why it can happen, and how to look for it. *Phys. Lett.*, B633:260–264, 2006.

[38] Dmitri E. Kharzeev, Larry D. McLerran, and Harmen J. Warringa. The Effects of topological charge change in heavy ion collisions: 'Event by event P and CP violation'. *Nucl. Phys.*, A803:227–253, 2008.

[39] Sergei A. Voloshin. Parity violation in hot QCD: How to detect it. *Phys. Rev.*, C70:057901, 2004.

[40] Scott Pratt, Soeren Schlichting, and Sean Gavin. Effects of Momentum Conservation and Flow on Angular Correlations at RHIC. *Phys. Rev.*, C84:024909, 2011.

[41] Adam Bzdak, Volker Koch, and Jinfeng Liao. Charge-Dependent Correlations in Relativistic Heavy Ion Collisions and the Chiral Magnetic Effect. *Lect. Notes Phys.*, 871:503–536, 2013.

[42] Soren Schlichting and Scott Pratt. Charge conservation at energies available at the BNL Relativistic Heavy Ion Collider and contributions to local parity violation observables. *Phys. Rev.*, C83:014913, 2011.

[43] B. I. Abelev et al. Azimuthal Charged-Particle Correlations and Possible Local Strong Parity Violation. *Phys. Rev. Lett.*, 103:251601, 2009.

[44] B. I. Abelev et al. Observation of charge-dependent azimuthal correlations and possible local strong parity violation in heavy ion collisions. *Phys. Rev.*, C81:054908, 2010.

[45] Gang Wang. Search for Chiral Magnetic Effects in High-Energy Nuclear Collisions. *Nucl. Phys.*, A904-905:248c–255c, 2013.

[46] L. Adamczyk et al. Fluctuations of charge separation perpendicular to the event plane and local parity violation in $\sqrt{s_{NN}} = 200\,\mathrm{GeV}$ Au+Au collisions at the BNL Relativistic Heavy Ion Collider. *Phys. Rev.*, C88(6):064911, 2013.

[47] L. Adamczyk et al. Beam-energy dependence of charge separation along the magnetic field in Au+Au collisions at RHIC. *Phys. Rev. Lett.*, 113:052302, 2014.

[48] Betty Abelev et al. Charge separation relative to the reaction plane in Pb-Pb collisions at $\sqrt{s_{NN}} = 2.76\,\mathrm{TeV}$. *Phys. Rev. Lett.*, 110(1):012301, 2013.

[49] Shuzhe Shi and Jinfeng Liao. private communication.

[50] Vardan Khachatryan et al. Observation of charge-dependent azimuthal correlations in pPb collisions and its implication for the search for the chiral magnetic effect. *Phys. Rev. Lett.*, 2016. [Phys. Rev. Lett.118, 122301(2017)].

[51] Prithwish Tribedy. Disentangling flow and signals of Chiral Magnetic Effect in U+U, Au+Au and p+Au collisions. In *26th International Conference on Ultrarelativistic Nucleus-Nucleus Collisions (Quark Matter 2017) Chicago,Illinois, USA, February 6-11, 2017*, 2017.

[52] Sandeep Chatterjee and Prithwish Tribedy. Separation of flow from the chiral magnetic effect in U + U collisions using spectator asymmetry. *Phys. Rev.*, C92(1):011902, 2015.

[53] A. Adare et al. Transverse energy production and charged-particle multiplicity at midrapidity in various systems from $\sqrt{s_{\mathrm{NN}}} = 7.7$ to $200\,\mathrm{GeV}$. *Phys. Rev.*, C93(2):024901, 2016.

[54] D. T. Son and Ariel R. Zhitnitsky. Quantum anomalies in dense matter. *Phys. Rev.*, D70:074018, 2004.

[55] Max A. Metlitski and Ariel R. Zhitnitsky. Anomalous axion interactions and topological currents in dense matter. *Phys. Rev.*, D72:045011, 2005.

[56] Yannis Burnier, Dmitri E. Kharzeev, Jinfeng Liao, and Ho-Ung Yee. Chiral magnetic wave at finite baryon density and the electric quadrupole moment of quark-gluon plasma in heavy ion collisions. *Phys. Rev. Lett.*, 107:052303, 2011.

[57] G. M. Newman. Anomalous hydrodynamics. *JHEP*, 01:158, 2006.

[58] L. Adamczyk et al. Observation of charge asymmetry dependence of pion elliptic flow and the possible chiral magnetic wave in heavy-ion collisions. *Phys. Rev. Lett.*, 114(25):252302, 2015.

[59] Adam Bzdak and Piotr Bozek. Contributions to the event-by-event charge asymmetry dependence for the elliptic flow of pi^{+} and pi^{-} in heavy-ion collisions. *Phys. Lett.*, B726:239–243, 2013.

[60] Qi-Ye Shou. Charge asymmetry dependence of π/K anisotropic flow in Au + Au and U + U collisions at RHIC. *Nucl. Phys.*, A931:758–762, 2014.

[61] Yoshitaka Hatta, Akihiko Monnai, and Bo-Wen Xiao. Elliptic flow difference of charged pions in heavy-ion collisions. *Nucl. Phys.*, A947:155–160, 2016.

[62] Sergei A. Voloshin. Testing the Chiral Magnetic Effect with Central U+U collisions. *Phys. Rev. Lett.*, 105:172301, 2010.

[63] Wei-Tian Deng, Xu-Guang Huang, Guo-Liang Ma, and Gang Wang. Test the chiral magnetic effect with isobaric collisions. *Phys. Rev.*, C94:041901, 2016.

[64] S. Raman, C. W. G. Nestor, Jr, and P. Tikkanen. Transition probability from the ground to the first-excited 2+ state of even-even nu clides. *Atom. Data Nucl. Data Tabl.*, 78:1–128, 2001.

[65] B. Pritychenko, M. Birch, B. Singh, and M. Horoi. Tables of E2 Transition Probabilities from the first 2+ States in Even-Even Nuclei. *Atom. Data Nucl. Data Tabl.*, 107:1, 2016.

[66] P. Moller, J. R. Nix, W. D. Myers, and W. J. Swiatecki. Nuclear ground state masses and deformations. *Atom. Data Nucl. Data Tabl.*, 59:185–381, 1995.

[67] A. Hennig et al. Collective excitations of Ru96 by means of (p,p$'$ γ) experiments.

Phys. Rev., C92(6):064317, 2015.

[68] Tomoaki Togashi, Yusuke Tsunoda, Takaharu Otsuka, and Noritaka Shimizu. Quantum Phase Transition in the Shape of Zr isotopes. *Phys. Rev. Lett.*, 117(17):172502, 2016.

[69] B. I. Abelev et al. Observation of Two-source Interference in the Photoproduction Reaction Au Au → Au Au rho0. *Phys. Rev. Lett.*, 102:112301, 2009.

[70] J. Adams et al. Production of e+ e^{-} pairs accompanied by nuclear dissociation in ultra-peripheral heavy ion collision. *Phys. Rev.*, C70:031902, 2004.

[71] STAR. SN0666 - An Event Plane Detector for STAR.

[72] N. Brambilla et al. Heavy quarkonium: progress, puzzles, and opportunities. *Eur. Phys. J.*, C71:1534, 2011.

[73] STAR. SN0598 - Studying the Phase Diagram of QCD Matter at RHIC. March 2014. STAR Note SN0598.

[74] STAR. SN0644 - Technical Design Report for the iTPC Upgrade.

[75] Physics Program for the STAR/CBM eTOF Upgrade. 2016.

[76] L. Adamczyk et al. Beam-Energy Dependence of the Directed Flow of Protons, Antiprotons, and Pions in Au+Au Collisions. *Phys. Rev. Lett.*, 112(16):162301, 2014.

[77] Y. Aoki, Z. Fodor, S. D. Katz, and K. K. Szabo. The QCD transition temperature: Results with physical masses in the continuum limit. *Phys. Lett.*, B643:46–54, 2006.

[78] Y. Aoki, D. Endrodi, Z. Fodor, S. D. Katz, and K. K. Szabo. The order of the quantum chromodynamics transition predicted by the standard model of particle physics. *Nature*, 443:675–678, 2006.

[79] M. A. Stephanov. Non-Gaussian fluctuations near the QCD critical point. *Phys. Rev. Lett.*, 102:032301, 2009.

[80] Masayuki Asakawa, Shinji Ejiri, and Masakiyo Kitazawa. Third moments of conserved charges as probes of QCD phase structure. *Phys. Rev. Lett.*, 103:262301, 2009.

[81] M. A. Stephanov. On the sign of kurtosis near the QCD critical point. *Phys. Rev. Lett.*, 107:052301, 2011.

[82] L. Adamczyk et al. Energy Dependence of Moments of Net-proton Multiplicity Distributions at RHIC. *Phys. Rev. Lett.*, 112:032302, 2014.

[83] F. Karsch and K. Redlich. Probing freeze-out conditions in heavy ion collisions with moments of charge fluctuations. *Phys. Lett.*, B695:136–142, 2011.

[84] M. Bleicher et al. Relativistic hadron-hadron collisions in the ultra-relativistic quantum molecular dynamics model. *J. Phys.*, G25:1859, 1999.

[85] Adam Bzdak and Volker Koch. Acceptance corrections to net baryon and net charge cumulants. Phys. Rev., C86:044904, 2012.

[86] J. Brachmann, S. Soff, A. Dumitru, Horst Stoecker, J. A. Maruhn, W. Greiner, V. Bravina, and D. H. Rischke. Antiflow of nucleons at the softest point of the EoS. *Phys. Rev.*, C61:024909, 2000.

[87] B. Mohanty and N. Xu. Probe the QCD phase diagram with phi-mesons in high energy nuclear collisions. *J. Phys.*, G36:064022, 2009.

[88] Md. Nasim, Bedangadas Mohanty, and Nu Xu. Elliptic flow of ϕ mesons as a sensitive probe for the onset of the deconfinement transition in high energy heavy-ion collisions. *Phys. Rev.*, C87(1):014903, 2013.

[89] B. I. Abelev et al. Energy and system size dependence of phi meson production in Cu+Cu and Au+Au collisions. *Phys. Lett.*, B673:183–191, 2009.

[90] R. Rapp. Signatures of thermal dilepton radiation at RHIC. *Phys. Rev.*, C63:054907, 2001.

[91] Ralf Rapp and Hendrik van Hees. Thermal Dileptons as Fireball Thermometer and Chronometer. *Phys. Lett.*, B753:586–590, 2016.

[92] Paul M. Hohler and Ralf Rapp. Is *p*-Meson Melting Compatible with Chiral Restoration? *Phys. Lett.*, B731:103–109, 2014.

[93] R. V. Gavai and S. Gupta. QCD at finite chemical potential with six time slices. *Phys. Rev.*, D78:114503, 2008.

[94] T. Anticic et al. Centrality dependence of proton and antiproton spectra in Pb+Pb collisions at 40A GeV and 158A GeV measured at the CERN SPS. *Phys. Rev.*, C83:014901, 2011.

[95] Jean Cleymans. Recent developments around chemical equilibrium. *J. Phys.*, G37:094015, 2010.

[96] B. I. Abelev et al. Systematic measurements of identified particle spectra in pp, d+Au, and Au+Au collisions at the STAR detector. *Phys. Rev.*, C79:034909, 2009.

[97] D. Cebra, S. G. Brovko, C. E. Flores, B. A. Haag, and J. L. Klay. Coulomb effect in Au+Au and Pb+Pb collisions as a function of collision energy. 2014.

[98] L. Adamczyk et al. Dielectron Mass Spectra from Au+Au Collisions at $\sqrt{s_{NN}} = 200\,\mathrm{GeV}$. *Phys. Rev. Lett.*, 113(2):022301, 2014. [Addendum: Phys. Rev. Lett.113,no.4,049903(2014)].

[99] L. Adamczyk et al. Measurements of Dielectron Production in Au+Au Collisions at $\sqrt{s_{NN}} = 200\,\mathrm{GeV}$ from the STAR Experiment. *Phys. Rev.*, C92(2):024912, 2015.

[100] T. C. Huang et al. Muon Identification with Muon Telescope Detector at the STAR Experiment. *Nucl. Instrum. Meth.*, A833:88–93, 2016.

[101] Jan Steinheimer and Jorgen Randrup. Spinodal amplification of density fluctuations in fluid-dynamical simulations of relativistic nuclear collisions. *Phys. Rev. Lett.*, 109:212301, 2012.

[102] C. Alt et al. Pion and kaon production in central Pb + Pb collisions at 20-A and 30-A-GeV: Evidence for the onset of deconfinement. *Phys. Rev.*, C77:024903, 2008.

[103] L. Adamczyk et al. Beam-Energy Dependence of Charge Balance Functions from Au+Au Collisions at RHIC. Submitted Jul. 13, 2015.

[104] P. Chung et al. Near threshold production of the multistrange xihyperon. *Phys. Rev. Lett.*, 91:202301, 2003.

[105] J. Adams et al. Multi-strange baryon elliptic flow in Au + Au collisions at s(NN)**(1/2) = 200-GeV. *Phys. Rev. Lett.*, 95:122301, 2005.

[106] Scott Pratt. General Charge Balance Functions, A Tool for Studying the Chemical Evolution of the Quark-Gluon Plasma. *Phys. Rev.*, C85:014904, 2012.

[107] Horst Stoecker. Collective flow signals the quark gluon plasma. *Nucl. Phys.*, A750:121–147, 2005.

[108] H. Liu et al. Sideward flow in Au + Au collisions between 2-A-GeV and 8-A-GeV. *Phys. Rev. Lett.*, 84:5488–5492, 2000.

[109] Michael Annan Lisa, Ulrich W. Heinz, and Urs Achim Wiedemann. Tilted pion sources from azimuthally sensitive HBT interferometry. *Phys. Lett.*, B489:287–292, 2000.

[110] M. A. Lisa et al. Azimuthal dependence of pion interferometry at the AGS. *Phys. Lett.*, B496:1–8, 2000.

[111] M. A. Lisa, E. Frodermann, G. Graef, M. Mitrovski, E. Mount, H. Petersen, and

Bleicher. Shape analysis of strongly-interacting systems: The Heavy ion case. *New J. Phys.*, 13:065006, 2011.

[112] Michael Annan Lisa, Scott Pratt, Ron Soltz, and Urs Wiedemann. Femtoscopy in relativistic heavy ion collisions. *Ann. Rev. Nucl. Part. Sci.*, 55:357–402, 2005.

[113] Hannah Petersen and Marcus Bleicher. Longitudinal flow and onset of deconfinement. *PoS*, CPOD2006:025, 2006.

[114] C. Pinkenburg et al. Elliptic flow: Transition from out-of-plane to in-plane emission in Au + Au collisions. *Phys. Rev. Lett.*, 83:1295–1298, 1999.

[115] G. Baym and P. Braun-Munzinger. *Nucl. Phys. A*, 610:286c, 1996.

[116] Ralf Rapp and Hendrik van Hees. Thermal dileptons as fireball thermometer and chronometer. *Physics Letters B*, 753:586 – 590, 2016.

[117] S. V. Afanasiev et al. Event-by-event fluctuations of the kaon to pion ratio in central Pb + Pb collisions at 158-GeV per nucleon. *Phys. Rev. Lett.*, 86:1965–1969, 2001.

[118] L. Adamczyk et al. Beam energy dependence of moments of the net-charge multiplicity distributions in Au+Au collisions at RHIC. *Phys. Rev. Lett.*, 113:092301, 2014.

[119] A. Adare et al. Measurement of higher cumulants of net-charge multiplicity distributions in Au+Au collisions at $\sqrt{s_{NN}}$ = 7.7 – 200 GeV. 2015.

[120] Yataro Sekido and Harry Elliot. *Early History of Cosmic Ray Studies*, page 323. D. Reidel Publishing Company, 1985.

[121] B. I. Abelev. Observation of an Antimatter Hypernucleus. *Science*, 328:58–62, 2010.

[122] H. Agakishiev et al. Observation of the antimatter helium-4 nucleus. *Nature*, 473:353, 2011. [Erratum: Nature475,412(2011)].

[123] Hajdu L. et al. Automated Finite State Workflow for Distributed Data Production // Journal of Physics: Conference Series, 762 012006 doi:10.1088/1742-6596/762/1/012006

[124] Allcock W. 2003 GridFTP: Protocol Extensions to FTP for the grid (Global Grid Forum GFD) page 20

[125] Pordes R. et al. The Open Science Grid // Journal of Physics: Conference Series, 2007, Vol. 78, Boston, Massachusetts, USA

[126] Andreetto P. et al. Status and Developments of the CREAM Computing Element Service // Journal of Physics: Conference Series, 2011, doi:10.1088/1742-6596/331/6/062024

[127] Bockelman B. et al. Commissioning the HTCondor-CE for the Open Science Grid // Journal of Physics: Conference Series, 2015, doi:10.1088/1742-6596/664/6/062003

[128] Ceccanti A. et al. VOMS/VOMRS utilization patterns and convergence plan // Journal of Physics: Conference Series, 2010, doi:10.1088/1742-6596/219/6/062006

[129] Hajdu L. et al. Meta-configuration for dynamic resource brokering: the SUMS approach (2006 International Conference on Computing in High Energy and Nuclear Physics, Tata Institute of Fundamental Research, Mumbai, India)

[130] Lauret J. et al. ERADAT and Data Carousel systems at BNL: A tool and UI for efficient access to data on tape with fair share policies capabilities (2010 ACAT 2010 proceedings, PoS ACAT 023)

[131] Lauret J. et al. Tape storage optimization at BNL (CHEP 2010 proceedings) // Journal of Physics: Conference Series, 331 042045 doi:10.1088/1742-6596/331/4/042045

Appendix 1. Data analysis. The specific JINR Contribution

The specific JINR Contributions related to participation in the STAR research program in 2015–2017 are following:

- ***Spectra of charged particles production in BES-I***

M.V. Tokarev (for the STAR Collaboration). Int. J. Mod. Phys. (2015) 1560103.

The JINR team of the STAR collaboration takes part in the analysis of the BES-I data. The original method of data analysis has been suggested and exploited for search for new phenomena in nuclear matter created in heavy ion collisions. The preliminary STAR data shown in Figure A1.1 covers a wide kinematical and dynamical range of particle production, collision energy $\sqrt{s_{NN}}$ = 7–200 GeV, centrality of collisions 5 %–80 % and momentum range p_T = 0.2–12 GeV/c.

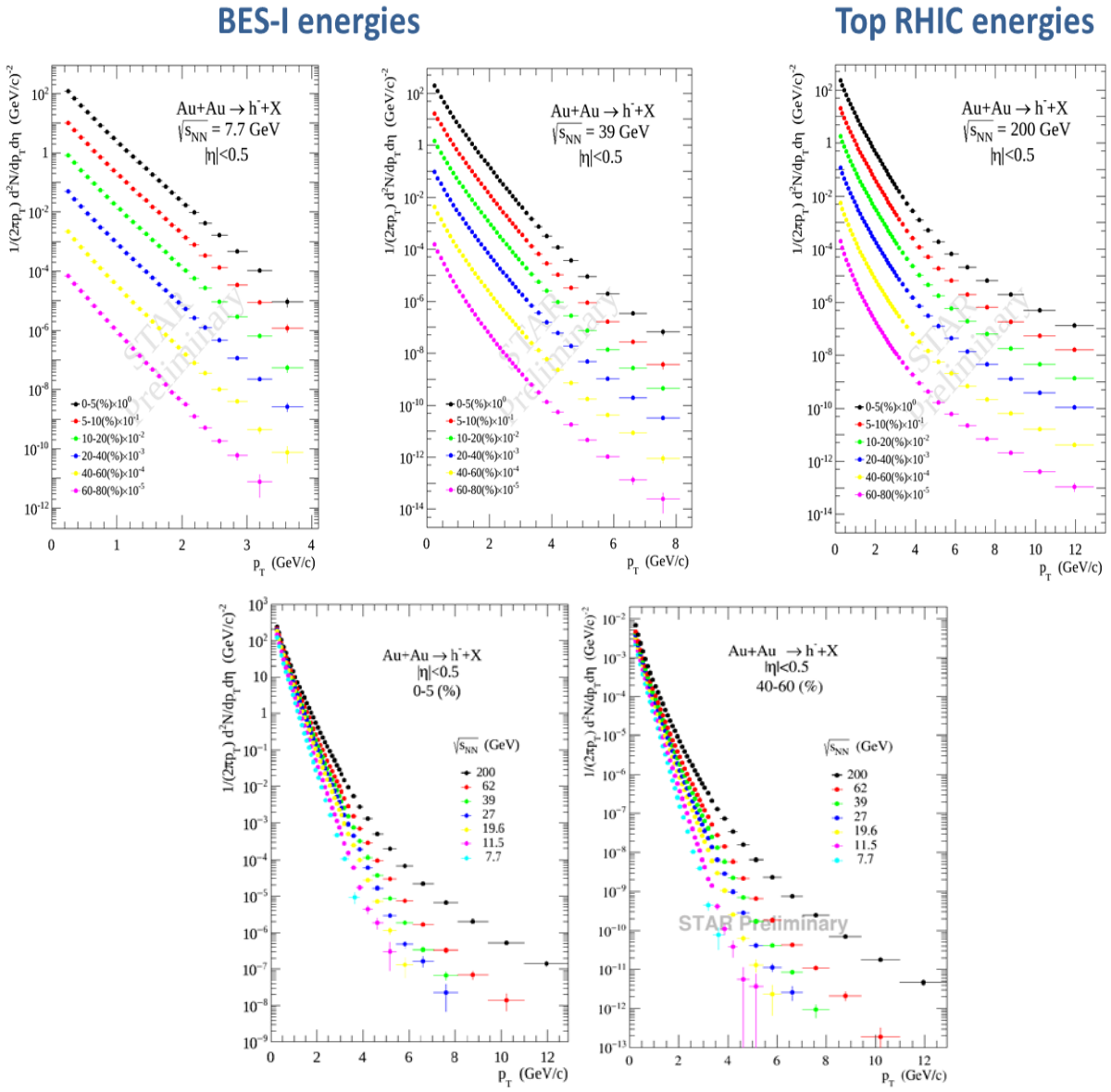

Figure A1.1. Transverse momentum distribution of negative charged particles production at BES-I energies as a function of centrality.

As one seen from Figure A1.1 the data demonstrate strong energy and centrality dependence of spectra, exponential behavior of the spectra at low p_T and energy $\sqrt{s_{NN}}$, a power behavior of spectra at high p_T and energy $\sqrt{s_{NN}}$. One observes that difference of yields at various energies strongly increases with transverse momentum.

The analysis of the obtained spectra has been performed in the framework of the *z*-scaling approach (Phys. Rev. D75, 2007, 094008; Int. J. Mod. Phys. A24, 2009, 1417; Nucl. Phys. Suppl. B245, 2013, 231). The results of data *z*-presentation are shown in Figure A1.2. The results demonstrate a "collapse" of data onto a single curve. This is confirmation of self-similarity of particle production in heavy ion collision over a wide scale range. The shape of the curve reveals the power behavior at low and high *z*. The energy dependence of the fractal and fragmentation dimensions and "specific heat" was found. The decrease of the fractal dimension δ_A of the nucleus at energy $\sqrt{s_{NN}}$ < 20 GeV was found.

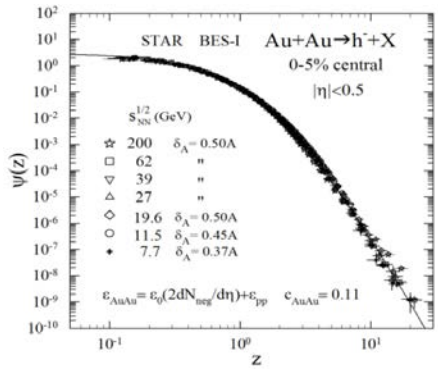

Figure A1.2. *z*-presentation of transverse momentum distribution of negative charged particle production at BES energies 7.7, 11.5, 19.6, 27, 39, 62.4, and 200 GeV at different centralities and central rapidity range.

Figure A1.3 shows the dependence of the constituent energy loss on the energy and centrality of collisions and transverse momentum of inclusive particle. It was found the energy loss decreases with p_T , increases with $\sqrt{s_{NN}}$ and centrality.

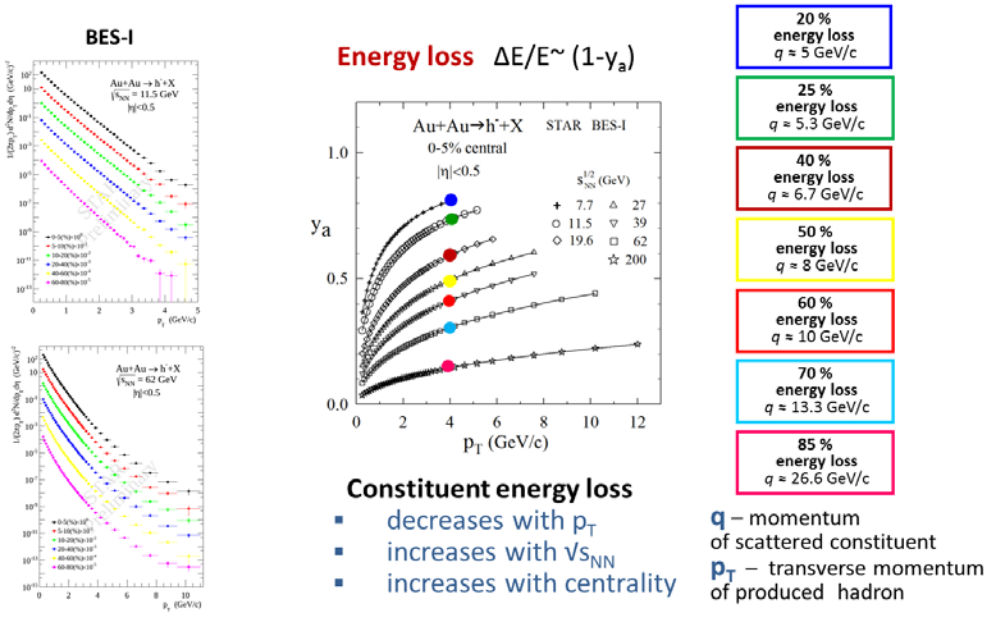

Figure A1.3. Momentum fraction y_a as a function of the energy and centrality of collision and the transverse momentum of inclusive particle.

The model parameters – nucleus fractal dimension δ_A, fragmentation fractal dimension ε_{AA}, and "heat capacity" c, are determined from the requirement of scaling behavior of $\Psi(z)$ as a function of self-similarity parameter z. The fractal dimension of the nucleus and the fragmentation dimension are equal to $\delta_A = A \cdot \delta$ and $\varepsilon_{AA} = \varepsilon_0(dN/d\eta) + \varepsilon_{pp}$, respectively. Figure A1.4 shows the dependence of these parameters on the collision energy. It was found that δ is independent of the energy for $\sqrt{s_{NN}} \geq 20$ GeV, ε_0 increases with the energy and c is independent of the energy over the range $\sqrt{s_{NN}} =$ 7.7–200 GeV. Note that, while δ decreases with decreased energy for $\sqrt{s_{NN}} \leq 20$ GeV, the function $\Psi(z)$ preserves the shape in this range.

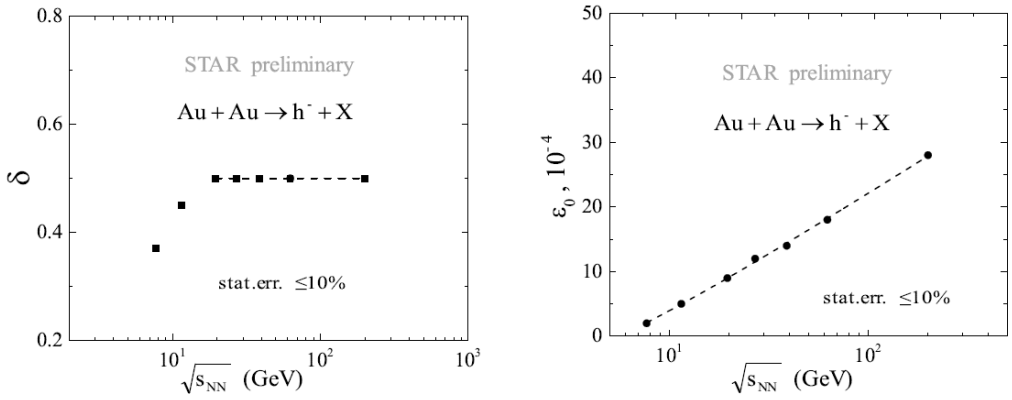

Figure A1.4.Model parameters δ and ε_0 as a function of collision energy $\sqrt{s_{NN}}$.

- ***The first high statistics measurement of ΛΛ correlation***

Phys. Rev. Lett. 114, 022301 (2015)

A new and extremely interesting physical results were obtained with the active participation of JINR physicists in collaboration with colleagues from the Czech Republic, Slovakia and Russia using the methods of correlation femtoscopy: first high statistics measurement of $\Lambda - \Lambda$ correlation function in Au + Au collisions at $\sqrt{s_{NN}}$ = 200 GeV. This research pioneered the venue of using RHIC as a hyperon factory to investigate hyperon-hyperon interactions. The STAR measurement can provide precious data for understanding of the hyperon-hyperon interaction which is an important input to various baryon-baryon interaction potential model as well as for the study of equation of state for neutron stars. The $\Lambda - \Lambda$ interaction is also closely related to the existence of the H dibaryon, one of the most searched for exotic hadrons in nuclear collisions.

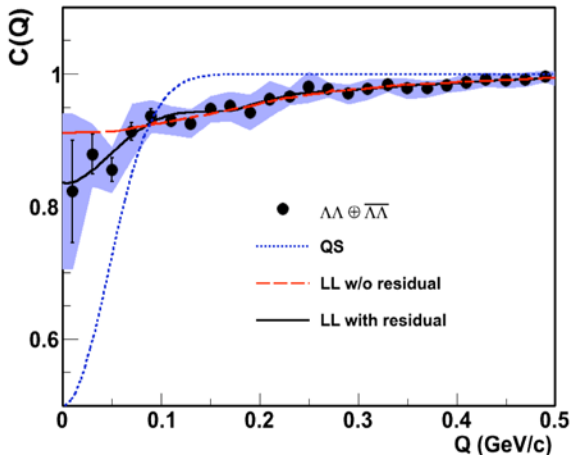

Figure A1.5. Correlation functions of $\Lambda - \Lambda$ and $\overline{\Lambda} - \overline{\Lambda}$ hyperon pairs.

The combined $\Lambda-\Lambda$ and $\overline{\Lambda}-\overline{\Lambda}$ correlation function for 0–80 % centrality Au + Au collisions at $\sqrt{s_{NN}}$ = 200 GeV. Curves on Figure A1.5 correspond to fits using the Lednicky and Lyuboshitz analytical model with and without a residual correlation term. The dotted line corresponds to Fermi statistics with a source size of 3.13 fm. The shaded band corresponds to the systematic error.

- ***Measurement of interaction between antiprotons***

Nature 527 (2015) 345.

One of the primary goals of Nuclear Physics is to understand the force between nucleons, which is necessary step for understanding the structure of nuclei and how nuclei interact with each other. Although anti-nuclei up to anti-helium-4 have been discovered and their masses measured, little is known directly about the nuclear forces between antinucleons. Here we study antiproton pair correlations among data collected by the STAR experiment with gold ions at 200 GeV per nucleon. Antiprotons are abundantly produced at such collisions. Thus making feasible to study details of the antiproton-antiproton interactions. Studies of two anti-proton correlation functions with data taken by the STAR experiment at RHIC show the attracting nuclear force between two anti-protons. The measurement of the two key parameters that charactering the corresponding strong interaction, namely, the scattering length (f_0) and effective range (d_0) are presented in Figure A1.6. As a direct knowledge from the interaction between two anti-protons, the simplest system of anti-nucleons (nuclei), our result provides a fundamental ingredient for understanding the structure of more sophisticated anti-nuclei and their properties.

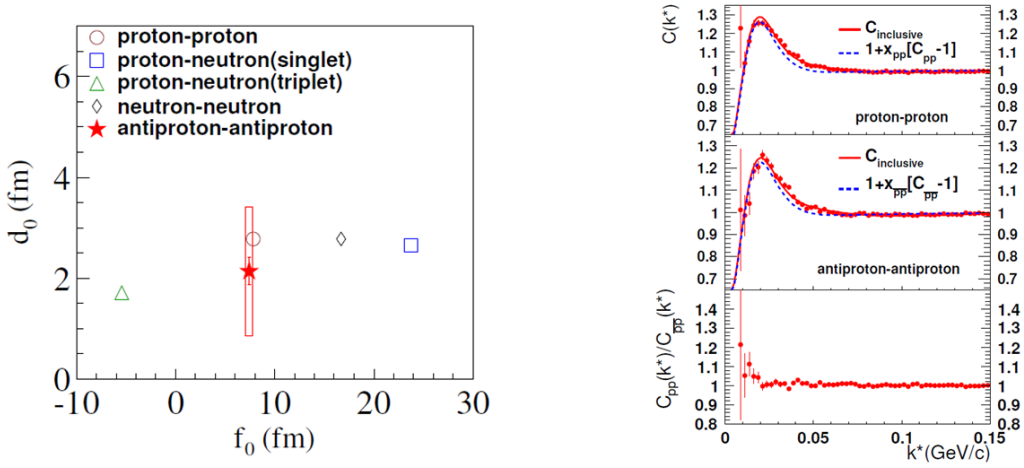

Figure A1.6. Correlation functions of $N-N$ and $\overline{N}-\overline{N}$ pairs.

- ***Self-similarity of hard cumulative processes in fixed target experiment for BES-II at STAR***

Physics of Particles and Nuclei Letters, V.12, №2, 2015, pp.324–338

Search for signatures of phase transition in Au + Au collisions is in the heart of the heavy ion program at RHIC. Systematic study of particle production over a wide range of collision energy revealed new phenomena such as the nuclear suppression effect expressed by nuclear modification factor, the constituent quark number scaling for elliptic flow, the "ridge effect" in $\Delta\phi-\Delta\eta$ fluctuations etc. To determine the phase boundaries and location of the critical point of nuclear

matter the Beam Energy Scan (BES-I) program at RHIC has been suggested and performed by STAR and PHENIX Collaborations. The obtained results shown that the program (BES-II) should be continued. In this paper a proposal to use hard cumulative processes in BES Phase-II program is outlined. Selection of the cumulative events is assumed to enrich data sample by new type of collisions characterized by higher energy density and more compressed matter. This would allow finding clearer signatures of phase transition, location of a critical point and studying extreme conditions in heavy ion collisions.

- ***Self-similarity of proton spin and asymmetry of jet production***

Physics of Particles and Nuclei Letters, V.12, №2, 2015, pp.313–323

Spin is one of the most fundamental properties of elementary particles. The proton spin structure is studied for a long time in processes with polarized leptons and protons. The goal is to understand complete picture of the proton spin in terms of quark and gluon degrees of freedom. Microscopic scenario of proton structure implies knowledge of momentum and spin distributions of its constituents at different scales. In the framework of QCD, the non-linear Yang-Mills equations taking into account gauge invariance and Lorentz covariance regulate dynamics of the constituent interactions both at hard and soft regimes.

The concept of *z*-scaling is applied for description of jet production in processes with polarized protons. The double longitudinal spin asymmetry A_{LL} of inclusive jets produced in proton-proton collisions at $\sqrt{s}$ = 200 GeV (Phys. Rev. Lett. 115, (2015) 092002) measured by STAR Collaboration at RHIC is shown in Figure A1.7. The asymmetry was analyzed in the framework of *z*-scaling approach. A hypothesis of self-similarity and fractality of the proton spin structure are suggested and discussed. The possibilities to extract information on spin-dependent fractal dimensions of proton and jet fragmentation process from the asymmetry are justified. The spin-dependent fractal dimension of proton is estimated.

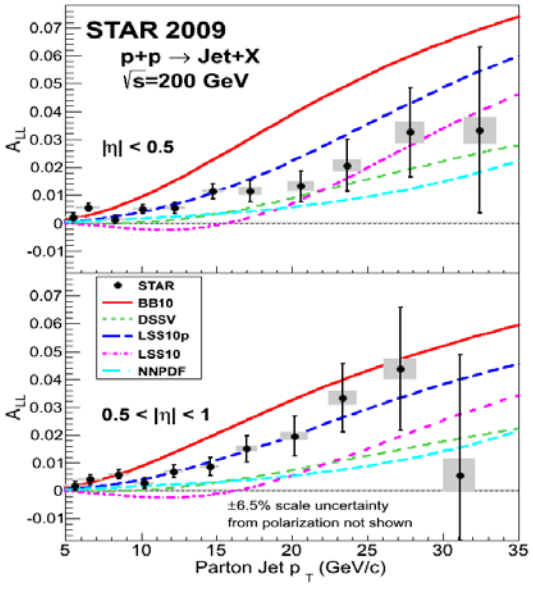

Figure A1.7. Double longitudinal spin asymmetry of jet production in polarized p-p collisions at $\sqrt{s}$ = 200 GeV, measured by the STAR collaboration.

Figure A1.8 shows the cross section of inclusive jet production in $\vec{p}+\vec{p} \rightarrow jet+X$ reaction in *z*-

presentation and the ratio of the spin-dependent and the spin independent scaling functions and the corresponding parameters δ_1 and δ_2.The functions coincide each other with high accuracy in all considered region of z . The coincidence is the indication on self-similarity of polarization processes in the z -scaling approach.

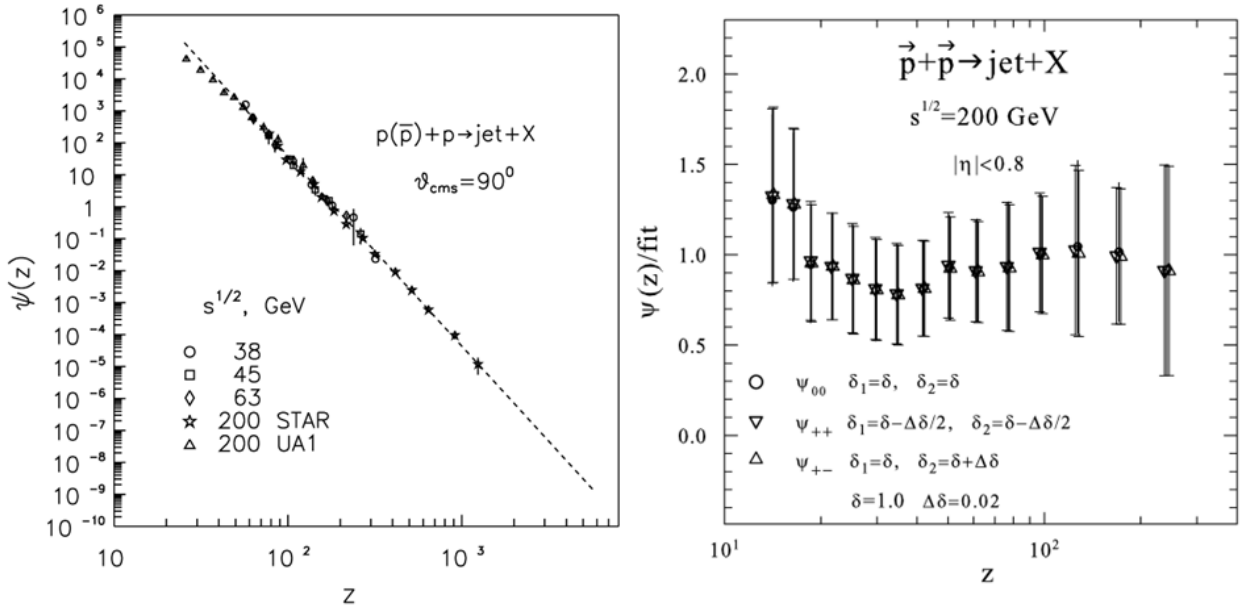

Figure A1.8. The ratios of the scaled spin-dependent and spin-independent functions for inclusive jet production in polarized p-p collisions at $\sqrt{s}$ = 200 GeV.

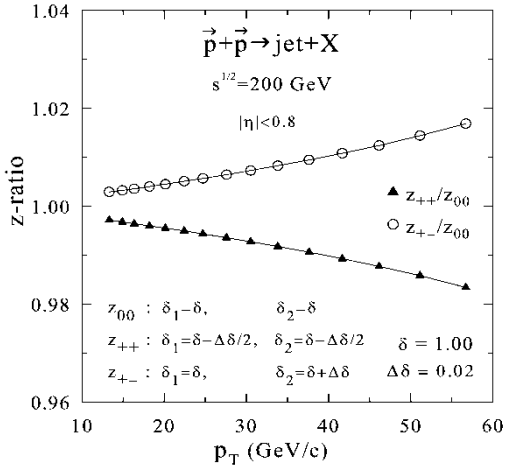

Figure A1.9. The ratios of the spin-dependent self-similarity parameters for inclusive jet production in polarized p-p collisions at $\sqrt{s}$ = 200 GeV.

The respective ratios of the spin-dependent self-similarity parameters $(z_{++}/z_{00}, z_{+-}/z_{00})$ as functions of the transverse momentum are shown in Figure A1.9. The effect of spin-spin interactions on the ratios does not exceed 4%. Such a difference agrees with values of the spin asymmetry A_{LL} which have similar magnitudes in the high- p_T region. The ratio decreases as function of p_T for the interactions of protons with the same (positive or negative) helicities and increases with p_T for the opposite orientation of proton helicities. The larger values of z_{+-} mean that spin structure of proton can be probed with higher resolution (i.e. at smaller scales) in the collisions of protons with opposite helicities relative to the interactions where the protons have the same helicities. If the collision is viewed as a clash of two fractals, the collisions of polarized

protons can be viewed as clashing of mutually spinning fractals with fractal spin connections like an "internal screw-screw connection". We expect that the features of the proton spin structure could manifest itself more prominently at high p_T. Similarly as for unpolarized processes, an abrupt change of the spin-dependent fractal dimensions should indicate on a spin phase transition. To test such hypothesis, the measurements of spin asymmetries and cross sections need very good accuracy. New precise data on A_{LL} over a wide range of x_1 and x_2 could give more detailed information regarding polarized constituent interactions and provide complementary restriction on parameters of the scaling variable z. The hypothesis of self-similarity of spin-dependent structure of proton interactions encoded in the parameters $\delta, \Delta\delta$ and in the functions Ψ_{++}, Ψ_{+-} is considered to play an important role to understand origin of the proton spin.

Study of the behavior of the respective ratios of spin-dependent self-similarity parameters $(z_{++}/z_{00}, z_{+-}/z_{00})$ leads us to a conclusion that interaction of the protons with mutually parallel spin orientations along the collision axis allows to probe their spin structure at smaller scales in comparison with the situation where the spins of both polarized protons are aligned in the opposite direction. Such inference relies on fractal structure of hadron constituents as implemented in the z-scaling formalism and, as we consider, reflects the self-similarity of hadron interactions in spin dependent processes at a constituent level.

The measurements of non-zero asymmetry, A_{LL}, give us strong motivation to study fractal properties of proton spin in the reactions with inclusive jet production. We believe that considered scaling property for polarization processes reflects the self-similarity of the spin structure of the colliding objects and interaction mechanism of their constituents. We hope that systematic experimental investigations of such processes will contribute to further development of theory and understanding of spin as one of the most important and basic property of particles.

- ***Recent STAR Heavy-Ion Results***

Mikhail Tokarev (for the STAR collaboration). Review talk at the XXIII International Seminar "Relativistic Nuclear Physics and QCD", Dubna, 2016. EPJ Web of Conferences 138 , 01016 (2017).

The recent STAR heavy-ion results obtained in the first phase of the RHIC Beam Energy Scan program are presented. The measurements of particle spectra have been performed over a wide range of collision energy $\sqrt{s_{NN}}$ = 7.7–200 GeV, centrality and transverse momentum of produced particles. The fixed target mode in heavy-ion collisions at the STAR experiment also extends considerably the range of search for the new physics. Heavy quarks provide an exceptional probe in understanding properties of the hot and dense medium created in such collisions. The Heavy Flavor Tracker (HFT) and Muon Telescope Detector (MTD) upgrades at the STAR experiment at RHIC significantly improved the experimental capabilities of TPC, ToF and EMC detectors in measuring both open and hidden heavy flavor hadrons in heavy-ion collisions.

- ***Fractal structure of hadrons in processes with polarized protons at SPD NICA***

M. V. Tokarev, 1, I. Zborovsky, A. A. Aparin, Phys. Part. Nucl .Lett, Vol.12,№1, 2015, 48-58

The concept of *z*-scaling previously developed for analysis of inclusive reactions in proton-proton collisions is applied for description of processes with polarized protons at the planned Spin Physics Detector (SPD) NICA in Dubna. A hypothesis of self-similarity and fractality of the proton spin structure is discussed for verification in processes with polarized protons.

The *z*-scaling approach shows itself as an effective tool for sophisticated data analysis in searching for new phenomena, verification of theoretical models, etc. Extension of the method for analysis of polarization phenomena and verification of self-similarity of spin-dependent inclusive cross sections for particle production in p+p collisions is an interesting problem which could give new insight into the origin of proton spin at small scales. The spin-dependent fractal dimensions are new parameters of the *z*-scaling theory. They are new characteristics of polarization properties of proton structure, constituent interactions and hadronization process. The possibilities to extract information on spin-dependent fractal dimensions of hadrons and fragmentation process from asymmetries and coeffients of polarization transfer are justifed. The double longitudinal spin asymmetry A_{LL} of π^0-meson production and the coeffcient of the polarization transfer D_{LL} of Λ-hyperon production in proton-proton collisions measured at RHIC are analyzed in the framework of *z*-scaling. The spin-dependent fractal dimensions of proton and fragmentation process with polarized Λ hyperon are estimated. A study of the spin-dependent constituent energy loss as a function of transverse momentum of the inclusive hadron and collision energy is suggested.

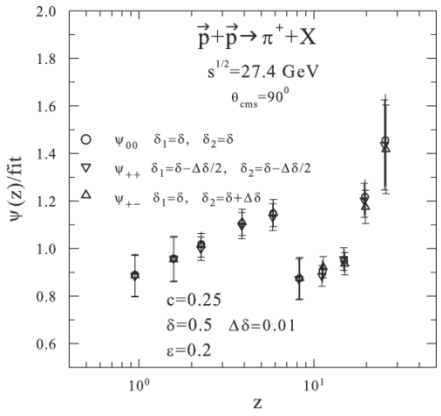

Figure A1.10. The ratios of the scaled spin-dependent and spin-independent functions for inclusive jet production in polarized p-p collisions at $\sqrt{s}$ = 200 GeV.

The scaled spin-dependent Ψ_{++}, Ψ_{+-} and spin-independent Ψ_{00} functions of pion production in proton-proton collisions at $\sqrt{s}$ = 27.4, 200 GeV and $\vartheta_{cms} = 90^0$ in z -presentation.

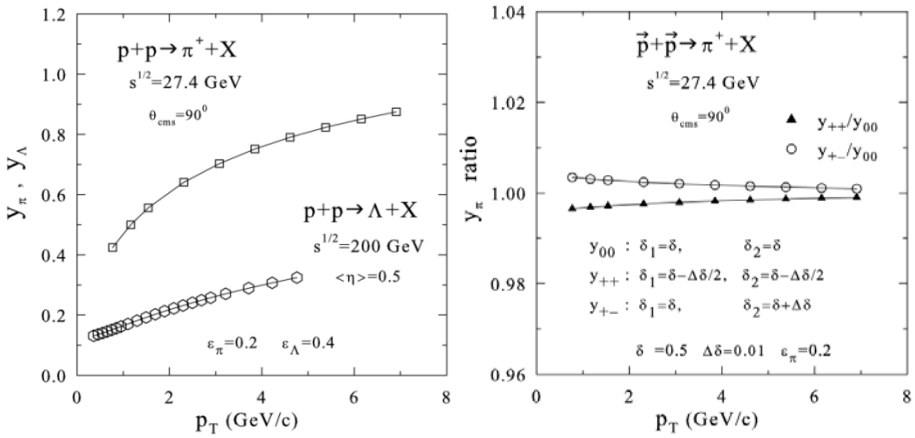

Figure A1.11. The momentum fraction y_a and the scaled ratio of the momentum fractions for pion production in unpolarized and polarized p-p collisions at $\sqrt{s}$ = 27.4 GeV.

▪ ***Possible effect of mixed phase and deconfinement upon spin correlations in the $\Lambda-\overline{\Lambda}$ pairs generated in relativistic heavy-ion collisions***

V.V. Lyuboshitz, Journal of Physics : Conference Series, v. 668 , 012130 (4 pages), 2016

Spin correlations for the $\Lambda-\Lambda$ and $\Lambda-\overline{\Lambda}$ pairs generated in relativistic heavy ion collisions, and related angular correlations at the joint registration of hadronic decays of two hyperons, in which space parity is not conserved are analyzed. The correlation tensor components can be derived from the double angular distribution of products of two decays by the method of "moments". The properties of the "trace" of the correlation tensor (a sum of three diagonal components), determining the relative fractions of the triplet states and singlet state of respective pairs, are discussed. Spin correlations for two identical particles ($\Lambda-\Lambda$) and two non-identical particles ($\Lambda-\overline{\Lambda}$) are considered from the viewpoint of the conventional model of one particle sources. In the framework of this model, correlations vanish at sufficiently large relative momenta. However, under these conditions, in the case of two non-identical particles ($\Lambda-\overline{\Lambda}$) a noticeable role is played by two-particle annihilation (two-quark, two-gluon) sources, which lead to the difference of the correlation tensor from zero. In particular, such a situation may arise when the system passes through the "mixed phase".

▪ ***On the pair correlations of neutral K , D, B and B_s mesons with close momenta produced in inclusive multiparticle processes***

V.V. Lyuboshitz, Journal of Physics : Conference Series, v. 668 , 012112 (2 pages), 2016

The phenomenological structure of inclusive cross-sections of the production of two neutral K mesons in hadron-hadron, hadron-nucleus and nucleus-nucleus collisions is investigated taking into account the strangeness conservation in strong and electromagnetic interactions. Relations describing the dependence of the correlations of two short-lived and two long-lived neutral kaons $K_S^0K_S^0$, $K_L^0K_L^0$ and the correlations of "mixed" pairs $K_S^0K_L^0$ at small relative momenta upon the space-time parameters of the generation region of K^0 and $\overline{K}^0$ mesons have been obtained. These relations involve the contributions of Bose-statistics and S-wave strong final state interaction of two K^0 ($\overline{K}^0$)-mesons as well as of K^0 meson with $\overline{K}^0$-meson, and also the contribution of transitions $K^+K^-\to K^0\overline{K}^0$ and they depend upon the relative fractions of produced pairs K^0K^0,

$\overline{K}^0\overline{K}^0$ and $K^0\overline{K}^0$. It is shown that under the strangeness conservation the correlation functions of the pairs $K_S^0K_S^0$ and $K_L^0K_L^0$, produced in the same inclusive process, coincide, and the difference between the correlation functions of the pairs $K_S^0K_S^0$ and $K_S^0K_L^0$ is conditioned by the production of the pairs of nonidentical neutral kaons $K^0\overline{K}^0$.

Analogous correlations for the pairs of neutral heavy mesons D^0, B^0 and B_S^0, generated in multiple processes with the charm (beauty) conservation are analyzed and differences from the case of neutral K mesons are discussed.

- ***New indication on scaling properties of strangeness production in pp collisions at RHIC***

International Journal of Modern Physics A Vol. 32, No. 5 (2017) 1750029 (42 pages)

Search for fundamental symmetries is main goal of all sciences and physics, in particular. Fundamental symmetry principles dictate the basic laws of physics, control the structure of matter, and define the fundamental forces in Nature. Among them are principles of relativity (special, general, scale), gauge invariance, locality, selfsimilarity, spontaneous symmetry breaking and others. One of the fundamental principles governing hadron interactions at high energies is the self-similarity principle. Its relation to the scale relativity and fractal properties of the quantum space-time. The scaling behavior related to the ideas of self-similarity of hadron interactions at a constituent level is manifested by the *z*-scaling. The scaling was used for analysis of inclusive spectra obtained at the accelerators U70, SppS, SPS, ISR, Tevatron and RHIC. The transverse momentum spectra reveal striking similarity over a wide range of energies when expressed by the variable *z*. The scaling is treated as manifestation of the self-similarity of the structure of the colliding objects (hadrons or nuclei), the interaction mechanism of their constituents, and the process of fragmentation into real hadrons. Universality of the *z*-scaling is given by its flavor independence. It means that spectra of particles with different flavor content can be described by the same function $\Psi(z)$ with values of *z* and Ψ rescaled by a multiplicative factor α_F. The factor was found to be constant over a wide kinematic range. The *z*-scaling was confirmed in the region which is far from boundary of a phase transition or the region where a critical point can be located. We consider that the approach can be a suitable tool to search for the phase transition and critical point in hadron and nuclear matter at energies where the Beam Energy Scan program is being currently performed at RHIC.

The strange particles are traditionally used as special probes for studying the medium created in the collisions of protons or nuclei. Strangeness, as well other quark flavors, is conserved in the strong interactions. Production of strange quarks accompanied with their antiquark partners can serve as a good indicator of properties of the hadron and nuclear matter and, especially, the Quark-Gluon Plasma (QGP) which is a new state of this matter. The original idea of enhanced production of hadrons containing strange quarks as a signature of quark deconfinement has been proposed by Rafelski and Hagedorn. It is now generally accepted that strangeness enhancement provides a signal for the formation of QGP and strange quarks play a crucial role in shaping the phase diagram of QCD matter.

Experimental data on transverse momentum spectra of strange particles produced in pp collisions

at $\sqrt{s_{NN}}$ = 200 GeV obtained by the STAR and PHENIX collaborations at RHIC are analyzed in the framework of *z*-scaling approach. Results of the analysis are compared with other data on meson and hyperon spectra obtained at RHIC, ISR, SPS and Tevatron. The concept of the *z*-scaling is based on fundamental principles of self-similarity, locality, and fractality of hadron interactions at high energies. General properties of the data *z*-presentation are studied. Self-similarity of fractal structure of protons and fragmentation processes with strange particles is discussed. A microscopic scenario of constituent interactions developed within the *z*-scaling scheme is used to study the dependence of momentum fractions and recoil mass on the collision energy, transverse momentum and mass of produced inclusive particle, and to estimate the constituent energy loss. We consider that obtained results can be useful in study of strangeness origin, in searching for new physics with strange probes, and can serve for better understanding of fractality of hadron interactions at small scales.

Figure A1.12 shows the spectra of strange meson and baryon production in pp collisions in *z*-presentation. The solid line is the reference curve corresponding to negative pion production in pp collisions.

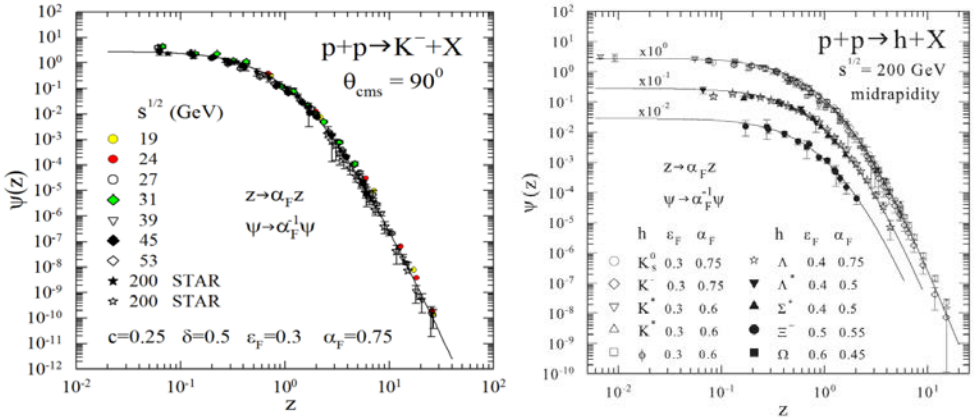

Figure A1.12. Spectra of strange particle production in *z*-presentations.

The *z*-presentation of the transverse momentum spectra demonstrates the energy independence of $\psi(z)$ over the analyzed kinematic range at the constant values of the parameters δ= 0.5, c = 0.25. The approximate matching of the data points and the solid curve corresponding to π^- mesons is obtained for α_F = 0.75. The function $\psi(z)$ exhibits two regimes of the behavior: one is seen in the low-*z* and the other one — in the high-*z* region. The low-*z* region corresponds to the saturation of the scaling function with a typical flattening out. The behavior of $\Psi(z)$ at $z < 1$ (low p_T) depends mainly on the parameter *c*. This parameter was determined from the multiplicity dependence of the inclusive spectra. The region at high *z* (high p_T) is characterized by the power behavior $\Psi(z) \sim z^{-\beta}$ with a constant value of the slope parameter β.

The amount of energy loss and its dependence on the collision energy and transverse momentum of the produced inclusive particle has relevance to the evolution of the hadron matter created in proton and nucleus collisions. The energy loss is influenced by the flavor content of the inclusive hadron. Studying its properties for strange particles can be useful for searching for signatures of new phenomena in the multiple strong interacting system. The quantities which characterize the process with energy loss in the *z*-scaling scheme are the fragmentation dimensions ε_F and the corresponding momentum fractions y_a. In this approach, the relative energy loss of the scattered

constituent with energy E is given by the relation $\Delta E/E = (1 - y_a)$. Its dependence on $\sqrt{s_{NN}}$, p_T and strangeness content of the produced hadron gives information on the medium created in the collisions of protons and nuclei and also on properties of the fragmentation and structure of the strange probes themselves.

Figure A1.10. shows the dependence of the momentum fraction y_a of strange meson and baryon production in pp collisions on transverse momentum.

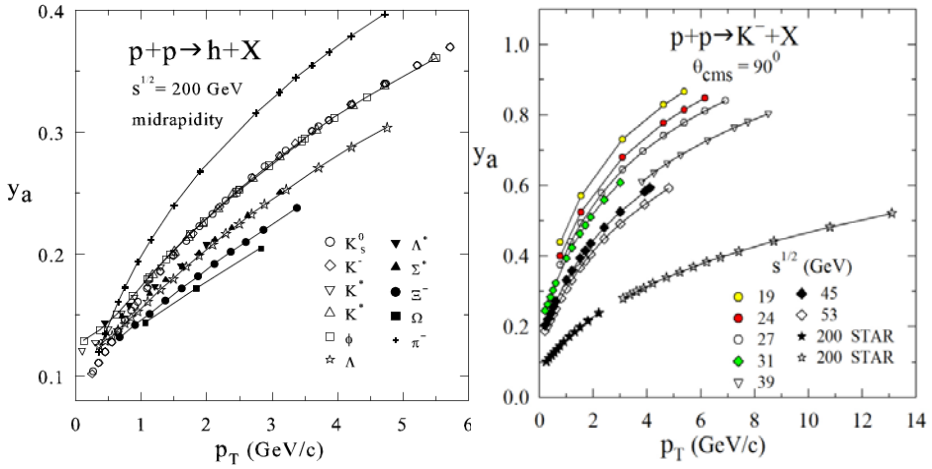

Figure A1.13. Momentum fraction of y_a as a function of collision energy and transverse momentum for different strange particles produced in pp collisions.

One can see from Figure A1.13 the fraction y_a increases with p_T for all particles. The relative energy loss $\Delta E/E$ depends on a value of the fragmentation dimension ε_F. The energy loss decreases with increasing p_T for all particles. For a given $p_T > 1$ GeV/c, the energy loss is larger for strange baryons than for strange mesons. The growth indicates increasing tendency with larger number of strange valence quarks inside the strangebaryon $(\Delta E/E)_\Omega > (\Delta E/E)_\Xi > (\Delta E/E)_\Lambda \approx (\Delta E/E)_{\Lambda^*} \approx (\Delta E/E)_\Sigma$.

- ***Recent STAR spin results and future spin measurements at RHIC***

M.V. Tokarev (for the STAR Collaboration) Review talk at the XVII International Workshop on High Energy Spin Physics "DSIPN17", September, Dubna, 2017
Preprint JINR E1-2018-11, Submitted to journal Phys.Part. Nucl. Lett.

A main goal of the spin physics program at the Relativistic Heavy Ion Collider (RHIC) at Brookhaven National Laboratory is to investigate processes of particle production in collisions of polarized protons, to understand the spin origin of the proton in terms of quarks and gluons as fundamental degrees of freedom of Quantum Chromodynamics. The ability to collide polarized beams at RHIC provides unique information on polarization phenomena over a wide range of collision energy, momentum and rapidity of the various probes produced (pions, photons, W bosons and jets). The STAR experiment at RHIC provides measurements of single and double-spin asymmetry in longitudinally and transversely polarized p+p collisions at $\sqrt{s_{NN}}$ = 200 and 510 GeV to deepen our understanding of the proton spin structure and dynamics of parton interactions. Polarized processes with W^- production allow us to study the spin-avor structure of the proton. Recent results obtained by STAR on the double longitudinal asymmetry, A_{LL}, of pion and jet production at $\sqrt{s_{NN}}$ = 200 and 510 GeV, the single longitudinal, A_L, and transverse, A_N,

asymmetry of *W* production at $\sqrt{s_{NN}}$ = 510 GeV are overviewed. Measurements on the transverse spin transfer of Λ and anti-Λ in *p+p* collisions providing insights into transversely polarized fragmentation function and nucleon transversity distribution, and the nuclear modifcation of transverse spin asymmetry, *AN*, from polarized *p+Au* collisions are discussed. The proposed Forward Calorimeter System (FCS) and Forward Tracking System (FTS) upgrades at STAR would signifcantly improve the capabilities of existing detectors for measurements of observables such as asymmetries of pion, jet, Drell-Yan pairs produced at forward rapidities.

- ***Fractional Momentum Loss of Hadrons in Au+Au Collisions at BES Energies***

A.*Kechecyan, STAR Regional Meeting , Warsaw, Poland, June 27-30, 2017*

It has been established that in relativistic heavy-ion collisions a hot, dense medium is rapidly formed, capable of interacting with the high-p_T partons produced in primordial hard scattering and making them lose some energy while traversing the medium. Quantifying this energy loss is an important issue, because it is directly connected to the properties of the medium.

The Alternative Method to Estimate Fractional Momentum Loss (FML) was suggested in the Phys. Rev.C 93, 024911 (2016) and used for analysis of RHIC(PHENIX) and LHC (ALICE) data. STAR BES-I negative charged particle transverse momentum spectra in Au+Au were used for estimation of the fractional momentum loss vs. energy and centrality.

Calculation of the difference of normalized transverse momentum spectra is performed at the same yield. The events are divided into centrality classes: 0–5%, 5–10%, 10–20%, 20–40%, 40–60%, 60–80%. Fraction energy loss is defined as follows $\delta p_T / p_T = (p_T^0 - p_T^i)/p_T$,where index 0 corresponds to centrality 60–80%, and index i to the other centralities.

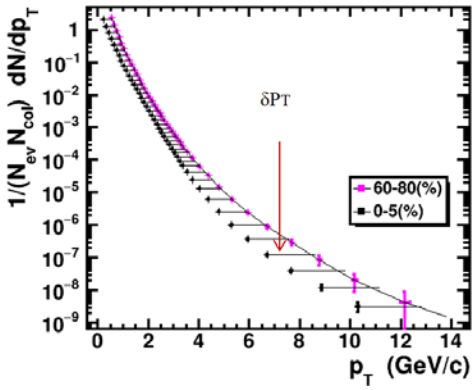

Figure A1.14. Normalized transverse momentum spectra at 0–5% and 60–80% centralties.

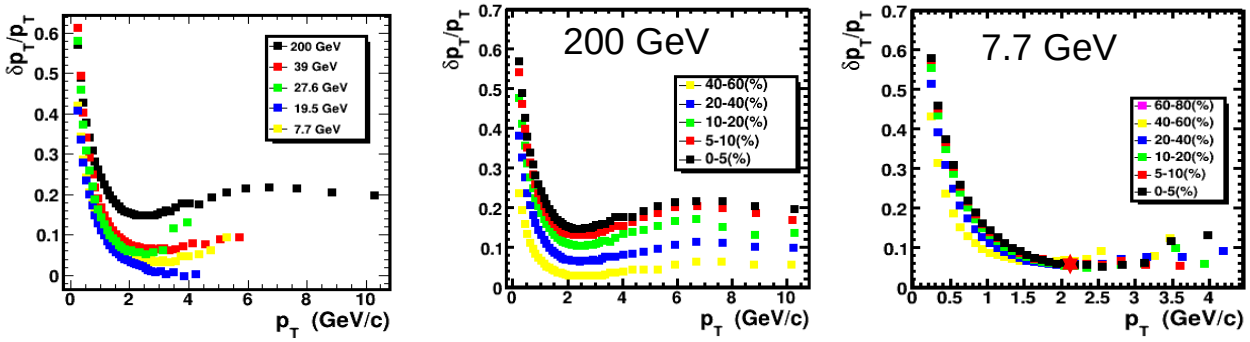

Figure A1.15. Fractal momentum loss as a function of transverse momentum and centrality at BES-I energies.

Preliminary results of analysis demonstrate that FML decreases with energy, strong centrality dependence of FML is found at 200 GeV, centrality difference of FML decreases with collision energy.

References

1. Self-similarity of negative particle production from the Beam Energy Scan Program at STAR
M.V.Tokarev, International Journal of Modern Physics: Conference Series, 39, 1560103 (12 pages), 2015

2. Fractal structure of hadrons in processes with polarized protons at SPD NICA
M.V.Tokarev, I.Zborovsky, A.A.Aparin, Письма в ЭЧАЯ , ISSN:1814-5957 , eISSN:1814-5973 , Изд:ОИЯИ, 12, 1, 48-58, 2015

3. Self-similarity of hard cumulative processes in fixed target experiment for BES-II at STAR
M.V.Tokarev, I.Zborovsky, A.A.Aparin, Письма в ЭЧАЯ , ISSN:1814-5957 , eISSN:1814-5973 , Изд:ОИЯИ, 12, 2, 221-229, 2015

4. Self-similarity of proton spin and asymmetry of jet production
M.V.Tokarev, I.Zborovsky, Письма в ЭЧАЯ , ISSN:1814-5957 , eISSN:1814-5973 , Изд:ОИЯИ, 12, 2, 214-220, 2015

5. Cumulative hadron production in pA collisions in the framework of z-scaling
A.A.Aparin, M.V.Tokarev, International Journal of Modern Physics: Conference Series, 39, 1560110 (7 pages), 2015

6. Two-step procedure of fractal analysis
T.G.Dedovich, M.V.Tokarev, Physics of Particles and Nuclei Letters , ISSN:1547-4771 , Изд:Pleiades Publishing, 13, 2, 178-189, 2016

7. Analysis of fractals with combined partition
T.G.Dedovich, M.V.Tokarev, Physics of Particles and Nuclei Letters , ISSN:1547-4771 , Изд:Pleiades Publishing, 13, 2, 169-177, 2016

8. Self-similarity of strangeness production in pp collisions at RHIC
M.V.Tokarev, I.Zborovsky, Journal of Physics: conference series, ISSN:1742-6588, eISSN:1742-6596, Изд:IOP Publishing Limited, 668, 012087, 2016

9. J/psi production at low transverse momentum in p+p and d+Au collisions at √sNN = 200 GeV
L. Adamczyk, ... A. Aparin et al. (STAR Collaboration), Physical Review C, Nuclear Physics, ISSN:0556-2813, eISSN:1089-490X, Изд:American Physical Society, 93, 6, 064904/1-064904/11, 2016

10. Upsilon production in U + U collisions at √sNN = 193 GeV measured with the STAR experiment
L. Adamczyk, ... A. Aparin et al. (STAR Collaboration), Physical Review C, Nuclear Physics,

ISSN:0556-2813, eISSN:1089-490X, Изд:American Physical Society, 94, 6, 064904/1-064904/9, 2016

11. Jet-like Correlations with Direct-Photon and Neutral-Pion Triggers at sNN&8722;&8730;=200sNN=200 GeV
STAR Collaboration (L. Adamczyk (AGH-UST, Cracow) et al.)., Phys. Lett. B, 760, 689-696, 2016

12. Bulk Properties of the Medium Produced in Relativistic Heavy-Ion Collisions from the Beam Energy Scan Program
L. Adamczyk ... A.A. Aparin et al. (STAR Collaboration), Physical Review C, Изд:American physical society, 96, 4, 044904/1-044904/34, 2017

13. Charge-dependent directed flow in Cu+Au collisions at √sNN = 200 GeV
L. Adamczyk, ... A. Aparin et al. (STAR Collaboration), Physical Revew Letters, ISSN:0031-9007, eISSN:1079-7114, Изд:American Physical Society, 118, 1, 012301/1-012301/8, 2017

14. New indication on scaling properties of strangeness production in pp collisions at RHIC
M. V. Tokarev, I.Zborovsky, Internatiional Journal of Modern Physics A, 32, 1750029(42 pages), 2017

15. Coherent diffractive photoproduction of ?0 mesons on gold nuclei at 200 GeV/nucleon-pair at the Relativistic Heavy Ion Collider
L. Adamczyk ... A.A. Aparin ... et al. (STAR collaboration), Physical Review C, Изд:American physical society, 96, 5, 054904/1-054904/12, 2017

17. Self-similarity of hadron production: z-scaling
Tokarev M.V. , Zborovsky I., Theoretical and Mathematical Physics, ISSN:0040-5779, eISSN:1573-9333, Изд:Springer New York, 184, 3, 1350-1360, 2016

18. Scaling of cumulative particle production and production of particles with large transverse momentum in proton-nucleus collisions at high energies.
A.A. Aparin, PhD thesis, JINR, November 19, 2017

Reports at international conferences, workshops, collaboration meetings in 2017

1. M.V.Tokarev (for the STAR Collaboration)
Recent STAR spin results and spin measurements at RHIC,
XVII Workshop on High Energy Spin Physics ", Dubna, Russia, September 11-15, 2017
http://theor.jinr.ru/~spin/2017/

2. M.V.Tokarev, I.Zborovsky
"Fractality of strange particle production in pp collisions at RHIC",
18th Lomonosov Conference on Elementary Particle Physics MSU, Moscow, Russia, August 24 - 30, 2017.
http://www.icas.ru/english/index.htm

3. M.V. Tokarev, I.Z. borovsky, A.O. Kechechyan
"Fractality of strange particle production in pp collisions at RHIC",
Regional STAR Meeting MEPhI, Moscow, Russia, August 23, 2017.

4. М.В. Токарев (ОИЯИ, Дубна)
«Спиновая физика на STAR»,
Объединенный семинар Лаборатории физики высоких энергий, 1 декабря 2017, ЛВФЭ ОИЯИ.

5. A.O. Kechechyan
Fractional Momentum Loss of Hadrons in Au+Au Collisions at BES Energies
Regional STAR Meeting MEPhI, Moscow, Russia, August 23, 2017.

6. A.O. Kechechyan
Fractional Momentum Loss of Hadrons in Au+Au Collisions at BES Energies
STAR Regional Meeting , Warsaw, Poland, June 27-30, 2017

7. Valery V. Lyuboshitz, V.L. Lyuboshitz

"Possible effect of mixed phase and deconfinement upon spin correlations in the $\Lambda\bar{\Lambda}$ pairs generated in relativistic heavy-ion collisions". Talk at the XVII Advanced Research Workshop on High Energy Spin Physics – DSPIN-2017 (Dubna, September 11 – 15, 2017) ; allo-cated on the DSPIN-2017 website (PDF file) . Submitted to Proceedings of DSPIN-2017 (*Journal of Physics: Conference series* , 2018) .

8. Valery V. Lyuboshitz, V.L. Lyuboshitz
"On the pair correlations of neutral *K, D*, *B* and B_s mesons with close momenta produced in inclusive multiparticle processes". Talk at the XVII International Conference on Hadron Spectroscopy and Structure – HADRON 2017 (Salamanca, Spain, September 21 – 25, 2017) ; allocated on the Indico website of HADRON 2017 (PDF file) . Submitted to Proceedings of HADRON 2017 (PoS (Hadron2017) 041, *Proceedings of Science* , v. **310** , 2018)

9. Valery V. Lyuboshitz, V.L. Lyuboshitz

"Possible effect of mixed phase and deconfinement upon spin correlations in the $\Lambda\bar{\Lambda}$ pairs generated in relativistic heavy-ion collisions". Poster presentation at the 24-th International European Physical Society Conference on High Energy Physics – EPS-HEP 2017 (Venice, Italy, July 5 – 12, 2017) ; allocated on the Indico website of EPS-HEP 2017 (PDF file). Accepted for Proceedings of EPS-HEP 2017 (PoS (EPS-HEP2017) 653, *Proceedings of Science*, v. **314** , 2018)

10. Valery V. Lyuboshitz, V.L. Lyuboshitz
"On the coherent inelastic binary and multiparticle processes in ultrarelativistic hadron–nucleus, photon–nucleus and nucleus–nucleus collisions". Poster presentation at the 24-th International European Physical Society Conference on High Energy Physics – EPS-HEP 2017 (Venice,

Italy, July 5 – 12, 2017) ; allocated on the Indico website of EPS-HEP 2017 (PDF file). Accepted for Proceedings of EPS-HEP 2017 (PoS (EPS-HEP2017) 652, *Proceedings of Science* , v. **314** , 2018)

11. Valery V. Lyuboshitz, V.L. Lyuboshitz
"Polarization effects in the reactions $p + {}^3He \to \pi^+ + {}^4He$, $\pi^+ + {}^4He \to p + {}^3He$ and quantum character of spin correlations in the final (p, ${}^3He$) system". Poster presentation at the 24-th International European Physical Society Conference on High Energy Physics – EPS-HEP 2017 (Venice, Italy, July 5 – 12, 2017) ; allocated on the Indico website of EPS-HEP 2017 (PDF file). Submitted to Proceedings of EPS-HEP 2017 (PoS (EPS-HEP2017) 743, *Proceedings of Science* , v. **314** , 2018) .

12. Valery V. Lyuboshitz, V.L. Lyuboshitz
"The process of Coulomb dissoci-ation of weakly bound relativistic hypernuclei within the two-cluster model" . Poster presentation at the 24-th International European Physical Society Conference on High Energy Physics – EPS-HEP 2017 (Venice, Italy, July 5 – 12, 2017) ; allocated on the Indico website of EPS-HEP 2017 (PDF file). Submitted to Proceedings of EPS-HEP 2017 (PoS (EPS-HEP2017) 742, *Proceedings of Science* , v. **314** , 2018).

13. Valery V. Lyuboshitz, V.L. Lyuboshitz . "Polarization effects in the reactions $p + {}^3He \to \pi^+ + {}^4He$, $\pi^+ + {}^4He \to p + {}^3He$ and quantum character of spin correlations in the final (p, ${}^3He$) system" . Poster presentation at the XVII Advanced Research Workshop on High Energy Spin Physics – DSPIN-2017
(Dubna, September 11 – 15, 2017) ; submitted to Proceedings of DSPIN-2017 (*Journal of Physics: Conference series* , 2018).

14. Valery V. Lyuboshitz, V.L.Lyuboshitz . "On the coherent inelastic binary and multiparticle processes in ultrarelativistic hadron–nucleus, photon–nucleus and nucleus–nucleus collisions". Poster presentation at the XVII International Con-ference on Hadron Spectroscopy and Structure – HADRON 2017 (Salamanca, Spain, September 21 – 25, 2017) ; allocated on the Indico website of HADRON 2017 (PDF file) . Submitted to Proceedings of HADRON 2017
(PoS (Hadron2017) 227, *Proceedings of Science* , v. **310** , 2018).

15. Valery V. Lyuboshitz, V.L.Lyuboshitz . "Possible effect of mixed phase and deconfinement upon spin correlations in the $\Lambda\,\overline{\Lambda}$ pairs generated in relativistic heavy-ion collisions". Poster presentation at the XVII International Conference on Hadron Spectroscopy and Structure – HADRON 2017 (Salamanca, Spain, September 21 – 25, 2017) ; allocated on the Indico website of HADRON 2017 (PDF file) . Submitted to Proceedings of HADRON 2017
(PoS (Hadron2017) 226, *Proceedings of Science* , v. **310** , 2018).

16. Valery V. Lyuboshitz, V.L.Lyuboshitz . "The process of Coulomb dissoci-ation of weakly bound relativistic hypernuclei within the two-cluster model" . Poster presentation at the XVII International Conference on Hadron Spectroscopy and Structure – HADRON 2017 (Salamanca, Spain, September 21 – 25, 2017) ;

allocated on the Indico website of HADRON 2017 (PDF file) . Submitted to Proceedings of HADRON 2017 (PoS (Hadron2017) 228, *Proceedings of Science* , v. **310** , 2018)

Appendix 2. STAR Upgrades for BES-II

STAR has three detector upgrades planned for Run 18 and/or Run 19: the inner Time Projection Chamber (iTPC), Event Plane Detector (EPD) and endcap Time of Flight (eTOF). The iTPC will increase the acceptance of the TPC, it will improve the *dE/dx* resolution, and will allow tracks to be reconstructed down to p_T of 60 MeV/*c*. The EPD will replace the BBC as a minimum-bias trigger detector and will allow forward measurements of both the centrality and event plane. The eTOF will be installed on one side of STAR, which will extend PID capabilities at forward rapidities. These upgrades are described in more detail below, and their overall location in the STAR detector is shown in Fig. A4.1.

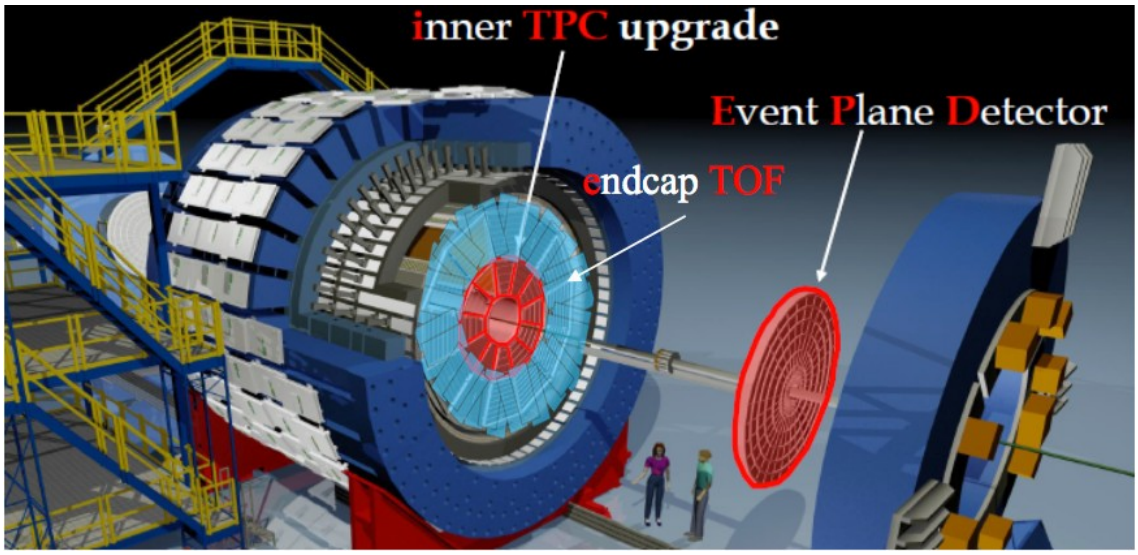

Figure A4.1: Rendering of the STAR detector with the upgrades highlighted in red. The EPD and iTPC are symmetric in STAR whereas the eTOF is only on the east side.

The acceptance and the limit in p_T vs. rapidity for different species using PID from either the iTPC, bTOF or eTOF are show in Fig. A4.2.

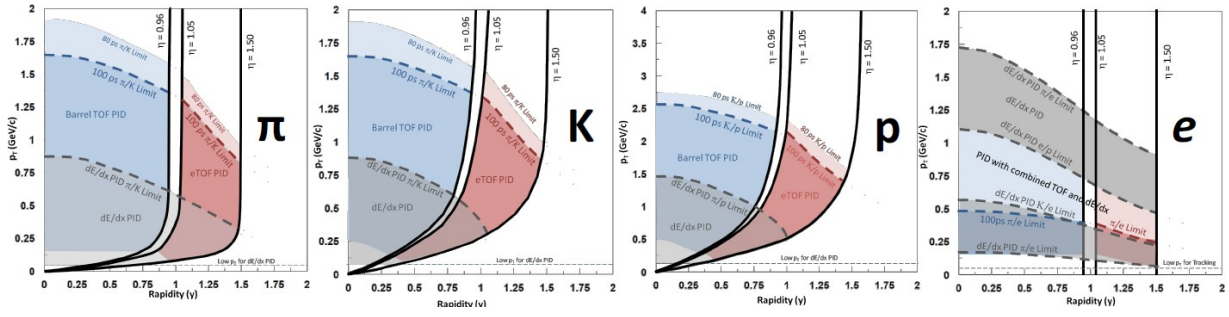

Figure A4.2: Acceptance and PID limits for π, K, proton and electrons with STAR instrumented with iTPC and eTOF.

These upgrades are scheduled to be phased into STAR over the next two shutdown periods. Table A4.1 summarizes when prototypes and final installation will take place.

STAR is also engaged in a R&D program that will enable a future Forward Physics program after the completion of the BES-II program. This program has been outlined in the proposal [1] also

submitted to the PAC as part of future opportunities with STAR at RHIC.

Table A4.1: Timeline for installation of upgrades.

Year	iTPC	EPD	eTOF
2017	–	1/8 installed	1 prototype
2018	One sector	**Full Installation**	3 modules at one sector
2019	**Full Installation**	**Full Installation**	**Full Installation**

The inner TPC (iTPC)

The inner sectors of the STAR TPC are being upgraded to increase the segmentation on the inner pad planes. These improvements will extend the capabilities of STAR in many ways. Most significantly, the enhanced tracking at small angles relative to the beamline will expand the TPC acceptance out to pseudorapidity $|\eta| \leq 1.5$, compared to the current limitation of $|\eta| \leq 1$. Furthermore, the detector will have better acceptance for tracks with low transverse momentum down to 60 MeV/*c*, as well as better resolution in both momentum ($\delta p/p$ improvement ~15%) at larger momenta, and dE/dx improvement of (~25%) for full length tracks. These changes will enable the collection of data that is critical to the physics mission for the BES-II. In addition, the improved *dE/dx* and momentum resolution, as well as tracking at higher pseudorapidity, provide the foundation for the success of the eTOF. The iTPC project is described in detail in the Technical Design Report [2].

The iTPC upgrade was given go ahead for construction in March 2016 following a director's review to ensure that the project could complete for the Run 19. The project had a DOE NP Technical Cost Schedule and Management review in September 2016, and progress and status is now presented monthly to the DOE. The overall schedule is still tight, but significant progress has been made. The project consists of two parts: Construction of new sectors and their MWPC readout, and development of new electronics based on the SAMPA chip doubling the number of channels per FEE card. The Al strong backs and the pad planes have all been manufactured according to specifications. Prototype bonding of pad planes to the sectors, a high precision task, has been done at LBNL, and the production phase has been entered. Two prototypes of the MWPC have been constructed at Shandong University, Jinan, China (SDU) and tested. The first step in the production is to bond the pad plane with high accuracy to the strong back. Figure A4.3 (left) shows the second bonded pad plane to an Al sector at LBNL. Subsequent steps align the side mount that will hold the wire planes with high precision, then bare sectors are shipped to SDU where wire winding and mounting takes place. Figure A4.3 (right) shows a complete sector built at SDU. This sector has been tested for gain and resolution using a ^{55}Fe source. Figure A4.4 shows a result of such measurements on a single wire. A good resolution of 20% FWHM, better than requirements, is observed.

Significant progress has also been made with the electronics. Two prototype FEE cards with the prototype MWP2 SAMPA chip have been installed, with special adapter cards, on one of the innermost rows of the STAR TPC for the Run 17 (p+p at $\sqrt{s}$ = 500 GeV). So far the electronics are performing well. It is planned to have electronics available for a full sector test on the floor, and installed for the STAR Run 18.

Figure A4.3: (left) pad plane bonded to Al strongback. (right) Complete prototype sector.

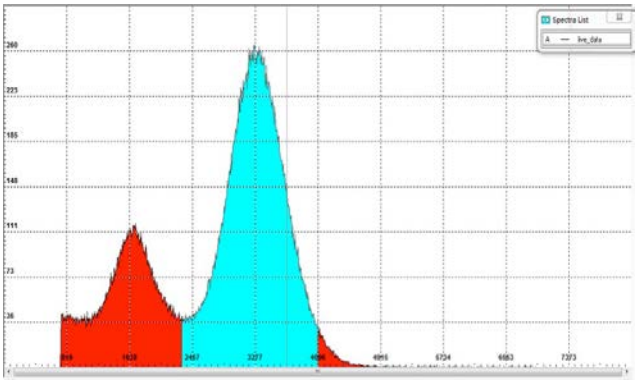

Figure A4.4: Energy spectrum from a ^{55}Fe source on a single anode wire of a prototype iTPC sector showing the main and escape peaks.

The current production and testing of the full complement of inner sectors is scheduled to complete in mid-summer of 2018, and the installation and testing period will take 10 months.

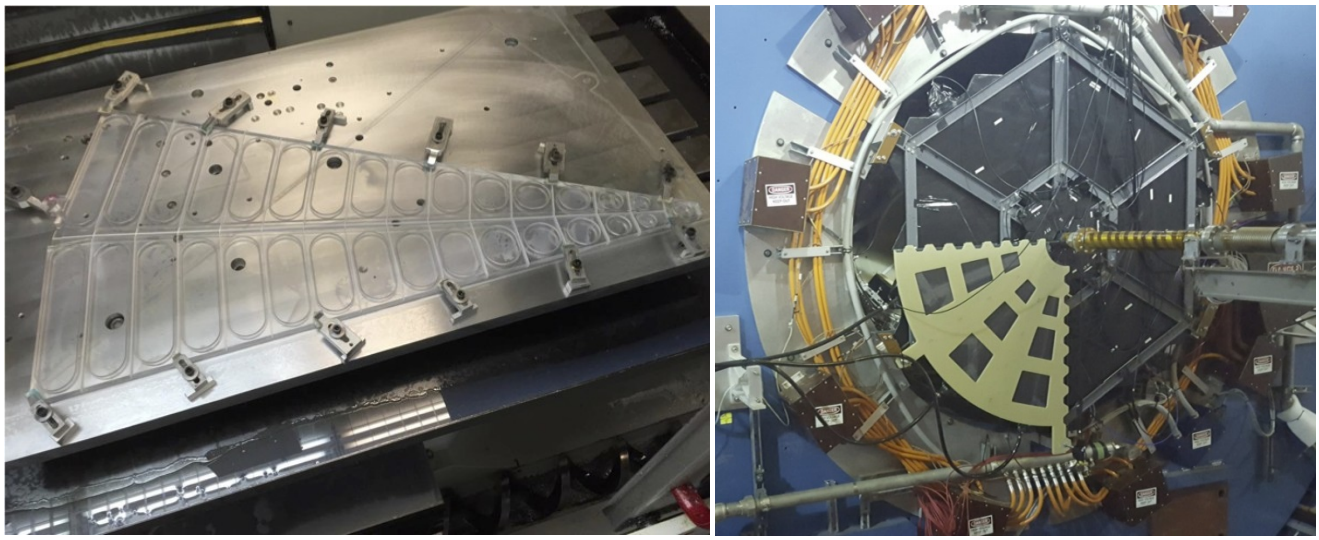

Figure A4.5: (left) The first EPD super-sector under construction at OSU. (right) The 1/8th detector installed for Run 17.

The Event Plane Detector (EPD)

A new, dedicated Event Plane, centrality, and trigger Detector (EPD) will be installed in the forward direction of STAR for Run 18 and beyond. This new detector will have pseudorapidity acceptance of $2.1 < |\eta| < 5.1$ with high radial and azimuthal segmentation. The EPD will allow the centrality and the event plane to be measured in the forward region, reducing the systematics due to autocorrelations from mid-rapidity analyses. The baseline detector design utilizes scintillator plastic, wavelength-shifting fibers and silicon photomultipliers (SiPMs).

The EPD consists of two disks that will be placed on either side of the STAR inter- action region, in the current location of the Beam-Beam Counter (BBC). The EPD will be the same size as BBC, as it is required to sit in the same space within the STAR experiment. The EPD will extend from a radius of 4.5 cm (1.77 in) to 90 cm (35.4 in) and will be located at z = 375 cm. The design allows for the EPD to be installed downstream from the BBC as a contingency for Run 18, or for the EPD to be installed instead of the BBC which is the preferred mode of operation. The EPD scintillator is 1.2 cm thick and has 12 azimuthal segments, spanning an angle of 30°, which we give the label "super-sector". There are 16 segments in η, with the innermost tile spanning the entire super-sector and the other tiles dividing it in two for better ϕ resolution. This results in a total of 744 channels for the two EPD disks. The tile size was designed such that the probability of multiple particle hits in the same tile would be less than 10% at $\sqrt{s_{NN}}$ = 19.6 GeV, based on $dN/d\eta$ measurements from PHOBOS. This increases to 65% for Au+Au collisions at 200 GeV. More details on the EPD design and expected performance can be found here [3].

Two EPD prototypes were built and tested in Runs 15 and 16. These successful tests showed that the detector could be integrated with the STAR electronics, and that the basic design principles were sound. This allowed construction of the EPD to begin; the machining of the first of the super sectors can be seen in Figure A4.5. Shown on the right of Figure A4.5 is the 1/8 of the total detector (1/4 of a single disk) installed downstream from the BBC in Run 17 for commissioning. This commissioning run will allow the quantification of the performance of the detector in terms of efficiency, and timing and test different trigger algorithms.

The first results of the EPD can be seen in Figure A4.7, which shows the ADC spectra for three different tiles: 1, 3 and 9. Since the lowest numbered tiles are closest to the beam pipe, this shows data for a variety of η positions. These curves were fit by Landau distributions, which had a 1, 2 and 3 MIP contributions. For each, an average number of 50 photons per MIP was determined, with an uncertainty on the level of 40%. In Figure A4.6, on the left shows the hits in the different EPD tiles when selecting for a signal in a single BBC tile. The BBC tile in question is shown as a red circle, and a good correlation between the hits can be seen. On the right of this figure is a time difference between a hit arriving at a BBC tile and an overlapping EPD tile. The width of this distribution, roughly 3.5 ns, is a convolution of the timing resolution of the EPD and of the BBC.

One of the important tests for the Run 17 commissioning of the EPD was to benchmark its performance versus the BBC. In Figure A4.6 the hits in the EPD tile-by-tile is shown for collisions where there was a hit in BBC PMT channel 4, and no hit in BBC PMT 5. As expected, this selection lights up the EPD tile directly behind the BBC tile, showing a nice correlation. There

were no additional selections made on the collisions, so the vertex of the collision was only constrained by the STAR minimum bias trigger.

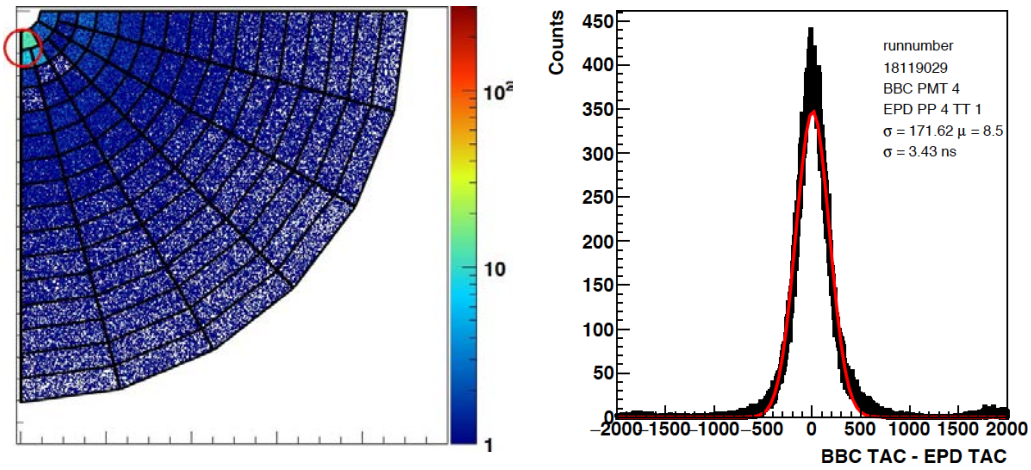

Figure A4.6: (left) Plot of the hits in different EPD tiles selecting collisions where there is a hit in BBC PMT channel 4, shown as an overlapping red circle, and no hit in the other BBC small tiles that overlap with the EPD. On the right is the time difference between a hit in an EPD tile and a hit in the overlapping BBC tile, the width of this curve is the convolution of the time resolution for both detectors.

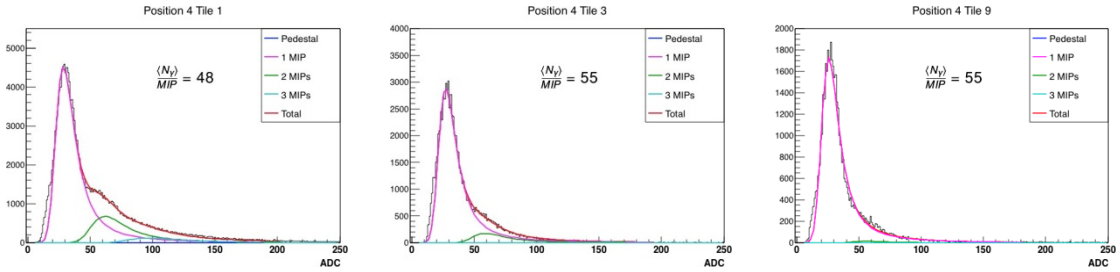

Figure A4.7: ADC spectra for three different tiles, from the highest η on the left to the mid-η region on the right. A valid TAC signal was required for each of these tiles.

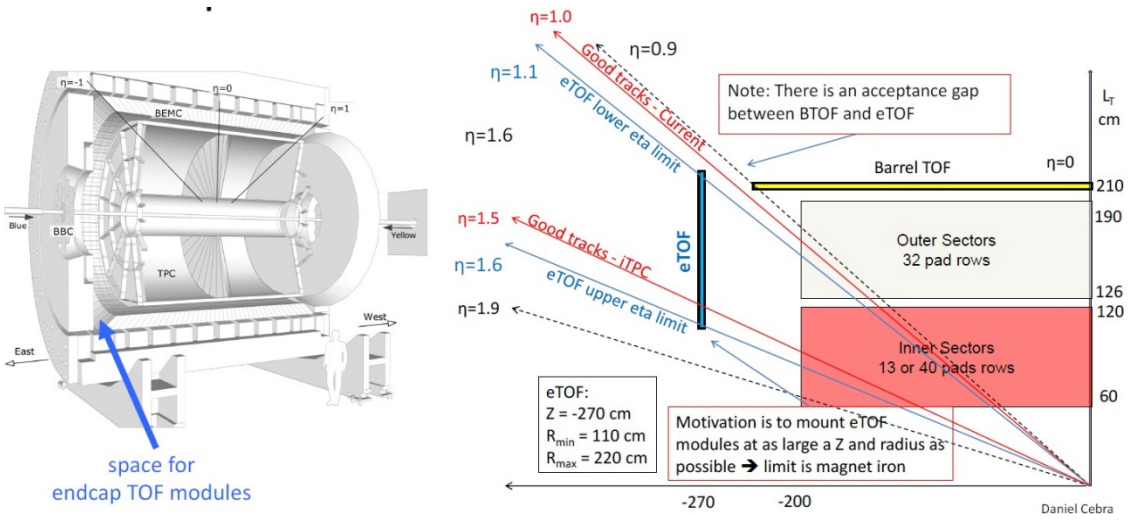

Figure A4.8: Placement and acceptance diagrams for the eTOF.

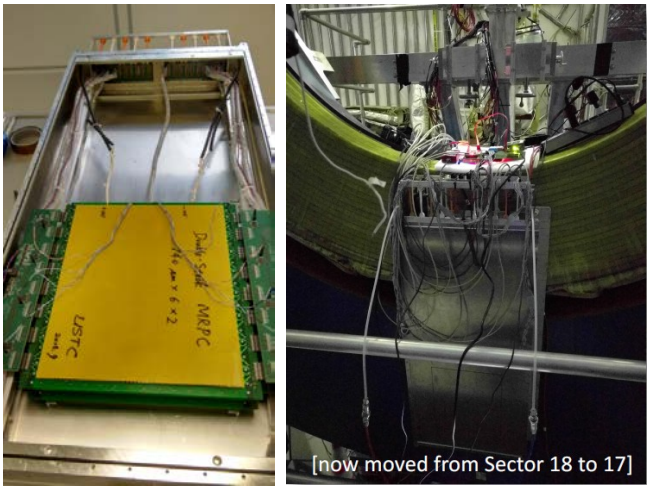

Figure A4.9: (left) The prototype module. (right) The installed module with services.

The endcap TOF (eTOF)

The STAR Collaboration and institutions from the CBM Collaboration: Heidelberg, Darmstadt, Tsinghua, CCNU, and USTC have agreed to install an endcap time-of-fight upgrade (eTOF) in the STAR detector for the BES-II program in 2019 and 2020. The improvements in acceptance and PID and the physics goals of the upgrade are described in detail in Ref. [4], and the technical description of the modules in Ref. [5]. The eTOF will be installed at the east end of STAR in the small gap between the poletip and the TPC; behind the readout electronics as depicted in the left cartoon of Figure A4.8. The right hand side of the same figure illustrates how the coverage in η is much improved with the combination of the iTPC and the eTOF.

A prototype eTOF module was installed behind one TPC sector for the ongoing run with the aim of testing the module in the RHIC environment, and integrating the CBM electronics with the STAR trigger and DAQ systems. This initial test will be followed with the installation prior to Run 18 of 3 modules to cover a full TPC sector. Figure A4.9 shows the MRPC eTOF module and the cabled up installed module.

References

[1] STAR. SN0648 - The STAR Forward Calorimeter System and Forward Tracking System beyond BES-II.

[2] STAR. SN0644 - Technical Design Report for the iTPC Upgrade.

[3] STAR. SN0666 - An Event Plane Detector for STAR.

[4] Physics Program for the STAR/CBM eTOF Upgrade. 2016.

[5] Norbert Herrmann, editor. *Technical Design Report for the CBM Time-of-Flight System (TOF)*. GSI, Darmstadt, 2014.